Copyright Warning & Restrictions

The copyright law of the United States (Title 17, United States Code) governs the making of photocopies or other reproductions of copyrighted material.

Under certain conditions specified in the law, libraries and archives are authorized to furnish a photocopy or other reproduction. One of these specified conditions is that the photocopy or reproduction is not to be "used for any purpose other than private study, scholarship, or research." If a, user makes a request for, or later uses, a photocopy or reproduction for purposes in excess of "fair use" that user may be liable for copyright infringement,

This institution reserves the right to refuse to accept a copying order if, in its judgment, fulfillment of the order would involve violation of copyright law.

Please Note: The author retains the copyright while the New Jersey Institute of Technology reserves the right to distribute this thesis or dissertation

Printing note: If you do not wish to print this page, then select "Pages from: first page # to: last page #" on the print dialog screen

ABSTRACT

GRANULAR DYNAMIC STUDY OF SIEVING

by
Heng Yung

The objective of this thesis is to study the behaviors of granular particles under sieving. A three-dimensional dynamic simulation code was transferred and modified for this purpose, The major concern is the mass flow rate of the particles. Lots of case studies were run. The influences of the friction coefficient, the sieve aperture, and the energy of vibration are studied.

GRANULAR DYNAMIC STUDY OF SIEVING

by
Heng Yung

A Thesis
Submitted to the faculty of
New Jersey Institute of Technology
in Partial Fulfillment of the Requirements for the Degree of
Master of Science in Mechanical engineering

Department of Mechanical Engineering

May 1996

APPROVAL PAGE

GRANULAR DYNAMIC STUDY OF SIEVING

Heng Yung

Dr. Anthony D. Rosato, Thesis Advisor — Date
Associate Professor of Mechanical Engineering, NJIT

Dr. Rajesh N. Dave, Committee Member — Date
Associate Professor of Mechanical Engineering, NJIT

Dr. Rong Chen, Committee member — Date
Professor of Mechanical Engineering and
Associate Chairperson and Graduate Advisor of
the Department of Mechanical Engineering, NJIT

BIOGRAPHICAL SKETCH

Author: Heng Yung

Degree: Master of Science

Date: May 1996

Undergraduate Education

- Master of Science in Mechanical Engineering,
  New Jersey Institute of Technology,
  Newark, New Jersey, 1996

- Bachelor of Science in Mechanical Engineering
  National Chung-Hsing University,
  Taichung, Taiwan, 1993

Major: Mechanical Engineering

This master thesis is dedicated to
my parents and my family

ACKNOWLEDGMENT

The author wishes to express his sincere gratitude to his advisor Dr. Anthony D. Rosato, for his guidance, friendship, and moral support through this research.

Special thanks to Drs. Rong Chen, Rajesh N. Dave, for serving as members of the committee.

The author would like to thank Dr. Mark W. Richman of Worcester Polytechnic Institute for supporting their computer investments, and furnishing their theoretical predictions. The author is also grateful to Dr. Otis R. Walton of Lawrence Livemore National Laboratory for providing a granular shear code which was modified for the purpose of these studies. Also thanks to Dr. Yidan Lan for helping on the programming, and to Laurent Labous for many stimulating discussions.

TABLE OF CONTAINS

Chapter **Page**

LIST OF TABLES

LIST OF FIGURES

Figure **Page**

CHAPTER 1

INTRODUCTION AND LITERATURE SURVEY

`1.1 Introduction, Motivation, and Overview

Through out history, from the ancient time to the present, sieving has been the least complicated, most economic, and widely used method for particle size classification. For thousands of year, sieves were used by humans in many different ways. If sieving is done properly, it can be as accurate and scientific as any other method for particle size classification. Recently, investigations on granular materials are becoming more and more prevalent because of the wide use of bulk solids in numerous industries. How to control and determine the size of the granular particles is one of the main topics of concern. While sieving may at first appear to be well understood, there are several issues which remain to be addressed, such as the effective sieve opening, the calibration method, the sieving flow, and the sieving flow rate. The goal of this project is to determine the relationships between the shaking velocity of the sieve, the mass of particles on the sieve, and the resulting mass flow rate. This is accomplished through the use of realistic granular dynamics computer simulation, which provides access to all the particle positions and velocities for subsequent analysis.

The major contribution of this work can be summarized as follows:

- Modify an existing three-dimensional simulation code for sieving analysis.
- Formulate parameter space based on the theoretical analysis of Richman [15].

- Compute diagnostics of granular temperature, and solid fraction depth profile.
- Compute the mass hold-up history over the identified range of parameters as well as the mass flow rate.
- Compare all results with Richman's theoretical predictions [15] and with qualitative behavior reported in the literature [10].

1.2 Theory and Literature Survey

To the knowledge of the author, analyses of sieving processes began as early as the 1930's, but investigations in the literature have been minimal over the last a few decades. In what follows, a survey and description of sieving are given, which highlights several open questions.

1.2.1 The Sieve Standards

The sieves employed today have been standardized for the convenience use and manufacture. There are several sieve standards which are commonly used [1,2,11] and examples are listed in Table 1.1.

Table 1.1 - Examples of Test Sieve Standards

German:	DIN 4188	woven wire test sieves
	DIN 4187	perforated plate test sieves
	DIN 4195	textile sieve cloths
Great Britain:	BS 410	woven wire test sieves

Table 1.1 - Examples of Test Sieve Standards - continued

USA:	A.S.T.M. E11-70	woven wire test sieves
	A.S.T.M. E161-607	Micromesh sieves (electroformed sieves)
France:	AFNOR NFX11-501	woven wire test sieves
International:	ISO 565	woven wire and perforated plate test sieves

Two of these standards, The Tyler Standard Screen Scale and the U.S. Sieve Series, are now used in the United States. These two standard series are exchangeable. They both follow the rule that the size of the apertures of a screen is $\sqrt{2}$ times the size of the apertures of the adjacent screen. This means that the areas of the screen openings of each sieve are twice the next finer sieve. Table 1.2 shows the U.S. standard series sieves designated as A.S.T.M. E-11a and the comparative International standard series sieves designated as ISO. R 565.

Table 1.2 -- U.S. standard sieve series (A.S.T.M. Designation E 11a)

U.S. Sieve Designation			ISO Designation b	
Aperture in mm.	Mesh No.	Aperture in inches	ISO R 565 1967 R 20/3	ISO R 565 R 40/3
1	2	3	4	5
107.6 mm	4.24	4.24		106 mm
101.6	4 c	4.00	100 mm e	
90.5	3½	3.50	90	90
76.1	3 c	3.00		75
64.0	2½	2.50	63	63
53.8	2.12	2.12		
50.8	2 c	2.00	50 e	
45.3	1¾	1.75		
38.1	1 ½	1.50		37.5
32.0	1¼	1.25	31.5	31.5
26.9	1.06	1.06		26.5
25.4	1 c	1.00	25 e	

Table 1.2 -- U.S. standard sieve series (A.S.T.M. Designation E 11a) - continued

U.S. Sieve Designation			ISO Designation b	
Aperture in mm.	Mesh No.	Aperture in inches	ISO R 565 1967 R 20/3	ISO R 565 R 40/3
1	2	3	4	5
22.6	7/8	0.875	22.4	22.4
19.0	3/4	0.75		
16.0	5/8	0.625	16	16
13.5	0.53	0.53		13.2
12.7	½ c	0.5	12.5 e	
11.2	7/16	0.438	11.2	11.2
9.51	3/8	0.375		9.5
8.00	5/16	0.312	8	8
6.73	0.265	0.265		6.7
6.35	1/4 c	0.250	6.3 e	
5.66	No. 3½ d	0.223	5.6	5.6
4.76	No. 4	0.187		4.75
4.00	No. 50	0.157	4	4
3.36	No. 6	0.132		3.35
2.83	No. 7	0.111	2.8	2.8
2.38	No. 8	0.0937		2.36
2.00	No. 10	0.0787	2	2
1.68	No. 12	0.0661		1.7
1.41	No. 14	0.0555	1.4	1.4
1.19	No. 16	0.0469		1.18
1.00	No. 18	0.0394	1	1
841 μm	No. 20	0.0331		850 μm
707	No. 25	0.0278	710 μm	710
595	No. 30	0.0234		600
500	N0. 35	0.0197	500	500
420	N0. 40	0.0165		425
354	No. 45	0.0139	355	355
297	No. 50	0.0117		300
250	No. 60	0.0098	250	250
210	No. 70	0.0083		212
177	No. 80	0.0070	180	180
149	No. 100	0.0059		150
125	N0. 120	0.0049	125	125

- b These sieves are issued by the International Standard Organization. They are included here for information.
- c These sieves are not in the standard fixed ratio series but have been included because they are in common usage.
- d These numbers (3½ to 120) are the approximate number of openings per linear inch.
- e These sieves are supplementary sizes but have been included because of being in common usage.

The mesh number (3½ to 120) represents the approximate number of openings per linear inch [2]. For example, sieve No. 100 has 100 openings per linear inch, so the sieve aperture should be equal to 0.01 inch. If you check with the Table 1 2, you will find out that the mean aperture of the sieve No. 100 is only 0.0059 inch, which means that the diameter of the sieve wire is 0.0041 inch.

1.2.2 The Effective Sieve Opening

The effective sieve opening is defined as the size of the largest particle that can pass through the sieve. If the sizes of particles to be sieved are fairly symmetric, then it can be determined directly by measuring the diameter of spherical particles which can just pass through the sieve [4]. The effective sieve opening can also be measured by a calibration method [5,9]. There are several types of calibration methods employed today, the easiest and most commonly used one is called the "*projection method*". The sieves are calibrated from measurements of a projected mesh using a microscope. The thickness of the wire is measured previously, and the number of openings per inch is counted for at least 6 inches. The average sieve opening is then determined. If the size of the openings is not uniform, the largest opening will be the effective one [4].

Although there are many kinds of calibration methods and they all can do a good job on measuring the sieve openings, it is still very difficult to determine the effective sieve opening very accurately. Bellows are some aspects of difficulties in determining the effective sieve opening [5].

(1) The sieve openings are not quite uniform. The sizes of apertures are distributed according to some probability laws and all the apertures of the sieve are rarely of the same size. That is why some over-sized particles can still pass through the larger opening and the effective sieve opening is usually larger than the average nominal opening.

(2) There are always some undersize particles remaining on the sieve and the sieving process will never be completed.

(3) The sieve openings are effective in three dimensions. So the plane of the effective opening may not be the same as the plane defined by the sieve

(4) The effective sieve opening is not a constant. It will change according to the manner in which the sieve is vibrated. One sieve can have different effective sieve opening if it is shaken at a different amplitude and frequency than another.

1.2.3 Two Different Regions in Sieving Process

By looking at the weight passing through the sieve versus time, it is observed that the sieving process can be divided into two different regions with a transfer region between them. Figure 1.1 is an example of the curve taken from Whitby in his paper "The Mechanics of Fine Sieving" [8].

The first region exists at the beginning of the sieving process. In this region, there are a lot of under-sized particles which are much smaller than the sieve openings on the sieve. All these small particles will pass through the sieve mesh quickly and the sieving

rate in this region is nearly a constant, yielding an almost straight line. on the graph of weight passing versus time

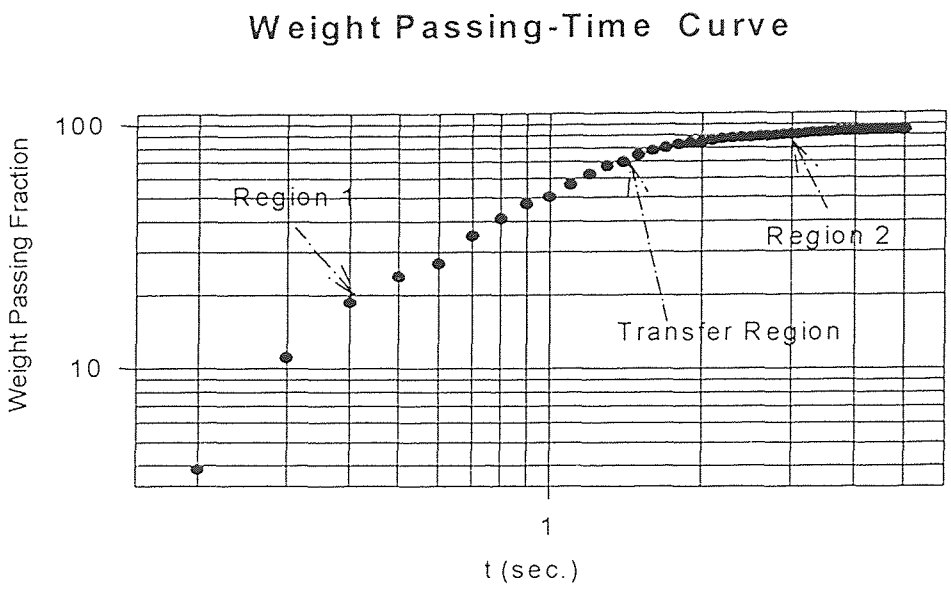

Figure. 1.1 Weight Passing versus Time Curve

In the transfer region, there are still some under-sized particles did not pass through the mesh. Most of the particles on the sieve are near-mesh particles which their sizes are nearly equal to the sieve apertures or over-sized particles which are larger than the sieve apertures. The flow rate in this region decreases and the graph is not a straight line any more.

The second region exists at the end of the sieving process. In the second region, most of the under-sized particles already passed through the sieve, and almost all the particles remain on the sieve are near-mesh or over-sized particles. Consequently, flow

rate in this region becomes very slow and the graph of the weight passing versus time for this region is nearly a horizontal line.

1.2.4 The Affective Factors of the Sieving Rate

The rate of sieving process basically depends on the probability of the particles of passing through the sieve, and this probability will be affected by the factors list below [1,6].

(1) The size of the sieve openings and the particles.

(2) The shape of the sieve openings and the particles.

(3) The properties of the particles.

(4) The loading on the sieve.

(5) The vibration of the sieve.

The Size of the Particles and the Sieve Openings

The relative size of the sieve mesh and the particles will greatly affect the results of sieving analysis. Markwick [12] conducted some of the earliest investigations for approximately equi-dimensional particles. The results of his experiments indicated that if the sizes of the particles are smaller than 90% of the sieve aperture, it will be very easy for them to pass through the sieve. From 90% to 95%, they will have some difficulties in passing the sieve. If the sizes of the particles are larger than 95% of the sieve aperture, passing through the sieve becomes very difficult for them.

With regard of the particle size distribution, the near mesh particles and the oversize particles play important roles in the sieving process [17]. As particles approach the limiting size of the sieve aperture, it becomes increasingly more difficult for these

particles to pass through the sieve [16]. This is because the near mesh particles are small enough to enter the sieve mesh but they may not be small enough to pass through the sieve mesh. These near mesh particles will stock in the meshes and make these blind openings. With increasing the sieving times, the small openings become ineffective and the sieving flow rate becomes slower.

If there are over-sized particles on the sieve screen, this blinding effect will be minimized and the rate of sieving will be enhanced dramatically. This is explained further on. N. Standish [17] carried out experiments to demonstrate this oversize effect. He began with a mixture have no over-sized particles. Then, during the sieving process, he added some oversize particles into the sieve, and found that the instantaneous rate of the sieving increased immediately. In order to understand the mechanism of this oversize particle effect, he also took high-speed films for the sieving process and then examined it at low play-back speeds. The predominant mechanism was observed to consist of the over-sized particles nudging the embedded near-mesh particles through and freeing the blind apertures for other particles to pass through. So the rate of sieving increased immediately.

The Shape of the particles and Sieve Openings

The shape of the aperture for a wire sieve is either square or somewhat rectangular. For equi-dimensional particles, the shape of the sieve aperture does not have a significant influence on sieving process. For irregular particles, the effective size of the sieve aperture will actually be smaller if the openings are rectangular. Therefore, it will be more difficult for these particles to pass through the sieve aperture [5].

With regard to the particle shapes, it is known that the flaky particles are more difficult to sieve than equi-dimensional particles, and elongated particles are most difficult to sieve [5,16]. This is because the dimensions for these irregular particles are not the same in all directions. They may be will pass through a mesh in one direction, but they probably cannot pass the sieve in all the other directions.

The Load on the Sieve

It is clearly indicated by F. A. Shergold [16] from his investigations that the results of sieve analysis will be affected by the load on the sieve. The important factor is not the gross amount placed on the sieve, but rather the proportion that does not pass through the sieve readily.

When sieving fine particles, the load on the sieve becomes a very important factor in making an accurate sieve analysis and, consequently, it is important not to heavily overload the sieve. If the sieve is overloaded, the weight will tend to jam the oversize particles or the near mesh particles into the sieve openings and making them blind [2,16]. If the wire of the sieve is too fine, the weight could even damage the whole mesh. When sieving coarse particles, the load on the sieve is not so important since the chance that the sieve openings being blind are much smaller than sieving fine particles.

The Vibration of the sieve

The pattern and the speed of the vibration of the sieve also have important influences on the sieving process. With regard to the paten of the vibration, Kenneth T. Whitby [8] conducted some early experiments by using two kinds of sieving machines: the "Gyrator sifter" which has only circular motion (rotation), and the "Ro-Tap sifter" which combines

the vibration and rotation at the same time. The results of his experiments showed that the blinding effect of the "Gyrator sifter" occurs much faster than the "Ro-Tap sifter", and the sieving rate for the "Gyrator sifter" was about one half of the "Ro-Tap sifter".

With regard to the speed of motion, F. G. Carpenter et al. [4] carried out some early investigations on the "Ro-Tap sifter". A number of different materials with different particle shapes and particle sizes were examined with different speeds of the "Ro-Tap". The same behavior was found for all these material: under-sized particles which was retained on the sieve at the speed of approximately 150 taps/min. may be pass though the mesh at the speed of approximately 115 taps/min. [4].

1.2.5 Mathematical Governing Equations

Like all the other studies of granular material, the establishment of a complete mathematical model of the sieving process is very difficult because of the number of parameters that should be considered. Below is a description of several models which take into account certain specific parameters under certain conditions.

In 1954, Whitby [8] tried to derived a formula for the weight passing vs. time curve of the first region of sieving process. From experiments, he first indicated that the sieving rate in the first region was nearly a constant and obeyed the following relationship:

$$\text{Percentage passing} = a\,t^{b} \qquad (1\text{-}2\text{-}1)$$

where a represents the sieving rate constant, b is a constant nearly equal to 1 and t represents the sieving time. In order to express the sieving constant a into a mathematical formula, he reconsidered those variables which might be important for sieving process. As

a result of dimensional analysis, He suggested that the sieving rate constant might be a function of five dimensional groups, i.e.,

$$a = f[\frac{W}{SA_0}, \frac{S}{d}, \frac{A_0}{A}, \frac{T}{d}, \frac{A}{S^2}] \tag{1-2-2}$$

Here, W represents the total load on sieve; S represents the size of the mesh opening ; A_0 represents the area of the sieve opening ; d is the diameter of the flow particle; A is the area of the mesh; and T represents the bed depth on sieve.

For the usual sieve, $\frac{A_0}{A}$ is a constant, while $\frac{T}{d}$ and $\frac{A}{S^2}$ are so large that it is improbable that they would have any appreciable effects. So Equation (1-2-2) can be reduced to:

$$a = f[\frac{W}{SA_0}, \frac{S}{d}] \tag{1-2-3}$$

By studying the data of series experiments, Equation (1-2-3) was finally expressed as:

$$a = C_1 \frac{A_0 \rho S}{W} \left(\frac{S}{k_s \overline{d}_m} \right)^n \tag{1-2-4}$$

$$\frac{aW}{A_0 \rho S} = C_1 \left(\frac{S}{k_s \overline{d}_m} \right)^n \tag{1-2-5}$$

where ρ is the density of the particle, C_1 is a constant to be determined , $\overline{d}_m$ represents the mass mean diameter of the particles, and $k_s \overline{d}_m$ is the geometric mass mean of the particle size distribution.

By plotting the graph of $\left(\frac{aW}{A_0\rho S}\right)$ against $\left(\frac{S}{k_s\bar{d}_m}\right)$ on a log-log scale, C_1 can be determined as the intercept of this line with the line $\left(\frac{S}{k_s\bar{d}_m}\right)$=1. The slope of this line is n. Whitby also found from his experiments that those materials having a narrow size distribution had steeper slop of the line.

Kaye [6] derived another mathematical equation for granular spherical particles sieving on a perfect mesh near the end of sieving process (Region 2). He first assumed that the sieving rate is proportional to the probability of particles passing the mesh and this probability is a function of the method of shaking, the physical properties of the spheres, and the geometry of the sieving surface. The probability of the passage of particle of diameter m at time t is given by

$$P_{mt} = Af(D)f(N)f(m\alpha) \tag{1-2-6}$$

where $f(D)$ is the factor due to the particle-size distributions, $f(N)$ is the factor due to the number of particles on the sieve, $f(m\alpha)$ is the component of P_{mt} which relates to the relative size of the particle to the sieve aperture. Because the objective was to model region 2, the end of the sieving process, most of the particles which remain on the sieve are over-sized, and only a small amount of particles on the sieve are able to pass through the mesh. In this condition, $f(D)$ and $f(N)$ should be constants. And because the difference between the size of particles and the size of apertures dose not change significantly near the end of sieving process, it seems reasonable to assume that $f(m\alpha)$ is also a constant. Then P_{mt} should also be a constant.

$$P_{mt} = K \tag{1-2-7}$$

Therefore, the equation of the rate of sieving becomes:

$$\frac{dW_t}{dt} = K\left(W_t - W_r\right) \tag{1-2-8}$$

where Wt is the total weight of all the particles remains on the sieve at time t, Wr is the residual (the weight of the particles which can not pass through the sieve).

In 1985, Standish [17] further derived another equation for near mesh-sized particles from Kaye's theory. If all the particles remaining on the sieve are near-mesh particles, then Equation (1-2-8) can be rewritten in the following form:

$$-\frac{dW}{dt} = kW \tag{1-2-9}$$

where W is the total weight of particles (Note that $Wr = 0$ since all the particles can fall through the sieve). From Equation (1-2-9), the individual rate equations for different sizes of particles (of sizes $R_1, R_2, R_3, \ldots\ldots, R_n$) can de written as:

$$\frac{dW_1}{dt} = k_1 W_1 \; ; \; \frac{dW_2}{dt} = k_2 W_2 \; ; \; \frac{dW_n}{dt} = k_n W_n \tag{1-2-10}$$

where k_1, k_2, k_3,.....k_n are rate constants for particles of size $R_1, R_2, R_3, \ldots\ldots, R_n$, respectively. and the sieving rate of all the particles at time t becomes

$$\frac{dW}{dt} = kW = k_1 W_1 + k_2 W_2 + k_3 W_3 + \ldots\ldots\ldots \tag{1-2-11}$$

where $W = \sum_{i=1}^{n} W_i = W_1 + W_2 + \ldots\ldots + W_n$

1.3 M. Richman and L. Wang's Theory

Recently, a theory and a mathematical equation which governing the rate of sieving was developed by M. Richman and L. Wang using kinetic theory [15]. Their theory accounts for loading sieve, vibrating intensity, and particle inelastic modeled by a normal restitution coefficient e and mean sieve aperture s. In their theory, an assembly of identical, inelastic spheres are vibrated and thermalized by a bumpy boundary which contains hemispheres that are randomly arranged. The empty spaces between the hemispheres allow the particles fall through.

The bumpy boundary randomly oscillates with instantaneous velocity c. Here, an Maxwilliam distribution function $p(c)$ is introduced to govern the boundary velocity.

$$p(c) = \frac{1}{(8\pi^3\beta)^{\frac{1}{2}}} \exp\left[\frac{-1}{2}(c-U)\cdot B^{-1}\cdot(c-U)\right] \tag{1-3-1}$$

$$B \equiv \int (c-U)\otimes(c-U)p(c)dc \tag{1-3-2}$$

where U is the mean velocity of the boundary, B is defined as the full second moment of the boundary fluctuation velocity and $\beta \equiv \det(B)$. By also governing the velocities of flow particles u with an Maxwilliam distribution function and ignoring the corrections due to special variations of the mass mean velocity, the temperature, and the density, the frequencies which the particles fall through the sieve can be defined as:

$$\phi \equiv \frac{v\cdot N}{\sqrt{2TN\cdot b\cdot N}} \tag{1-3-3}$$

where v is the "slip velocity" through boundary: $v = U\text{-}u$, T is the granular temperature, N is the inward normal vector, and $b = I + B/T$. The mass flow rate Q then becomes

$$Q = \frac{\rho(TN \cdot b \cdot N)^{\frac{1}{2}}}{(2\pi)^{\frac{1}{2}}}\left[1-\left(\frac{1+r}{1+\Delta}\right)^2\right]\left[\exp(-\phi^2)+\pi^{\frac{1}{2}}\phi \cdot erfc(-\phi)\right] \qquad (1\text{-}3\text{-}4)$$

where $r=\sigma/d$, and $\Delta = s/d$, σ is the diameter of the flow particles, and s is the mean space of the sieve apertures. For the special case that the dimensional space Δ is only slightly greater than the dimensional diameter r, the normal velocities to the bumpy boundaries and the flow rate through the boundaries are relatively small. Under this circumstance, the influence of the factor ϕ can be neglected (ϕ=0). The dimensional mass flow rate then becomes

$$q \equiv \frac{Q}{\rho_p(\sigma g)^{\frac{1}{2}}} = \frac{\nu(\tau N \cdot b \cdot N)^{\frac{1}{2}}}{(2\pi)^{\frac{1}{2}}}\left[1-\left(\frac{1+r}{1+\Delta}\right)^2\right] \qquad (1\text{-}3\text{-}5)$$

Once the mass flow rate is determined, the mass hold-up at the time $t+dt$ can be calculated as:

$$m_t(t+dt) = m_t(t) - q(t)dt \qquad (1\text{-}3\text{-}6)$$

The sieving rate in the first region is also significantly influenced by dimensional parameters Vn and Vt which concern the vibrating intensities in normal and tangential directions. The definition of Vn, Vt in their theory will be further descried in Chapter 3. Then we will compare our simulation results with their predictions.

1.4 Outline of Thesis

Chapter 1 contains the introduction and motivation of these studies, and a review of the relevant literature. In Chapter 2, the force model is introduced, the boundary (or sieve mesh) configuration is described, and the weight calculation method used in the dynamic

computer simulation code is provided. The results of simulation are reported in Chapter 3, and the comparisons with Richman's theoretical predictions also in Chapter 3. Chapter 4 includes the summary, the conclusions, and the suggestion for future research.

CHAPTER 2

THREE DIMENSIONAL PARTICLE DYNAMIC SIMULATION METHOD

2.1 History and Introduction

The development of the particle dynamic simulation method has a long history. The traditional molecular dynamic simulation method was developed in the middle of the century and was used for studies of dense fluid for about 40 years. In order to study the behavior of granular solid particles, the particle dynamic simulation method was derived from the molecular dynamic method in the 1970's. The major difference between these two methods is their interaction models. In the molecular dynamic method, the particles are perfectly elastic. The total energy of the system is conserved. No kinetic energy is lost during a collision. In the particle dynamic simulation method, the particles are inelastic, similar to real particulate. During a collision, a fraction of the initial kinetic energy is irreversibly lost as heat, elastic or plastic strain energy, acoustic energy or even light.

In the particle dynamic simulation method, two types of force interaction models are used. The "Hard Sphere Model" assumes that the particles are rigid bodies with infinite stiffness: the collisions are instantaneous and the particles do not overlap during a collision. This kind of simulation proceeds by irregular time jumps corresponding to the time period between one collision and the next. Velocities of particles after collision are determined by the normal and tangential restitution coefficients, a friction coefficient, and the velocities of particles before collision.

In the "Soft Sphere Model", there is a force scheme that acts during collision only. The equations of motion are integrated at regular time intervals. Each collision has a finite duration and the particles are allowed to overlap by an amount depending on their stiffness. The outcome of a collision (i.e. post-collision velocity) depends on the parameters in the force law which does not always have an explicit relationship with material properties used in the hard sphere mode. The maximum overlap may not exceed approximately one percent of the diameter of the colliding particles in accordance with the behavior of real particles.

The simulation code used in this work comes from Walton and Braun's [16] original uniform shear code. H. J. Kim modified parts of the diagnostic procedures for his study of Couette flow [17]. Y. D. Lan further modified the code so that it can handle different kinds of boundary conditions, and can calculate the velocity and temperature field in different cases for a vibrating bed [15]. The recent modifications we made for our studies include:

- Redefining and altering several control flags so that the "pouring" and "shaking" processes can be run separately.
- Changing the mode of vibration from one dimension to three dimensions.
- Subtracting out the particles' initial deviatoric velocities.
- Changing the configuration of bumpy boundary conditions.

- Incorporation of diagnostics to calculate the collision frequency, the mass flow rate, the mass hold up, and a few other time-related functions.

2.2 The Force Models

2.2.1 Normal Force Model

In the "Soft Sphere Model" developed by Walton [18], a "Partialy Latching-Spring Model" is used to estimate the interactive force in collisions,.and to approximate the energy lose due to inelastic collisions in "normal" direction, i.e., the direction defined by the line joining the center of two interacting spheres. In this force model, the collision process is divided into two periods: the "Compression" period and the "Restoration" period. Here, the overlaps between particles are measured as the particle deformations . The "Compression" period starts at the beginning of a collision. In this period, the relative velocity between two particles decreases as the particles approach each other. When the relative velocity becomes zero and the overlap reaches its maximum value in the collision α_{max}, the "Compression" period ends and the "Restoration" periods starts.

The interaction forces in the compression and the restoration periods are calculated as:

$$\begin{cases} F_1 = K_1 \cdot \alpha \\ F_2 = K_2 \cdot (\alpha - \alpha_0) \end{cases} \qquad (2\text{-}2\text{-}1)$$

where F_1 is the force in "Compression" period, F_2 is the force in "Restoration" period, K_1 and K_2 are the normal stiffness coefficients in the two periods, respectively, α is the overlap between the particles, and $_0$ is the residual overlap. Note that $_0$ is initialized to

zero automatically when the restoring force F_2 goes to zero because permanent deformations of particles are not allowed. Figure 2.1(a) (b) demonstrates the relationship between forces and deformations during collisions. In Figure 2.1(a) (b), K_1 is equal to the slope of line $\overline{ab}$, K_2 is equal to the slope of line $\overline{bc}$I. As shown in the figure, K_2 is always larger than K_1. The energy loss during this collision is equal to the area of Δabd minus the area of Δabc.

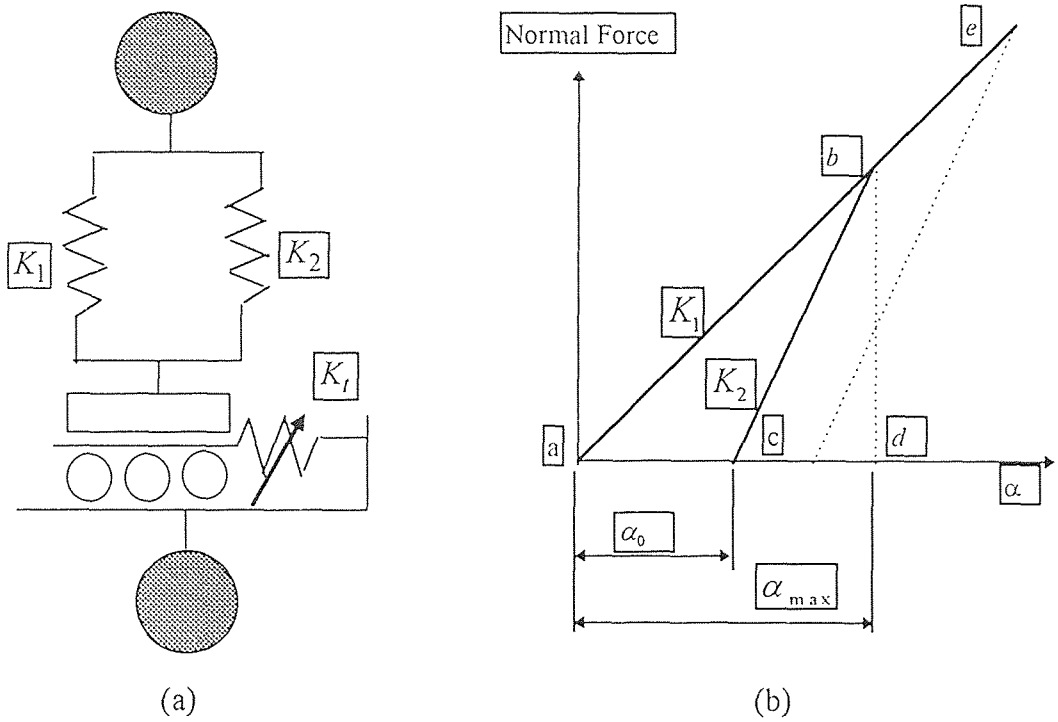

Figure 2.1 (a) The Partially Latching-Spring Model
(b) The Normal force to Overlap diagram

To determine the interactive force, F_1 and F_2 are both calculated for each time steps during the collision, and the smaller one is chosen as the normal interactive force.

(a) In the "Compression" period from $\alpha_0 = 0$: (from a to b)

Since K_2 is larger than K_1. and α_0 is equal to zero, then

$$\begin{cases} F_1 = K_1 \cdot \alpha \\ F_2 = K_2 \cdot (\alpha - 0) = K_2 \cdot \alpha \end{cases}$$

It is clear that F_2 is larger than F_1., so the normal interactive force will then be equal to F_1.

(b) In the "Restoration" period : (from b to c)

In this period, F_2 is always smaller than F_1 as it is shown in Figure 2.1. F_2 will be chosen as the normal interactive force

(c) In the "Recompression" period from $\alpha_0 \neq 0$:

If the two particles are recompressed during the "Restoration" period (from *b* to *c*), the loading path will go backwards(from c to b), and F_2 will be chosen as the normal force since F_2 is stll less than F_1. After reaching point *b*, F_1 will be chosen as the normal force again because it is now smaller than F_2, and the loading path goes from point *b* to point *e*.

2.2.2 Tangential Force Model

The tangential interactive force model developed by Walton and Braun [18] and used in the code, was derived by Mindin and Deresiewicz [13]. In this model, the tangential force at time *t* is related to the tangential stiffness, the surface displacements and the tangential force at the last time step *t-dt*. The tangential stiffness decreases with the surface displacement, and when it becomes zero, full sliding takes place.

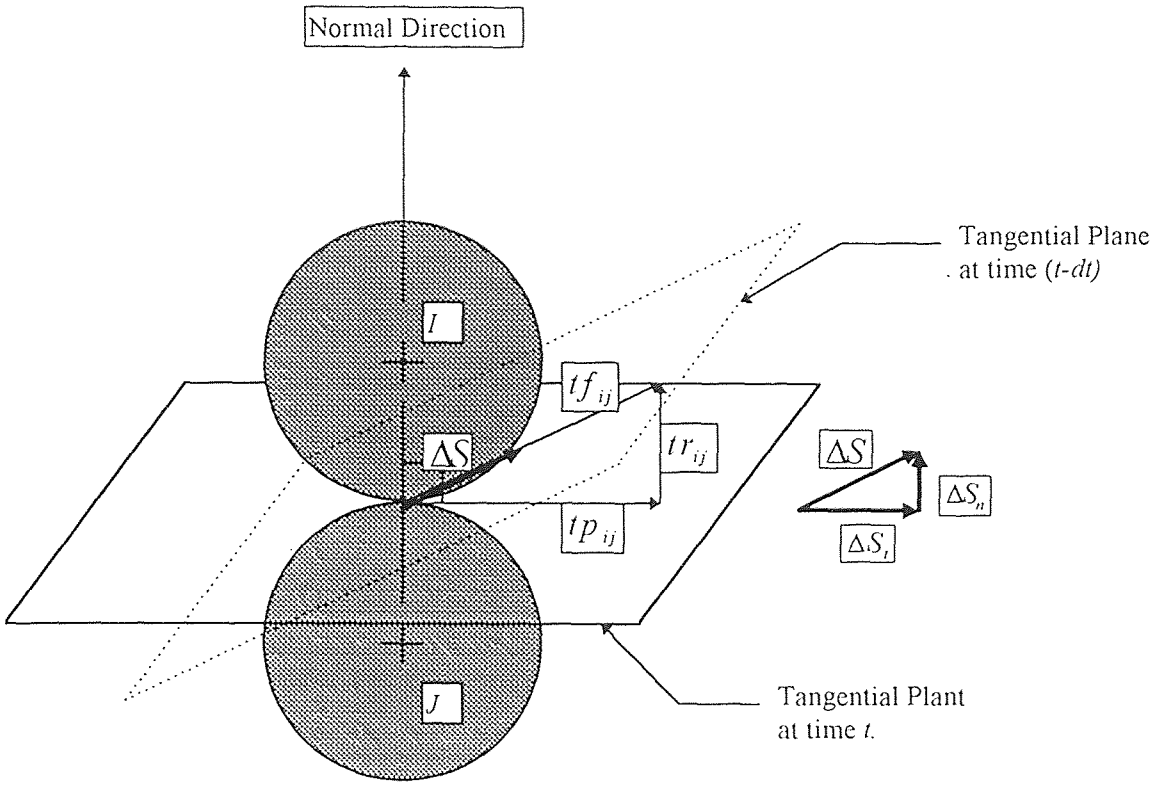

Figure 2.2 The Tangential Force Model

Figure 2.2 demonstrates the collision and the tangential plane between two particles. The tangential plane is always perpendicular to the line which connects the centers of the two particles, and it will be changed if the particles move to new positions. The tangential force at current time step ft_{ij} is calculated from the tangential force at the last time step (*t-dt*). In Figure 2.2, tf_{ij} is the tangential force at the last time step, and tp_{ij} is its projection onto the current tangential plane. ΔS is the total tangential displacement at time (*t-dt*), $(\Delta S_n, \Delta S_t)$ are its components in the plane's normal and parallel directions. The force ft_{ij} is then calculated as

$$ft_{ij} = tp_{ij} + K_t \cdot (\Delta S_t) + K_o \cdot (\Delta S_n) \qquad (2\text{-}2\text{-}2)$$

where K_t is the tangential stiffness at current time step, and K_o is the initial tangential stiffness. In the code, K_o has a fixed value which is computed as :

$$K_0 = K_1 \cdot ratk \tag{2-2-3}$$

where K_1 is the compression normal stiffness coefficient, and *ratk* is a input value. The value of K_t is calculated as:

$$K_t = K_0 \cdot scalek \tag{2-2-4}$$

$$scalek = \left(1 - \frac{T - T^*}{\mu N \pm T^*}\right)^{\frac{1}{3}} \tag{2-4-5}$$

where μN is the maximum Coulomb friction, T is the smaller value of μN and tf_{ij}, which is the fiction force at the last time step. T^* is equal to zero initially, and subsequently, it is set to the value of T when the slip reverses its direction. The sign of T^* is also determined by the direction of slip.

The components of ft_{ij} in *x*, *y*, *z* directions are then calculated by,

$$\begin{cases} ft_{ij_x} = tp_{ij_x} + K_t \cdot (\Delta S_t)_x + K_o \cdot (\Delta S_n)_x \\ ft_{ij_y} = tp_{ij_y} + K_t \cdot (\Delta S_t)_y + K_n \cdot (\Delta S_n)_y \\ ft_{ij_z} = tp_{ij_z} + K_t \cdot (\Delta S_t)_z + K_o \cdot (\Delta S_n)_z \end{cases} \tag{2-2-6}$$

or

$$\begin{Bmatrix} ft_{ij_x} \\ ft_{ij_y} \\ ft_{ij_z} \end{Bmatrix} = \begin{Bmatrix} tp_x \\ tp_y \\ tp_z \end{Bmatrix} + \begin{Bmatrix} K_t & K_o \end{Bmatrix} \cdot \begin{Bmatrix} (\Delta S_t)_x & (\Delta S_n)_x \\ (\Delta S_t)_y & (\Delta S_n)_y \\ (\Delta S_t)_z & (\Delta S_n)_z \end{Bmatrix} \tag{2-2-7}$$

2.3 The Time Step

The simulation time step dt is defined by the following equation :

$$dt = \frac{\pi \cdot e}{n} \cdot \sqrt{\frac{\pi \cdot d^3 \cdot \rho}{12 \cdot K_1}} \qquad (2\text{-}3\text{-}1)$$

where d is the diameter of the smallest particle, e is the normal restitution coefficient, ρ is the density of the material, K_1 is the loading normal stiffness coefficient, and n is the number of time steps during one collision. The value of n can be chosen by the user, where a reasonable value lies between 15 and 30. If n is too large, the time step dt will be too small and the computing time too large. If n is too small or dt too large, the resulting integration becomes inaccurate. Detailed descriptions about the derivations of Equation (2-3-1) can be found in [10].

2.4 The Boundary Conditions

Three kinds of boundary conditions can be generated by the code: periodic boundaries, plane walls, and bumpy walls. These boundary conditions are capable of modeling most of the real situations encountered.

2.4.1 Periodic Boundary Condition

If the number of boundary particles is set equal to zero in input file *I3ds*, then periodic boundaries are employed. The idea of the periodic boundary is extremely important for particle dynamic computer simulations. In effect, the use of this type of boundary allowed us to model behavior in real system having hundreds of thousands of particles by using

only a small representative sample of a few hundreds particles. This then permits optimum use of the computer's limited memory, and speed. The computational cell in this investigation may be considered as a sample volume of the bulk particle mass on top of the sieve.

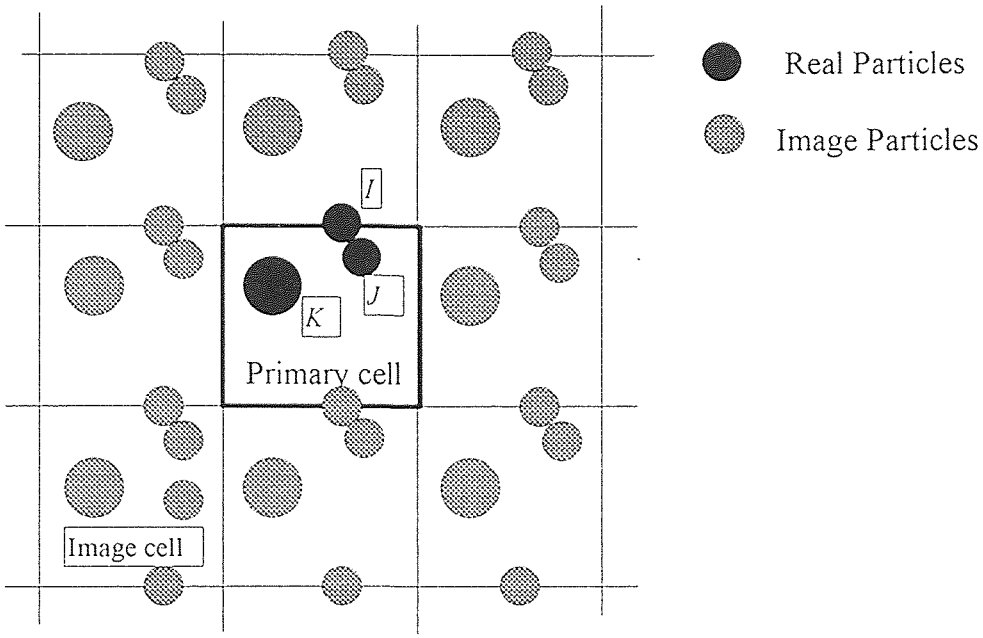

Figure 2.3 Particles and their Images for Periodic Boundary Condition

Through the use of periodic boundaries, we can simulate a system of "infinite" size with only a small number of particles since the effects of real walls are not present. Figure 2.3 is a two-dimensional representation of particles and their images under the periodic boundary condition. A primary cell is used with an "infinite" number of identical "image" cells surrounding it. All of the flow particles are originally placed in the primary cell. If a particle leaves the primary cell from one side, its image enters the primary cell on the opposite side.

Collisions can occur between either the particles or their images. In the code, the distances in *x*, *y*, *z* directions between real particles *I* and *J* are calculated as:

$$\begin{cases} r_x = x(J) - x(I) \\ r_y = y(J) - y(I) \\ r_z = z(J) - z(I) \end{cases} \tag{2-4-1}$$

Suppose the lengths for the cell in *x*, *y*, *z* directions are *xcell*, *ycell* and *zcell*. Then the nearest distances in *x*, *y*, *z* directions between these two particles or their images is given by:

$$\begin{cases} r_x = r_x - xcell \cdot \mathrm{int}(\dfrac{r_x}{xcell}) \\ r_y = r_y - ycell \cdot \mathrm{int}(\dfrac{r_y}{ycell}) \\ r_z = r_z - zcell \cdot \mathrm{int}(\dfrac{r_z}{zcell}) \end{cases} \tag{2-4-2}$$

from which the nearest distance r_{ij} is then computed as:

$$r_{ij} = \sqrt{r_x^2 + r_y^2 + r_z^2} \tag{2-4-3}$$

If the value of r_{ij} is smaller than *rad(I) + rad(J)*, then particles *I* and *J* have collided. The code then calculates the normal and tangential forces between the two particles.

2.4.2 Plane Boundary

If the number of boundary particles is set equal to unit in *I3ds*, then plane impenetrable walls are used which can reflect the colliding flow particles and impact to them both normal and tangential forces. In effect, the wall is represented by a particle of infinite mass which meets a flow particle, and consequently , any imposed motion of this boundary particle will not be affected by a collision. Figure 2.4 shows a picture of the plane

boundary particle and a colliding flow particle. As it is shown in Figure 2.4, the line which connects the centers of the boundary particle and the colliding flow particle is perpendicular to the plane boundary. The flow particle is in contact with the plane boundary if the distance between the centers of these two particles is equal to or smaller than the sum of their radii $(r_i + r_j)$.

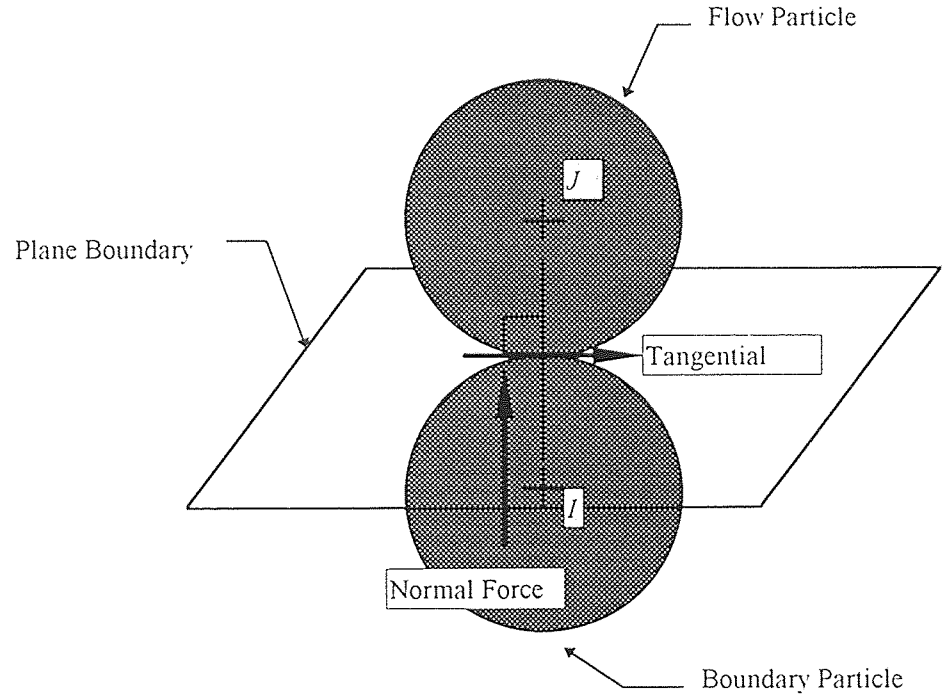

Figure 2.4 Collision on Plane Boundary

2.4.3 Bumpy Wall

If the number of boundary particles is greater than unity, then this boundary is a bumpy wall. Two configurations of bumps can be selected: a triangular lattice or a rectangular lattice in the plane. The bumps are actually hemispheres fixed at the same y-locations as

shown in the two-dimensional representation of Figure 2.5. Figure 2.6 (a)(b) is a diagram of the two types.

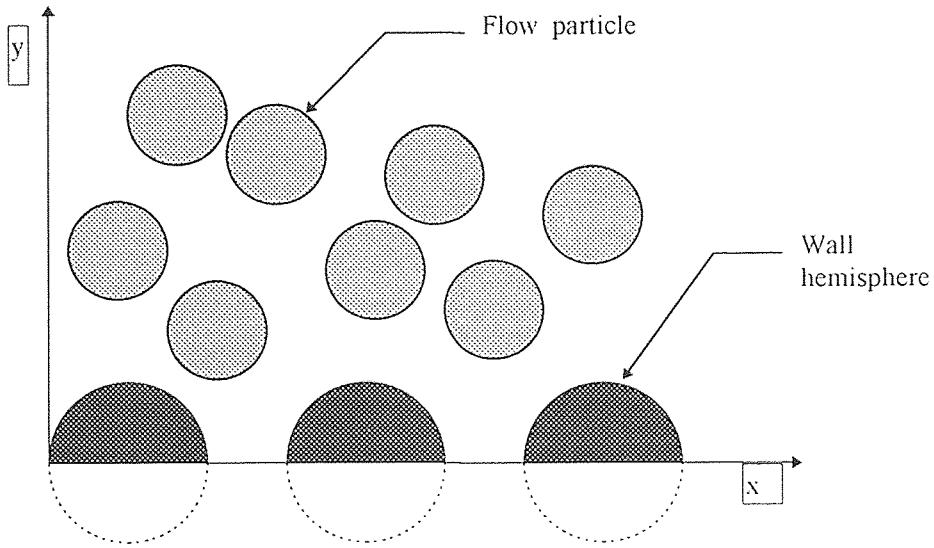

Figure 2.5 The Bumpy Walls

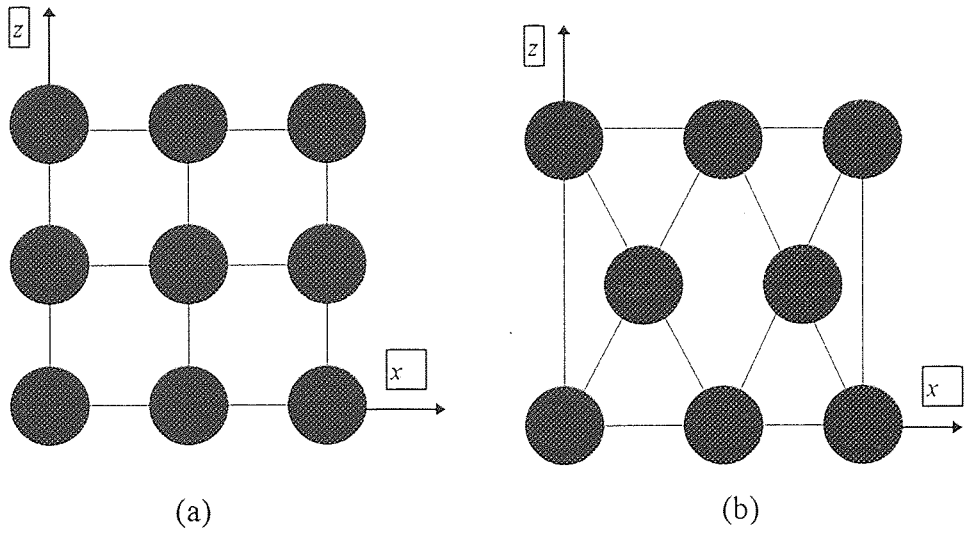

Figure 2.6 (a) Configuration of Rectangular Bumpy Boundary
(b) Configuration of Triangular Bumpy Boundary

2.5 Structure of the Sieve Computational Cell

The structure of the sieve computational cell is shown in Figure 2.7, while Figure 2.8 depicts an area of the vibrating sieve mesh. In this study, a rectangular lattice was chosen.

Size of the Cell

In Figures 2.7 and 2.8, *xcell, ycell* and *zcell* are lengths of the cell in x, y and z directions, *db2* is the diameter of boundary particles and S is the linear distance between the centers of two adjacent boundary particles along x and z directions. The value of *xcell* is the same as *zcell* in our studies and it is determined by using the following formula :

$$xcell = zcell = nsieve \cdot S \qquad (2\text{-}5\text{-}1)$$

where *nsieve* is the number of sieve apertures (or unit cells) along x and z directions. The value of *nsieve* is a user input in *I3ds*. In Figure 2.8, the value of *nsieve* is equal to four.

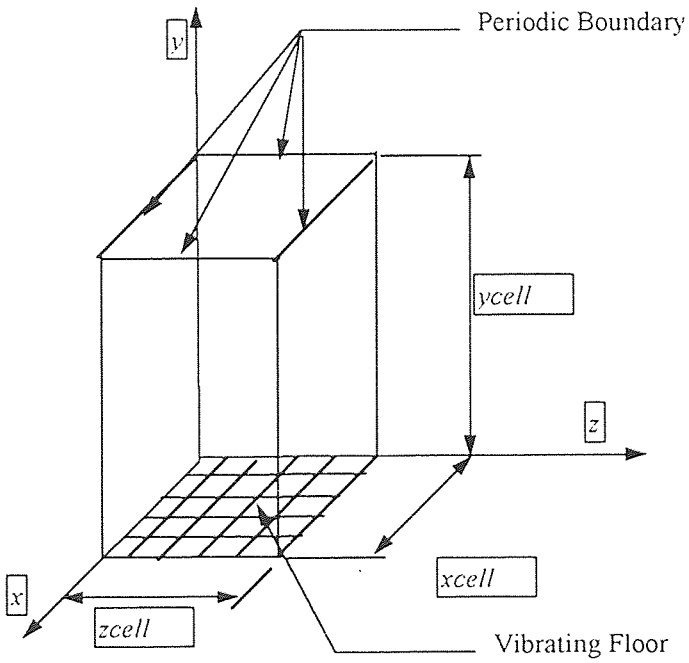

Figure 2.7 Model of the Computational Sieving Cell

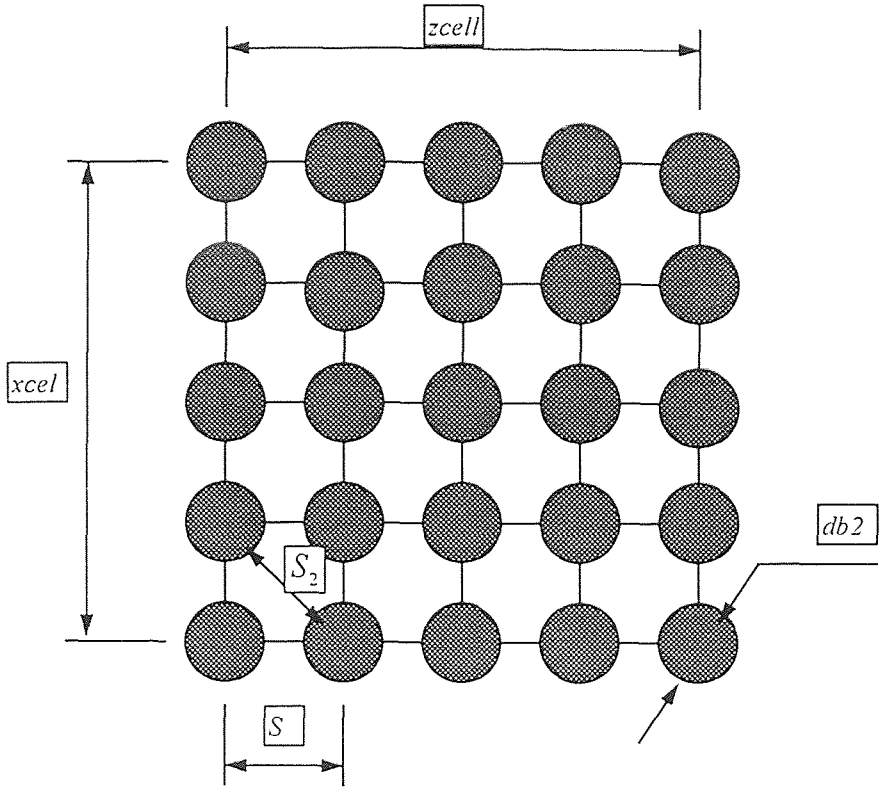

Figure 2.8 Model of the Sieve Configuration

Number of Y Zones

Quantities, such as granular temperature, velocity and solids fraction, are depth dependent i.e. their values are determined as a function of y. For this purpose, the computational cell is divided into a number of zones along the y direction. Figure 2.9 demonstrates these zones in our cell. The number of zones *nyzone* is input in *13ds* , and the height of each zone is calculated as

$$yzone = \frac{ycell}{nyzone} \tag{2-5-2}$$

In the code, the value of *nyzone* has an upper limit *myzone* which is set in the file *S3dscmm.*, and the value of *yzone* has to be larger than the diameter of the flow particle so

that the flow particle can not occupy more than two zones at the same time. Otherwise, the volume and the mass of the particle can not be calculated.

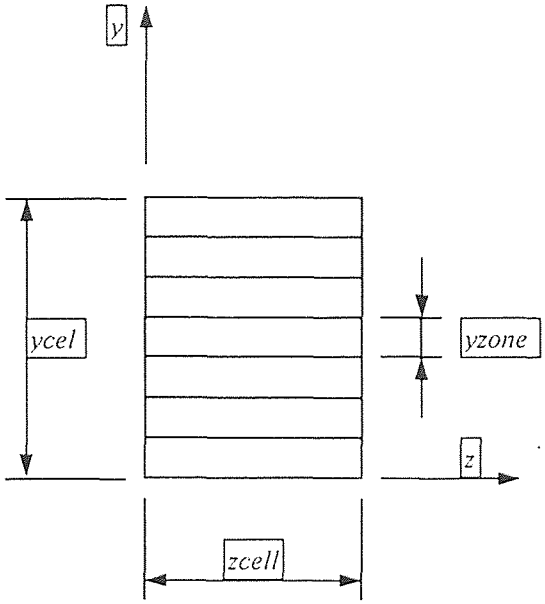

Figure 2.9 *Y*-Zones Used to Compute Depth Profiles.

Sieve Aperture

Figure 2.10 shows a sieve aperture which is formed by the space between the boundary particles. Here , S_2 is the diameter of the aperture, whose value can be calculated with the formula:

$$S_2 = \sqrt{2}\,S - db2 \qquad (2\text{-}5\text{-}3)$$

where *db2* is the diameter of boundary particles. In the pouring procedure, the value of S_2 must be smaller than the diameter of the flow particles so that the flow particles can not fall through the apertures. In the shaking procedure, S_2 must be greater than the diameter of the flow particles so that the flow particles can fall through the sieve apertures.

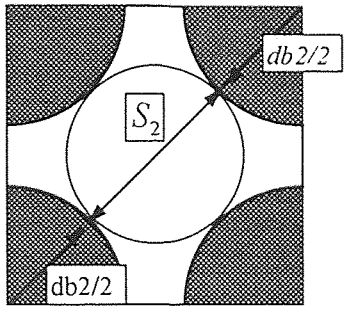

Figure 2.10 The Sieve Aperture

2.6 Subroutines and Procedures for the Simulation

The simulation process can be divided into a few distinctive steps. The first step is to read in the values of all the parameters relating the system and the material properties. The second step is the pouring procedure, where random coordinates are generated in the computational cell for all the flow particles, and then these particles are allowed to fall under gravity to an initial configuration. After this, the initial configuration is shaken with variable frequencies and amplitudes determined as input by the user. The particles' link lists (Sect. 2.6.4) are generated and the interactive forces, the particles' velocities, and other diagnostic parameters are calculated for each time step *dt* in both pouring and shaking procedures. The program can also be restarted for a continued run, or if it stops unexpectedly. Table 2.1 contains the values of several important control parameters to run the code. For example, *ipour* must be zero when running the pouring procedure. In the following sections, we describe in detail the procedures and the important computational methods in our simulation. At the same time, we also introduce the subroutines in the code and their functions.

Table 2.1 Parameters for Running each Process

Procedure	*ipour*	*istart*
Pouring	0	0
Shaking	1	0
Restart	0 or 1	1000

2.6.1 Subroutines and their Functions

In this section, a list of the subroutines in the code and simple descriptions about their functions will be given in Table 2.2

Table 2.2 Descriptions of Subroutines

Subroutine	Descriptions
Bound	This subroutine assigns the coordinates, velocities, and other parameters for the boundary particles.
Datain	This subroutine reads all the input data from "*I3ds*"
Datasav2	This subroutines writes the outputs data to all the output files.
Deletem	This subroutines loops through all near neighbors in the link list, and delete the near neighbors if their distance are beyond the maximum distance. It is only used when the maximum distance has been reduced to save the total memory which is used for storage.
Diagnos2	This subroutine calculates all the diagnose parameters like, the granular temperature, the velocities for each zone, and the stress tensors.

Table 2.2 Descriptions of Subroutines - continued

Dumpread	This subroutine reads all the needed information for restating the program from the file "*D3ds1000*". It is only used when *istart* is not equal to zero.
Findrad	This subroutine expands the radii for particles until they reach their predetermined values which were set in "*I3ds*".
Forces	This subroutine calculates the normal and tangential interacting forces between particles.
Init	This subroutine initializes general parameters, initial coordinates, and fluctuation velocities of the flow particles. It also calculates the time step and the number of zones.
Initcum1	This subroutine initializes all the short-term cumulative averages. It is called for every time interval *dtout*.
Initcum2	This subroutine is used to initialize the long-term cumulative averages in the code.
Initstep	This subroutine is used to initialize the integration steps in the code. It also established the index of the zones for calculating the zone diagnostics.
Integ1	This subroutine performs an iterative integration to calculate the particles' velocities.

Table 2.2 Descriptions of Subroutines - continued

Integ2	This subroutine calculates the coordinates of particles at the end of the current time step.
Rand	This subroutine is a random number generator which is used by *Init* to generate the initial random coordinates for particles.
Update	This subroutine updates the particles' link lists for every update time step *dtup*.

2.6.2 Dimensions and Data Input

The file *S3dscmm* provides dimensions for all the variables and arrays that will be used in the run. The main routine *Sieve* opens all the input and output files. Before starting the program, all values of the parameters, the properties of the material, the size of the computational cell, the number of particles, the initial velocities, the amplitudes and frequencies of the vibrating floor, etc. should be determined and assigned into the file *I3ds*. Once the program is running, all these parameters will be read by the subroutine *Datain*.

2.6.3 Generating an Initial Configuration

As previously mentioned, the pouring procedure is used to establish the initial flow particle configuration consisting of the positions of the centers of all the flow particles. In this procedure, subroutine Init first assigns a number or index for each particle. Then it begins to generate random coordinates of the centers and initializes the velocities for every

flow particle to zero. Once the random coordinates have been generated, it begins to calculate the distances between particle pairs in order to find an appropriate radius for each particle. This is a precursor to modifying the center positions of the particles so as to enable them to be assigned their prespecified radii , *radz( )*, which is read in from *I3ds*. If particle *J* is the nearest particle to particle *I* and the distance between the centers of these two particles is r_{ij}, then the radii of the two particles *rad(I)* and *rad(J)* are set to r_{ij} */2*. If r_{ij} */2* is larger than or equal to the radii *radz(I)* and *radz(J)*, then *rad(I)* and *rad(J)* are set equal to *radz(I)* and *radz(J)* respectively. If r_{ij} */2* is smaller than the initial radii *radz(I)* and *radz(J*), then the subroutine *Findrad* is called to increase *rad(I)* and *rad(J)* by actually making use of the force interaction routines in the code. As *rad(I)* and *rad(J)* are increased, ensuing overlaps result in repulsive force between *I* and *J* which consequently causes them to move apart. This expansion process is repeated at each time step until the radius of every particle is equal to its assigned value in *I3ds*. After that, the particles are allowed to fall under the gravity to the floor of the computational cell until they have very little kinetic energy and are essentially at "rest". This complete the pouring process. The positions of all the flow particles are saved in the output file *Zposition* as an initial configuration needed for the shaking procedure. We note that *Zposition* is modified every *dtout* time steps by adding each new configuration. In order to run the shaking procedure, the last configuration file output to *Zposition* is copied into a file designated as *Xyz*

2.6.4 Shaking

In the shaking procedure, initial positions of all the flow particles are read from the file *Xyz*. During shaking, the vibrating floor is vibrated with a specified type of motion. Velocities of the vibrating floor are calculated in subroutine *Integ2* as follows:

$$\begin{cases} v_x = vampx \cdot cos(omegax \cdot t + angx) \\ v_y = vampy \cdot cos(omegay \cdot t + angy) \\ v_z = vampz \cdot cos(omegaz \cdot t + angz) \end{cases} \quad (2\text{-}6\text{-}1)$$

$$\begin{cases} omegax = 2 \cdot \pi \cdot frqx \\ omegay = 2 \cdot \pi \cdot frqy \\ omegaz = 2 \cdot \pi \cdot frqz \end{cases} \quad (2\text{-}6\text{-}2)$$

$$\begin{cases} vampx = a_x \cdot omegax \\ vampy = a_y \cdot omegay \\ vampz = a_z \cdot omegaz \end{cases} \quad (2\text{-}6\text{-}3)$$

where a_x, a_y, a_z are the amplitutes of oscillating in *x*, *y* and *z* directions; *vampx*, *vampy* and *vampz* are the amplitudes of velocities in *x*, *y* and *z* directions; *omegax*, *omegay*, *omegaz* are the angular velocities of the vibrating floor in *x*, *y*, *z* directions; *angx*, *angy*, *angz* are the leading phase angles in *x*, *y*, *z* directions; and *frqx*, *frqy*, *frqz* are the oscillating frequencies of the vibrating floor in *x*, *y*, *z* directions. The values of these parameters are set in the input file *I3ds*.

2.6.5 Generating the Link List

The link list is an array containing the neighbors of each particle and is used for collision detection. To establish this list, subroutine *Update* first calculates the distances between the centers of all the particles. If the distance between two particles is smaller than the

value of the search radius (denoted by *search)* which is read in from *13ds*, then these two particles are neighbors and they are in each others' link list. For example, in Figure 2.11, the link list of particle *I* contains (*J, K, L, N)*, and the link list for particle *L* contains (*I, J, N, O)*. Although particle *N* is not in contact with particle *I*, it is still in particle *I*'s link list because the distance between them is less than the search radius.

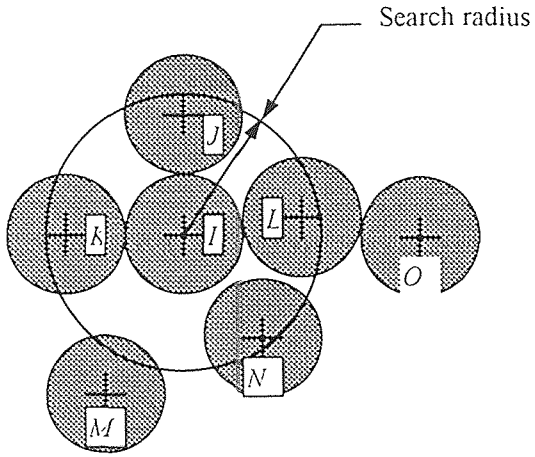

Figure 2.11 The Graph of Link Lists

All the link lists are updated after each time interval *dtup*. This updating time step *dtup* is calculated in subroutines *Init* and *Update* by using the formula

$$dtup = \frac{search}{2 \cdot vmaxx} \qquad (2\text{-}6\text{-}4)$$

where *vmaxx* is the maximum root mean square deviatoric velocity at the last time step which is calculated in the Subroutine *Diagnose2*. In the code, there is an upper limit *dtupmax* which is 200 times the value of *dt*. The value of *dtup* can not exceed this upper limit; otherwise it is set equal to *dtupmax*.

2.6.6 Calculating the Forces and the Diagnostic Parameters

After the link lists of particles are established, subroutine *Forces* calculates the interaction forces between each flow particle and the neighbors in its link list. After that, the resulting force which acts on each particle at the current time step can be determined. Subroutine *Integ1* finds the velocities of every particle from these forces and Newton's law. Subroutine *Diagnos2* calculates all the diagnostic variables like granular temperature, solid fraction, and the mass mean particle velocity for each zone at the current time step. Detail on these quantities can be found in [10,13]. Once the velocities are determined, subroutine *Integ2* determines the displacements of all the particles and their new positions at the next time step ($t+dt$) with the formulas below.

$$\begin{cases} dx_i = v_{x_i} \cdot dt \\ dy_i = v_{y_i} \cdot dt \\ dz_i = v_{z_i} \cdot dt \end{cases} \tag{2-6-5}$$

$$\begin{cases} x(i) = x(i) + dx_i \\ y(i) = y(i) + dy_i \\ z(i) = z(i) + dz_i \end{cases} \tag{2-6-6}$$

2.6.7 Data Output

If the simulation time t is larger than the time for output *tout*, then subroutine *Datasav2* will print out all the data to the specified files. The time for output *tout* is initialized to zero in *Init*. After that, it will then be increased by *dtout* when the subroutine *Datasav2* is called, i.e.,

$$tout = tout + dtout \tag{2-6-7}$$

Note that the value of *dtout* is assigned in *13ds*.

2.6.8 Restarting the Code

The program is run on a UNIX platform for several consecutive days to complete one case of study (depending on the time desired for the run). In the event of a system failure, dump file *D3ds* is written every time interval *dtdump*. Once the program stops (either unexpectedly or when *tmax* is reached), the program may be restarted by setting the value of *istart* in *I3ds* to 1000, and by renaming the file *D3ds* to *D3ds1000*. Subroutine *Dumpread* will then read all the data from *D3ds1000* and the program is restarted from the time step when *D3ds* was last updated.

2.6.9 Other Subroutines

In addition to all the subroutines mentioned above, there are some other subroutines which have important functions. Subroutine *Bound* assigns the initial positions and velocities for the boundary particles. Subroutine *Rand* is a random number generator which is used by *Init* to generate the random positions for flow particles. Subroutine *Initstep* is used to initialize the integration steps for all subroutines. Subroutine *Initcum1* and *Initcum2* are used to initialize short term and long term averages. Subroutine *Deletem* loops through all near neighbors in the link list and deletes contacts that are beyond the maximum distance.

2.7 The Method of Calculating Collision Frequency with the Floor

In order to calculate the collision frequency, several new variables are incorporated into the code. The flag *Ic(I,J)* indicates the contact status between particles *I* and *J*; *Ic(I,J)* is equal to unity if particles *I* and *J* are in contact, and zero otherwise. The quantity *tcby0* is

the instantaneous number of collisions (i.e. number of contacts) on the floor *(y=0)* at time *t*, and *tcby0t* is the accumulated number of collisions at this boundary from time t_0 to *t*. The array *tczone(Y)* is the instantaneous number of collisions in zone *Y* at time *t*, and *tczonet(Y)* is the accumulated number of collisions in zone *Y* from t_0 to *t* (Note: $t-t_0$ = *dtout*). The variables *tcby0 and tczone(Y)* are initialized to zero for each *dt*, while *tczone(Y)* and *tczonet(Y)* are initialized to zero for each output time step *dtout*.

The number of collisions at time t

In the code, subroutine *Forces* checks the flag *Ic(I,J)* and the distance between each pair of particles *(I,J)*, and determines the number of collisions at each time step. As previously described, the nearest distance r_{ij} between particles *I* and *J* or their images can be calculated by Equation (2-4-2) and Equation (2-4-3).

Case 1. If the distance r_{ij} is larger than the sum of the radii of these two particles *rad(I)+ rad(J)*, then they are not in contact during this time step, and Subroutine *Forces* will set the value of *Ic(I,J)* to 0.

Case 2. If r_{ij} is smaller than or equal to *rad(I)+rad(J)* and *Ic(I,J)* was equal to 0 in the last time step, it means that the two particles do come in contact during this time step. So the value of *tcby0* or *tczone( )* is increased by one, and *Ic(I,J)* is set to unity.

(a) If one of the particles is a boundary particle (at *y=0*), then

$$tcby0 = tcby0 + 1 \qquad (2\text{-}7\text{-}1)$$

(b) If neither of the particles is a boundary particle, then the location where the collision occurs must be determined in order to map it into the proper zone. The coordinates for particle *I* or its image in the primary cell are computed by,

$$\begin{cases} xp(I) = x(I) - xcell \cdot \mathrm{int}(\dfrac{x(I)}{xcell}) \\ yp(I) = y(I) - xcell \cdot \mathrm{int}(\dfrac{y(I)}{ycall}) \\ zp(I) = z(I) - zcell \cdot \mathrm{int}(\dfrac{z(I)}{zcell}) \end{cases} \tag{2-7-2}$$

Since in our studies, particles of uniform diameter are used (i.e., monodisperse), collisions will occurs at the middle point of the line joining the centers of two spheres as shown in Figure 2.12. Therefore, the y coordinate and the zone k where this collision occurs is given by,

$$y_m = \frac{yp(I) + yp(J)}{2} \tag{2-7-3}$$

$$k = 1 + \mathrm{int}(\frac{y_m}{yzone}) \tag{2-7-4}$$

In the event that particles "i" and "j" have collided in zone k; then the value of $tczone(k)$ is incremented by one, i.e.,

$$tczone(k) = tczone(k) + \tag{2-7-5}$$

Case 3. If $Ic(I,J)$ is equal to 1 and r_{ij} is smaller than $rad(I) + rad(J)$, then it means that the collision occurred in the previous time step and the two particles still are in contact at the current step. Since the collision has already been counted, it is not recounted and $Ic(I,J)$ is still set to unity.

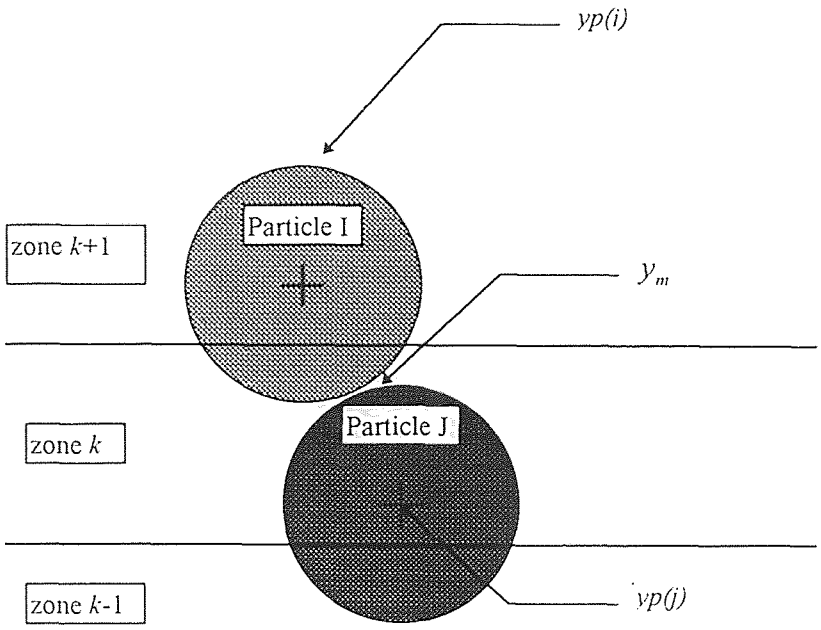

Figure 2.12 The Y Coordinate of Collision

The collision frequency

After the instantaneous collision numbers for each time step have been calculated in subroutine *Forces*, they are added to obtain the accumulated number of collisions :

$$\begin{cases} tcby0t = tcby0t + tcby0 \\ tczonet(Y) = tczonet(Y) + tczone(Y) \end{cases} \tag{2-7-6}$$

If time t is larger than the output time *tout*, then the total number of collisions will be divided by the output interval *dtout* to yield the collision frequencies,

$$\begin{cases} tcby0t = \dfrac{tcbyot}{dtout} \\ tczonet(Y) = \dfrac{tczonet(Y)}{dtout} \end{cases} \tag{2-7-7}$$

These collision frequencies are then written to the output files *tcy0* and *tczone*.

2.8 The Method of Computing the Mass Hold-Up

The mass hold-up is the dimensional mass supported by the vibrating floor. If the particles are spherical particles with uniform diameter d, then the formula for mass hold-up is

$$m_t = \int_0^{\frac{L}{d}} \nu(Y)\, dY = \frac{N \pi d^2}{6A} \tag{2-8-1}$$

where L is the depth of the bed, ν is the solid fraction depth profile, $Y = \frac{L-y}{d}$, N is the number of particles on the sieve, and A is the plane area of vibrating sieve.

The method of determining the position of the vibrating floor has been described in the Section (2.6.3) and is given by equations (2-6-1) and (2-6-2). The mass hold up *mashold* and the total mass of particles on the sieve *tmass* are calculated in subroutine *Datasav2*. These variables are initialized to zero. The location of every particle is examined at each time step to determine if it is still above the sieve floor. For each particle which has not passed through the mesh at time t, the instantaneous mass hold-up and the total mass are given by

$$\begin{cases} tmass = \sum_{y(i)>rad(i)} rmass(i) \\ mashold = \dfrac{\pi \cdot d^2}{6 \cdot xcell \cdot zcell} \sum_{y(i)>rad(i)} i \end{cases} \tag{2-8-2}$$

where *rmass(i)* is the mass of particle I, and $xcell \cdot zcell$ is the area of the vibrating floor. Once *tmass* and *mashold* have been determined, we also calculate the mass flow rate and the weight passing fraction, etc. Assuming that *tmass0 is* the initial value of *tmass* (at

t=0) , and *tmass1* is the value of *tmass* at the last output, then the mass flow rate *masflow* and the weight passing fraction p_w are computed as:

$$masflow = (tmass1 - tmass0) / dtout \tag{2-8-3}$$

$$p_w = (tmass0 - tmass) / tmass0 \tag{2-8-4}$$

All the values of these variables are written into the output file *Massflow* at each output time step *dtout*.

CHAPTER 3

RESULTS AND ANALYSIS

In this chapter, the behavior of both smooth and frictional particles under sieving will be discussed. The effects of the sieve aperture, the velocity intensity, and the vibration acceleration on the mass flow rate will be reported. Comparison's are also made with Richman and Wang's theoretical predictions [15].

In our studies, a system of acrylic spheres with density ρ = 1200 kg/m^3, diameter σ = 0.01 m is used. The friction coefficient μ of the friction spheres is set equal to 0.8, and the μ of the smooth particles is equal to 0.03. In order to reduce the computing time, the stiffness coefficient K which is used in our studies is equal to 1.55×10^5 thereby yielding a time step of 1.77×10^{-6} seconds.

With regard to the boundary motion (vibration), the definitions of the boundary velocities v_x, v_y, v_z, and the velocity amplitudes *vampx, vampy, vampz* had already been described in Section (2.6.4). Recall that $vampx = a_x \cdot omegax = a_1\omega_1$, $vampy = a_y \cdot omegay = a_2\omega_2$, $vampz = a_z \cdot omegaz = a_3\omega_3$ where a_1, a_2, a_3 are the amplitudes of vibration in the x, y, z directions, and ω , ω_2, ω_3, are the angular velocities in the three coordinate directions. Also, the motion of the sieve floor is given by :

$$v_x(t) = vampx \cdot cos(omegax \cdot t) = a_1\omega_1 \cdot cos(\omega_1 t)$$

$$v_y(t) = vampy \cdot cos(omegay \cdot t) = a_2\omega_2 \cdot cos(\omega_2 t) \qquad (3\text{-}0\text{-}1)$$

$$vz(t) = vampz \cdot cos(omegaz \cdot t) = a_3\omega_3 \cdot cos(\omega_3 t).$$

In what follows, we introduce the pertinent parameters defined in the kinetic theory (18), and also used in our case studies. First, the acceleration of vibration Γ is defined as :

$$\Gamma = a\omega^2 / g \qquad (3\text{-}0\text{-}2)$$

where a is the amplitude of vibration and ω is the frequency of the oscillating sieve floor. The velocity intensity of vibration α is defined as:

$$\alpha = \frac{V}{\sqrt{g\,\sigma}} \qquad (3\text{-}0\text{-}3)$$

$$V = \sqrt{\frac{1}{3}\left(v_1^2 + v_2^2 + v_3^2\right)} \qquad (3\text{-}0\text{-}4)$$

where v_1, v_2, and v_3 represent the average vibrating velocities in x, y, z directions, and V is the root mean square velocity of v_1, v_2, and v_3. The values of v_1, v_2, and v_3 are computed as:

$$\begin{cases} v_1^2 = \frac{1}{2} a_1^2 \cdot \omega_1^2 = \frac{1}{2} vampx^2 \\ v_2^2 = \frac{1}{2} a_2^2 \cdot \omega_2^2 = \frac{1}{2} vampy^2 \\ v_3^2 = \frac{1}{2} a_3^2 \cdot \omega_3^2 = \frac{1}{2} vampz^2 \end{cases} \qquad (3\text{-}0\text{-}5)$$

Here the 1/2 factor multiplying the terms on the right hand side of equation (3-0-4) is taken from the definitions in the kinetic theory [14]. The expresssion for V given in equation (3-0-3) is derived by calculating the root mean square velocity of the oscillating sieve floor as follows:

$$V^2 = \frac{1}{3}\left\langle \vec{V^2} \right\rangle = \frac{1}{3}\left(\frac{1}{\tau}\right)\int_0^{\tau}\left(v_x^2 + v_y^2 + v_z^2\right)dt \qquad (3\text{-}0\text{-}6)$$

where $\vec{2} = \vec{V} \cdot \vec{V} = v_x^2 + v_y^2 + v_z^2$, and $\langle\ \rangle$ denotes the mean. Recall that $v_x(t) = a_1\omega_1 \cdot cos(\omega_1 t)$, $v_y(t) = a_2\omega_2 \cdot cos(\omega_2 t)$, and $vz(t) = a_3\omega_3 \cdot cos(\omega_3 t)$. This leads to

$$V^2 = \frac{1}{3}\tau \int_o^\tau \left[a_1^2\omega_1^2 \cdot cos^2(\omega_1 t) + a_2^2\omega_2^2 \cdot cos^2(\omega_2 t) + a_3^2\omega_3^2 \cdot cos^2(\omega_3 t)\right]dt \qquad (3\text{-}0\text{-}7)$$

$$= \frac{1}{3}\tau \int_0^\tau \left[vampx^2 \cdot cos^2(\omega_1 t) + vampy^2 \cdot cos^2(\omega_2 t) + vampz^2 \cdot cos^2(\omega_3 t)\right]dt$$

Identity : $cos(\theta)^2 = \frac{1}{2}(1 + cos(2\theta))$. Then :

$$V^2 = \frac{1}{3}\tau \int_0^\tau \left[vampx^2 \cdot \frac{1}{2}(1 + cos(2\omega_1 t)) + vampy \cdot \frac{1}{2}(1 + cos(2\omega_2 t)) \right. \qquad (3\text{-}0\text{-}8)$$

$$\left. + vampz^2 \cdot \frac{1}{2}(1 + cos(2\omega_3 t))\right]dt$$

$$= \frac{1}{6\tau} vampx^2\tau + \frac{1}{6\tau} vampy^2\tau + \frac{1}{6\tau} vampz^2\tau$$

$$= \frac{1}{6}\left(vampx^2 + vampy^2 + vampz^2\right)$$

$$= \frac{1}{6}\left(2v_1^2 + 2v_2^2 + 2v_3^2\right)$$

$$= \frac{1}{3}\left(v_1^2 + v_2^2 + v_3^2\right)$$

In our studies, y is chosen opposite to the direction of the gravity field. The x. and, z directions then are the tangential directions. Consequently, the non-dimensional velocity intensities in normal and tangential directions are defined as:

$$\begin{cases} Vn = \dfrac{v_2}{V} \\ Vt = \dfrac{v_1}{V} = \dfrac{v_3}{V} \end{cases} \tag{3-0-9}$$

In this study, the values of v_1 and v_3 are the same. From Equations (3-0-3) and (3-0-5), a relationship between Vn and Vt is given by,

$$Vn^2 + 2 \cdot Vt^2 = \frac{v_1^2 + v_2^2 + v_3^2}{V^2} = 3 \tag{3-0-10}$$

The range of the vibration acceleration $\Gamma = a\omega^2 / g$ is from 2.84g to 56.5g in which the simulation results agreed with the kinetic theory predictions [10]. Therefore, the value of $\Gamma = a\omega^2 / g$ is chosen to be 30.0 in our study. If the values of α, Vn *and* Vt are chosen, the values of all the other parameters can be calculated by using the above equations. Now, For example, from Equation (3-0-2), if $\alpha = 1$, then the root mean velocity V becomes $V = \alpha\sqrt{g\sigma} = \sqrt{g\sigma}$. Now, ω , ω_2 and ω_3 can be found. From equation (3-0-5), if $Vn^2 = 3$, then $v_1 = v_3 = 0$, and $v_2 = \sqrt{3}V$. From the kinetic theory [14], $v_2^2 = \frac{1}{2} a_2^2 \omega_2^2$.. Therefore, $v_2 = \sqrt{3}V = \frac{a_2\omega_2}{\sqrt{2}}$, and $V = \frac{a_2\omega_2}{\sqrt{6}}$ As previously mentioned, $\Gamma = a_2\omega_2^2 / g = \frac{\sqrt{6}V\omega_2}{g} = 30$. Therefore, the frequency of vibration $\omega_2 = \frac{30g}{\sqrt{6}V} = \frac{30g}{\sqrt{6g\sigma}} = 30\sqrt{\frac{g}{6\sigma}}$. Once the value of ω_2 is determined, then the amplitude of vibration a_2 can be computed since $v_2 = \frac{a_2\omega_2}{\sqrt{2}}$. Table 3.2 contains all the

input values of *vampx, vampy, vampz, frqx, frqy, frqz* for the values α, Vn and Vt used in these studies.

Table 3.1 The Values of the Amplitude of Velocity and the Frequency

α	Vn^2	Vt^2	*vampx*	*vampy*	*vampz*	*frqx*	*frqy*	*frqz*
0.25	0	3	0.136	0	0.136	345.2	0	345.2
0.25	1	1	0.11	0.11	0.11	422.8	422.8	422.8
0.25	2	0.5	0.078	0.157	0.078	597.9	298.9	597.9
0.25	3	0	0	0.192	0	0	244.1	0
0.5	0	3	0.271	0	0.271	172.6	0	172.6
0.5	1	1	0.221	0.221	0.221	211.4	211.4	211.4
0.5	2	0.5	0.157	0.313	0.157	298.9	149.5	298.9
0.5	3	0	0	0.383	0	0	122	0
1	0	3	0.542	0	0.542	86.3	0	86.3
1	1	1	0.443	0.443	0.443	105.7	105.7	105.7
1	2	0.5	0.313	0.626	0.313	149.5	74.75	149.5
1	3	0	0		0	0	61	0

3.1 Smooth Particles and the Smallest Friction Coefficient

Several tests were performed to determine how smooth the particles could be so they would not fall through the mesh unassisted by the oscillations of the floor. In the first test, a group of smooth spheres with zero friction coefficient was used. The diameter of the identical flow spheres and the diameter of sieve aperture S_2 are both equal to 0.01 *m*. These particles are placed on a stationary sieve floor. From the results of this test, it was found that the spheres fell through the sieve mesh very quickly.

In the second test, the size of sieve openings was slightly reduced and the system was vibrated. From the output, a few particles were still found to pass through the mesh

openings even though the sphere diameter was somewhat larger than the diameter of the sieve apertures.

The results of the two tests indicated that the smooth particles with zero friction coefficient could not be used in the simulations. Without a friction force, the weight of the particles can not be supported. Consequently, particles can pass through the mesh with little or no vibration of the floor. Even though the diameter of particles are a little larger than the sieve aperture, the total weight of the particles will still push the bottom particles to pass through the mesh. Therefore, the use of smooth particles (μ=0) was abandoned.

In order to determine the minimum friction coefficient to prevent spheres from passing through the mesh unassisted by vibration, the last two tests for several different values of μ. were repeated. The results indicated that the smallest friction coefficient which could be used is equal to 0.03. By using this value, the particles will not fall through the mesh without shaking.

3.2 The Solid Fraction and Granular Temperature Depth Profiles

In this section, the temperature and the packing fraction depth profiles are reported. and also qualitatively compared with the kinetic theoretical predictions [14]. The granular temperature is the kinetic energy of the particles' fluctuating velocities, The higher the temperature, the faster are the particles' velocity fluctuations. During shaking, the work done by the external forces is transformed into kinetics energy, and the granular temperature of the particles increases. The depth profile od the long term mass-weighted average granular temperature T(Y) (at depth Y) is computed as:

$$T(Y) = \frac{1}{3}(< C(Y,t) >_L)^2 = \frac{1}{3}\frac{\sum_{t=t_0}^{t_{max}} (\sum_{i \in Y} \hat{m}_i(t).(v_i(t) - u(Y,t))^2)}{\sum_{t=t_0}^{t_{max}} (\sum_{i \in Y} \hat{m}_i(t))} \qquad (3\text{-}2\text{-}1)$$

where $<C(Y,t)>_L$ is the long term mass-weight average of the rms deviatoric velocity, $v_i(t)$ is the velocity of particle i, $\hat{m}_i(t)$ is the mass fraction of particle i in layer Y, $u(Y,t)$ is the instantaneous mean velocity in layer Y. The value of $u(Y,t)$ is calculated by :

$$u(Y,t) = \frac{\sum_{i \in Y} \hat{m}_i(t) \cdot v_{i(t)}}{\sum_{i \in Y} \hat{m}_i(t)} \qquad (3\text{-}2\text{-}2)$$

The dimensionless granular temperature is then defined as:

$$W(Y) = \sqrt{\frac{T(Y)}{\sigma g}} \qquad (3\text{-}2\text{-}3)$$

For the comparison with the theory, a plane boundary is used as the vibrating floor. The parameters used are listed in Table 3.2.

Table 3.2 List of Parameters (Case 1)

Parameter	Value
Diameter Of Flow Particles σ	0.01 m
Density ρ	1200 kg/m^3
Mass hold-up m_t	10
Restitution Coefficient e	0.9

Table 3.2 List of Parameters (Case 1) - continued

Normal Stiffness Coefficient K_1	1.55×10^5
Friction Coefficient μ	0.8
Velocity Intensity α	1
Vn^2	3

Temperatures and solid fraction profiles are presented in Figure 3.1 and Figure 3.2. These two figures are qualitatively in good agreement with the kinetic theoretical predictions [14]. In Figure 3.1, the granular temperature is highest at the vibrating floor, and decreases upwards along the depth In Figure 3.2, the highest solid fraction appears at somewhat the middle of the depth.

3.3 The Mass Flow Rate

3.3.1 The Effect of the Sieve Aperture

In this set of case studies, the effect of the sieve aperture on the mass flow rate will be discussed. For the purpose, three values of the diameter of sieve apertures S_2 are used. The first value of S_2 is equal to 0.0104 m = 1.04 σ, the second one is equal to 0.0108 m = 1.08 σ, and the third one is equal to 0.0112 m = 1.12σ. All the values of the parameters in this set of simulations are listed in Table 3.3. The corresponding velocity amplitudes and frequencies are listed in Table 3.1.

Table 3.3 List of Parameters (Case 2)

Parameter	Value
Diameter Of Flow Particles σ	0.01 m
Density ρ	1200 kg/m^3
Mass hold-up m_t	20
Restitution Coefficient e	0.9
Stiffness Coefficient K_1	1.55×10^5
Friction Coefficient μ	0.03, 0.8
Diameter Of Sieve Aperture S_2	0.0104 m, 0.0108 m, 0.0112 m
Velocity Intensity α	1

Smooth Particles

For the smooth particles (μ=0.03), the comparisons of the Mass hold-up versus time plots for the three values of S_2 are presented in Figure A3.3(a-d). In each figure, the values of Vn , Vt, are kept the same while we change the value of S_2. These figures clearly show the influence of the size of the sieve aperture. The general trend is that the smaller the S_2, the slower the mass hold-up decreased, and the smaller the mass flow rate. We also note that when Vn^2 is equal to 1, where the vibrations in all three directions are the same, the Mass hold-up evolution is nearly equal for all values of S_2 except near the end of sieving process. This means that the influence of the sieve aperture is very small

when Vn^2 is equal to unity. In the other cases, the differences among the three curves are very clear.

Frictioned Particles

For the frictioned particles in which μ is equal to 0.8, the comparisons of the Mass hold-up evolution with different α values are presented in Figure 3.4 (a-d). From these figures, nearly the same influence of the sieve aperture can be observed as was seen in the figures for smooth particles. The smaller the S_2 the slower the mass hold-up is decreased, and the smaller the mass flow rate.

If you draw a horizontal line at m_t = 10 in Figure A3.4(d) and compare the time needed for the Mass hold-up decreaing form 20 to 10 for each different S_2, you will find out that the time needed for S_2 = 0.0104 m is much longer than the time need for S_2 = 0.0108 m. Therefore, the mass flow rate for S_2 = 0.0104 m = 1.04 σ is much slower than the mass flow rate for S_2 = 0.0108 m =1.08 σ. This in turn is slower than the massflow rate for S_2 = 0.0112 m = 1.12 σ. This result is in good agreement with Markwick's investigations [12]. His experiments results shown that the particles were easy to pass through the sieve if the sizes of the particles are smaller then 90% of the seive aperture. From 90% to 95%, the particles will have some difficuties in passing through the sieve. If the size of the particles is larger than 95% of the sieve aperture, it will be very difficult for the particles to pass through the sieve.

In Figure A3.4(e-h), comparisons of the evolution curves for the smooth and rough particles reveal that the smooth particles flow much faster than the rough particles. The Mass hold-up time profiles for the rough particles are nearly straight lines except at

the end of sieving process. This implies that the sieving rate is nearly a constant in the whole process. These are the major differences of the sieving rate between the smooth and rough particles.

3.3.2 The Effect of the Vibration Energy

In this section, the influence of the vibration energy on the mass flow rate is studied. For the purpose, three different values of α are used : 0.25, 0.5, 1. The values of parameters in this set of case studies are listed in Table 3.4, and the corresponding velocity amplitudes and frequencies of vibration can be found in Table 3.1.

Table 3.4 List of Parameters (Case 3)

Parameter	Value
Diameter Of Flow Particles σ	0.01 m
Density ρ	1200 kg/m^3
Mass Hold Up m_t	20
Restitution Coefficient e	0.9
Stiffness Coefficient K_1	1.55×10^5
Friction Coefficient μ	0.03, 0.8
Diameter Of Sieve Aperture S_2	0.0108 m
Velocity Intensity α	0.25, 0.5, 1

Smooth Particles

For the smooth particles (μ = 0.03), the comparison of the Mass hold-up evolution with different α values is presented in Figure A3.5(a-d). In each figure, the values of Vn and Vt, are fixed while the value of α is varied. In Figure A3.5(a) where Vn^2 is equal to 0, the Mass hold-up evolution is nearly equal for all values of S_2 except near the end of sieving process. , This implies that the influence of the velocity intensity α is very small. In the other figures, most of the results of simulations clearly show that the smaller α is, the faster the mass hold-up decreases (except the evolution of the Mass hold-up for α = 0.25 in Figure A3.5(c)). This phenomena is contradicts Richman and Wang's theoretical predictions [10]. This is probably because of the friction coefficient is too small, so that the force bonds between particles is very weak. Therefore, small vibration energy can totally brakes these forces bonds, and enhance flow while excessive energy (large α) will further increases the random motions of particles thereby inhibiting sieving action. In this case, the larger the energy of vibrations, the smaller the mass flow rate.

Frictioned Particles

For the particles with the friction coefficient μ = 0.8, comparisons of the Mass hold-up evolution with different values of α are presented in Figure A3.6(a-d). As shown in Figure 3.6(a)(b), When Vn^2 is equal to 0 and 1, the influence of the velocity intensity α is very small. The Mass hold-up evolution is nearly equal for all values of S_2 except near the end of sieving process. In Figures 3.6(c)(d) where Vn^2 is equal to 2 and 3 , it can clearly be seen that the flow rate for α = 0.5 is now larger than the rate of α = 0.25, but the flow rate of α = 1 is still much slower than the other two. This is probably because of the

friction coefficient is increased. The friction force bonds between particles are now much stronger. Therefore, the energy of vibration is not sufficient to totally break these bonds when α is equal to 0.25, or 0.5. In this case, the vibration energy is helpful for the particles to sift through the sieve. However, when α is equal to 1, the energy of vibration is sixteen times of the energy of vibration when α is equal to 0.25. The energy probably is excessive, and this hinders the particles from falling through the sieve. Therefore, the mass flow rate of $\alpha = 1$ is much slower than the mass flow rate of $\alpha = 0.25$ and $\alpha = 0.5$.

3.4.3 The Effect of the Boundary Motion

In this section, the focus is on the influence of the boundary motion of the mass hold-up evolution. As described in Equation (3-0-5), Vn and Vt are defined as the dimensionless velocities in the normal and tangential directions. Therefore, changing the value of Vn and Vt means changing the motion of the vibrating boundary. Recall from Equation (3-0-6) that Vn and Vt have a $Vn^2 + Vt^2 = 3$. Therefore, the total energy of vibration will not be altered Vn and Vt are adjusted. The values of the parameters that were used in this set of studies are listed in Table 3.5. For each specified values of α and S_2, four different cases were run, i.e., $Vn^2 = 0, 1, 2, 3$.

Table 3.5 List of Parameters (Case 4)

Parameter	Value
Diameter Of Flow Particles σ	0.01 m
Density ρ	1200 kg/m^3

Table 3.5 List of Parameters (Case 4) - continued

Mass Hold Up m_t	20
Restitution Coefficient e	0.9
Stiffness Coefficient K_1	1.55×10^5
Friction Coefficient μ	0.03, 0.8
Diameter Of Sieve Aperture S_2	0.0104 m, 0.0108 m, 0.0112 m
Velocity Intensity α	0.25,0.5, 1

Smooth Particles

For the smooth particles, the comparison of the Mass hold-up evolution for different Vn are presented in Figure A3.7 (a-e). In Figure A3.7(a-c), the velocity intensity α is equal to one. These figures clearly indicate that the larger the Vn, the slower is the decrease of Mass hold-up. As explained in previous sections, when the energy of vibration exceeds the energy which is needed to break all the force bonds between particles, the excessive energy will hinder the particles from falling through the sieve. In this case, increasing the value of Vn further decreasing the mass flow rate. Therefore, we further hypothesize that it is the energy in normal directions that more strongly affects the mass flow rate of sieving.

In Figure A3.7(d), the velocity intensity α is equal to 0.5. The mass flow rate of Vn^2 =3 is generally larger than the mass flow rate of Vn^2 =2, and this in turn is larger than of Vn^2 =1 and Vn^2 =0. These results implies that the vibration energy when $\alpha = 0.5$ is

smaller than the energy needed to break the force bonds between particles. There the larger the normal vibration energy, the faster is the decrease of Mass hold-up. Again, this is further suggests that the vibration energy in normal direction more strongly affects the mass flow rate of sieving.

In Figure A3.7(e) where α=0.25, nearly the same results with α=0.5 can be observed except that the mass flow rate of Vn^2 =2 becomes smaller than the mass flow rate of Vn^2 =0.

Frictioned Particles

For the frictioned particles, the comparison of the Mass hold-up evolution for different Vn is presented in Figure A3.8(a-e). As previously suggested, the frictional force bonds between particles becomes stronger as the friction coefficient increases. Therefore, the energy which is required to overcome the force bonds and dislodge the assembly is larger. For the convenience in description, we call this energy which is required to break the force bonds between particles the *limit energy*.

The velocity intensity α is equal to one in Figure A3.8(a)(b)(c). These three figures seem to indicate that the limit energy is also affected by the size of the sieve apertures. In Figure A3.8(a)(b), the diameters of the sieve aperture are equal to 0.0104 m and 0.0108 m. There, the mass flow rate for Vn^2 =1 is larger then the mass flow rate when Vn^2 =0, and the mass flow rate of Vn^2 =2 and Vn^2 =3 are much smaller then the mass flow rate of Vn^2 =0. This implies that the *limit energy* is greater than the energy of vibration in the normal direction when Vn^2 =1. However, when the diameter of sieve aperture is equal to 0.0112 m, the comparison profiles suggest that the limit energy is

smaller then the energy of vibration in the normal direction when $Vn^2 = 1$. Since the total energy of vibration did not change, it is clear that the limit energy for S_2=0.0112 m is smaller then the limit energy for S_2=0.0104 m and S_2=0.0108 m. Therefore, the smaller the sieve aperture, the larger the limit energy.

3.4 Comparisons with Kinetic Theory Predictions

In this section, comparison will be made with the kinetic theory prediction of Richman and Wang [15]. In this theory, a time scale is used for measuring the time of sieving. This dimensionless time scale t^* is defined as :

$$t^* = \left[1 - \frac{(1+r)^2}{(1+\Delta)^2}\right] \cdot \bar{t} \qquad (3\text{-}4\text{-}1)$$

$$\bar{t} = t\sqrt{\frac{g}{\sigma}} \qquad (3\text{-}4\text{-}2)$$

Here, $r = \frac{\sigma}{d}$, $\Delta = \frac{s}{d}$, σ is the diameter of the flow particle, s is the mean sieve aperture, and d is the diameter of the boundary particles, $\bar{t}$ is the dimensionless time of sieving, and t is the real sieving time.

The values of the parameters which are used in this set of studies are listed in Table 3.6. In the studies, the diameter of the flow particles σ is equal to 0.01 m. For a chosen value of S_2, the diameter of the boundary particles is calculated as : $d = 0.01 \cdot \sqrt{2} - S_2$. Since it is not known how the mean sieve aperture s is relates to the simulation sieve mesh, the value of the diameter of sieve apertures S_2 is chosen to represent the mean sieve aperture s. Therefore, once the value of S_2 is determined, it is possible calculate the ratio t^* and t

from the simulation results. The values of the diameter of sieve aperture S_2 and the corresponding ratios t^*/t are listed in Table 3.7.

Table 3.6 List of Parameters (Case 5)

Parameter	Value
Diameter Of Flow Particles σ	0.01 m
Density ρ	1200 kg/m^3
Mass Hold Up m_t	20
Restitution Coefficient e	0.9
Stiffness Coefficient K_1	1.55×10^5
Friction Coefficient μ	0.8
Velocity Intensity α	0.25,0.5,1
Diameter Of Sieve Aperture S_2	0.0104 m, 0.0108 m, 0.0112 m
Vn^2	3

Table 3.7 The Diameter of the Sieve Aperture and the Corresponding Time Ratio

Diameter of Sieve aperture S_2	t^*/t
0.0104 m	1.734
0.0108 m	3.442
0.0112 m	5.09

Comparisons of the mass hold-up evolution curves with theoretical predictions are presented in Figure A3.9(a-d) to Figure A3.13(a-d). It is evident that the plots from the simulations do not compare well with those from the theoretical predictions. This is probably because the definition of the mean space is not correct. It can be seen from Equation (3-4-1) and Equation (3-4-2) that the ratio t^*/t is very sensitive to Δ for a fixed r. Hence comparisons with the theory using this spacing requires a better identification between s and the mesh geometry.

CHAPTER 4

SUMMARY AND CONCLUSION

4.1 Summary of Progress

The original shear code transferred from Walton was modified to fit for the sieving simulation. The bumpy boundary is changed to simulate the sieve mesh, and the vibration of the boundary is changed from one dimension to three dimensions. Two tasks are required to accomplish a case study. In the first task, the flow particles are poured into our computational cell, and stay steadily on the sieve for a period of time. An initial configuration of the positions of the particles is generated. In the second task, these particles are vibrated by the sieve floor. The Mass hold-up, the temperature, the packing fraction, and the other diagnostic parameters are then calculated and saved into the output files.

Periodic boundaries are used as the side walls of the computational cell. Therefore, we can model the process of sieving in a volume without the wall influence and reduce the number of particles in the system. In the studies, about 600 identical acrylic spheres were put into cell.

Two types of particles are used in the studies. One is the smooth particle having friction coefficient equal to 0.03. The other is frictioned particle with friction coefficient is equal to 0.8. The densities of the two types of particles are both equal to 1200 kg/m^3. Three different diameters of the sieve apertures S_2 are used. The first one is equal to 0.0104 m, the second one is equal to 0.0108 m, and the last one is 0.0112 m. The velocity

intensity α is also varied, i.e., α = 0.25, 0.5, and 1. For each different α and S_2, four different cases were run with Vn^2 = 0, 1, 2, 3. The effects of the sieve aperture, the energy of vibration, and the motion of the boundary are then studied. Lastly, the results are compared with Richman and Wang's theoretical predictions [15].

4.2 Conclusion

During sieving, the mass flow rate of the particles is positively affected by the size of the sieve apertures. In our studies, the mass flow rate for sieve aperture S_2 =0.0112 *m* is larger than the mass flow rate when S_2 =0.0112 *m*. This in turn is larger than the flow rate when S_2 =0.0104 *m*. As expected, the greater the size of sieve apertures, the faster the particles fall through the sieve.

With regard to the energy of vibration, it is found that the mass flow rate is dominantly affected by the vibration energy in the normal direction. At the same time, an *limit energy* which is equal to the energy needed to totally break the force bonds between particles was observed from the results of our case studies. If the vibration energy in the normal direction is smaller than this *limit energy*, the energy of vibration has a positive influence to the mass flow rate of sieving. The greater the energy, the faster the particles fall through the sieve. However, if the vibration energy in the normal direction exceeds the *limit energy*, then the influence of the vibration becomes negative, i.e., The larger the energy of vibration, the slower the mass flow rate. By searching all the related literature, a statement from F. G. Carpenter's experimental report [5] was uncovered that may gives a support to the conclusion of the simulation. In his experiments, under-sized particles

which were retained on the sieve at the speed of approximately 150 taps/min. may be pass though the mesh at the speed of approximately 115 taps/min. It means that a large vibration energy may be will prevent the particles falling through the sieve.

From the results, it was also found that the *limit energy* is related to the friction forces between particles and the size of the sieve apertures. The larger the friction coefficient, the larger the *limit energy*, and the greater the sieve aperture, the smaller the *limit energy*.

4.3 Future Work

There are still many interesting topics in this field that need to be studied. With regard to the simulations, three main concerns are required to proceed:

1. The mean spacing of our sieve aperture needs to be defined. The sieve mesh should be modeled more realistically. The boundary particles in the code can be changed from a semi-sphere to cylinder wires. In this way, the computational mesh will appears like a real sieve.

2. A mathematical model of the energy limit should be established. For this purpose, a large number of case studies should be carried out and the influences of the sieve aperture and the friction coefficient should be studied quantitatively.

3. The studies should be repeated by using different values of Γ. As previously described, the value of Γ is important in determining whether the behaviors of particles will satisfy the kinetic theory prediction. Before this study, no large initial mass hold-up

was used in any experiment or simulation. Therefore, it is necessary to determine the range of Γ which can satisfy the kinetic theory for $m_t = 20$.

APPENDIX

FIGURES OF CHAPTER 3

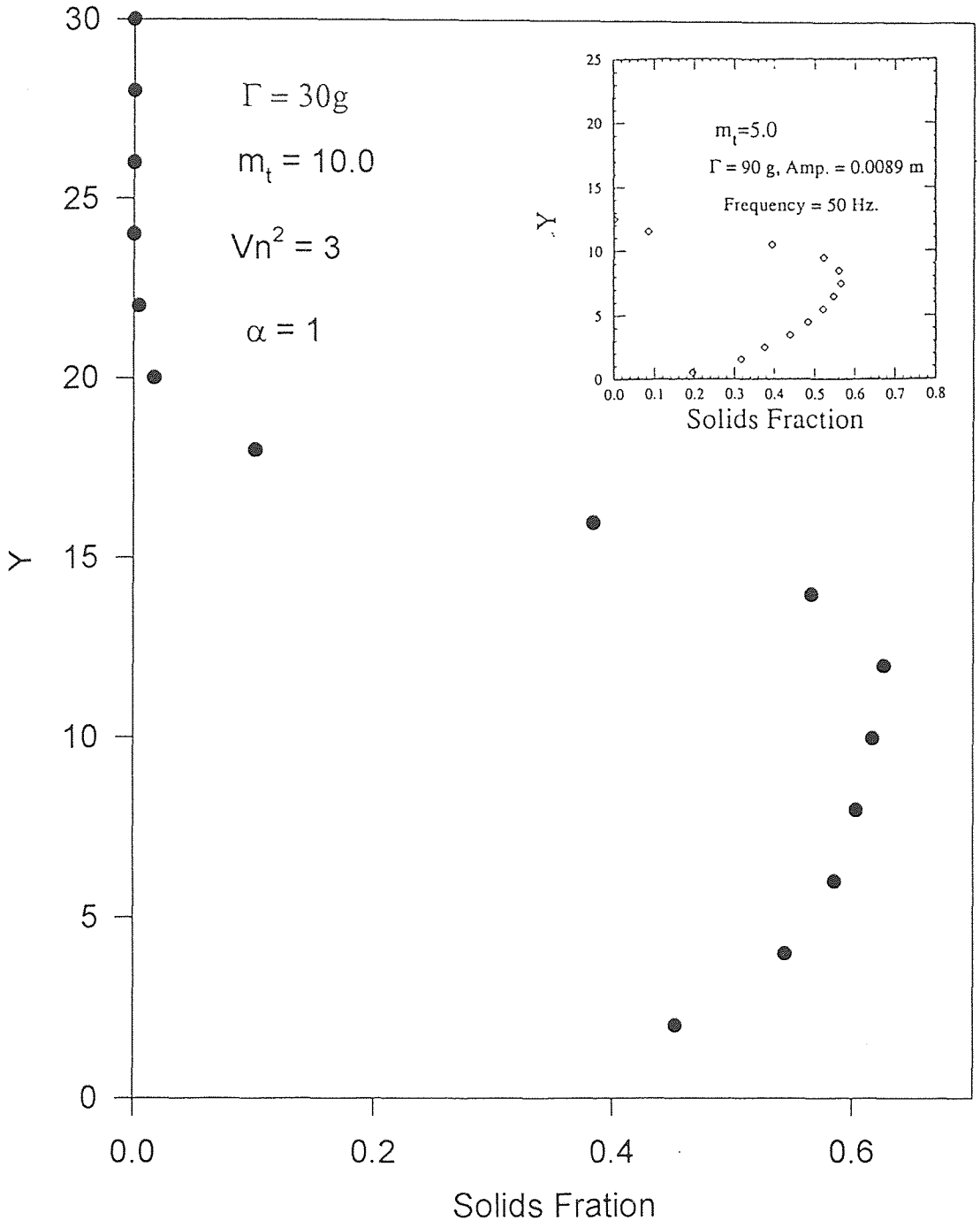

Figure A3.1 Solids fraction depth profile

Insert is the solid fraction depth profile from the simulation of Lan (15)

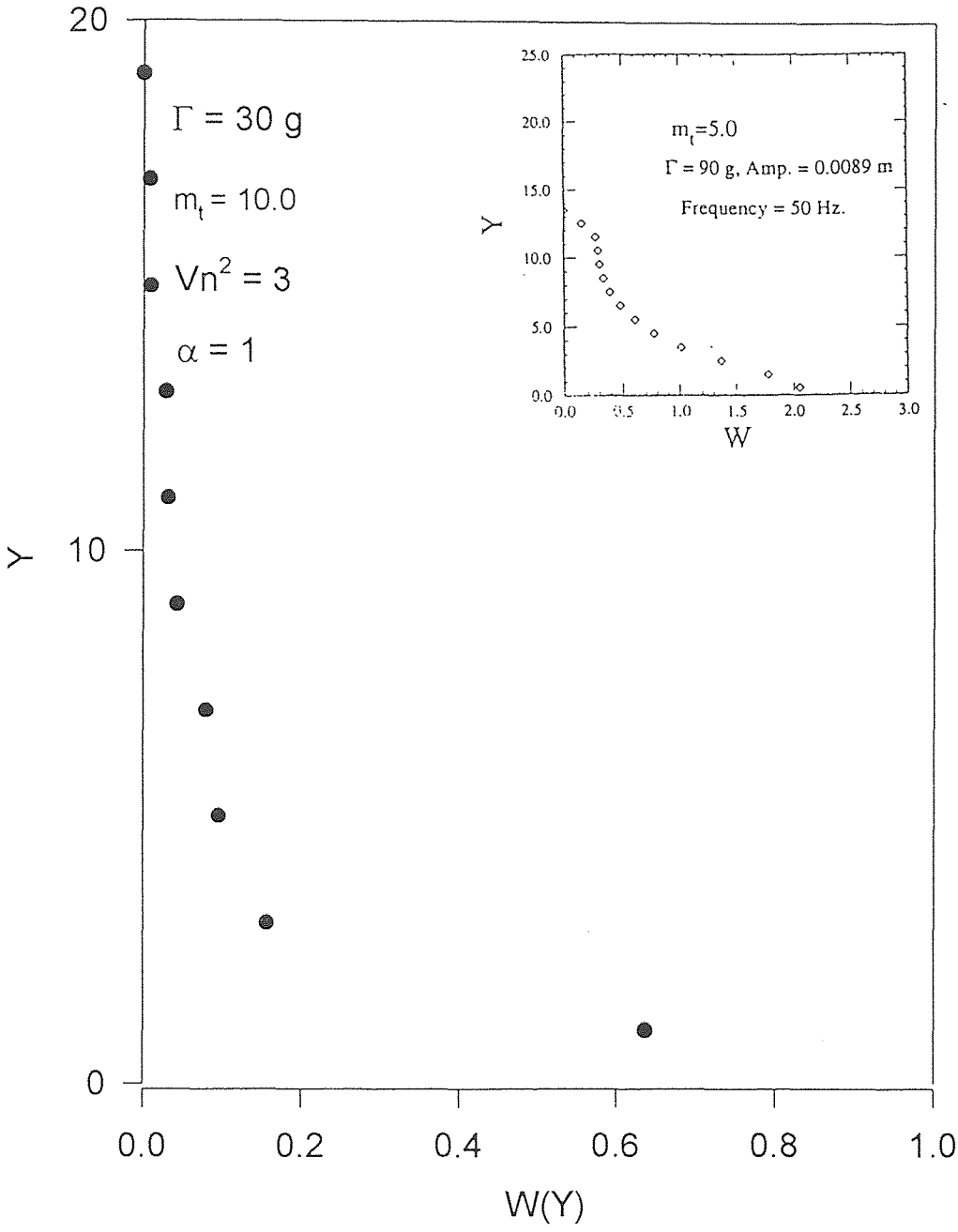

Figure A3.2 Dimensionless granular temperature depth profile
Insert is the Temperature depth profile from the simulations of Lan (15)

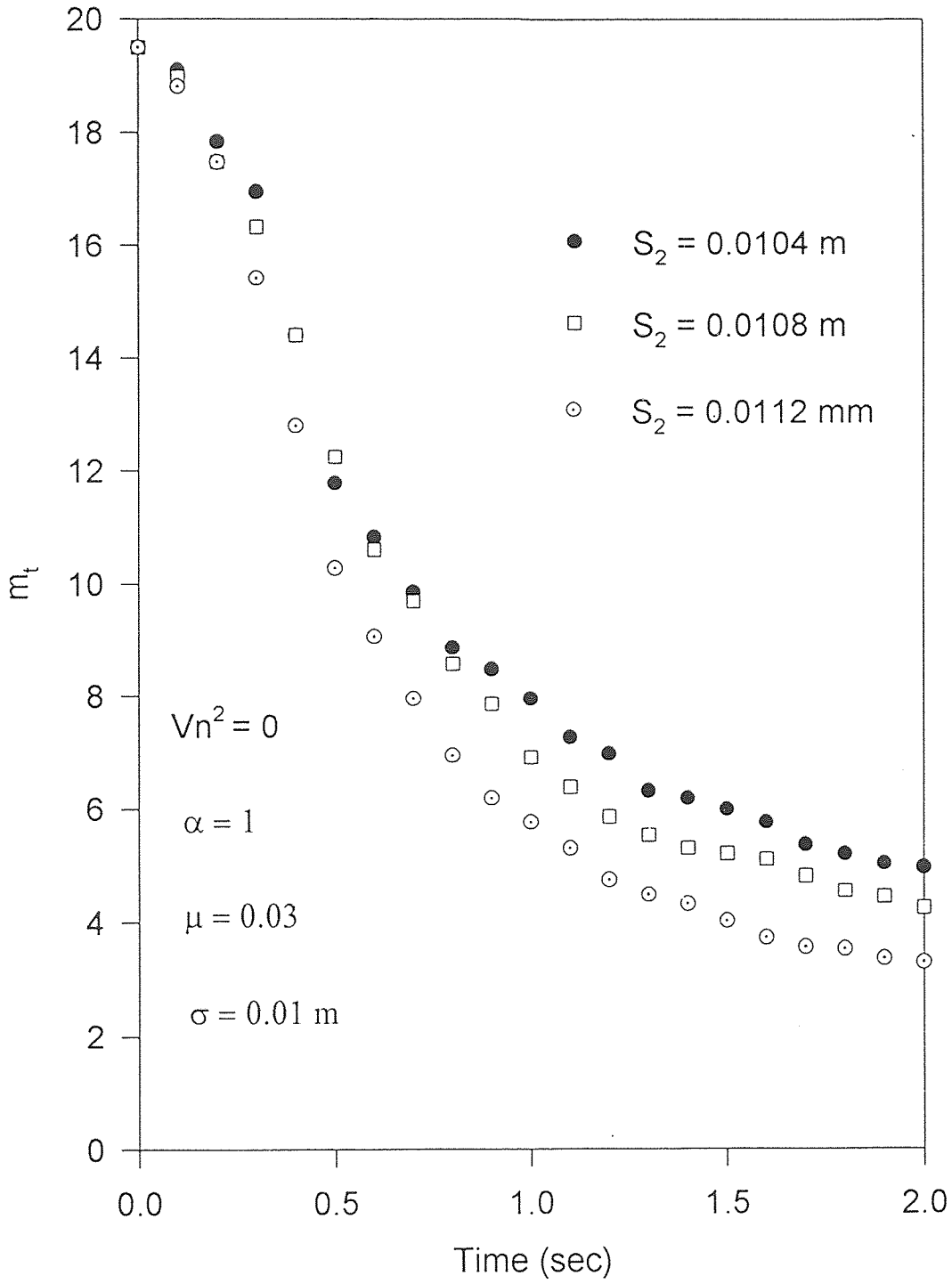

Figure A3.3(a) Mass hold-up evolution for different sieve apertures. Vn^2=0, α=1, μ=0.03, σ=0.01 m

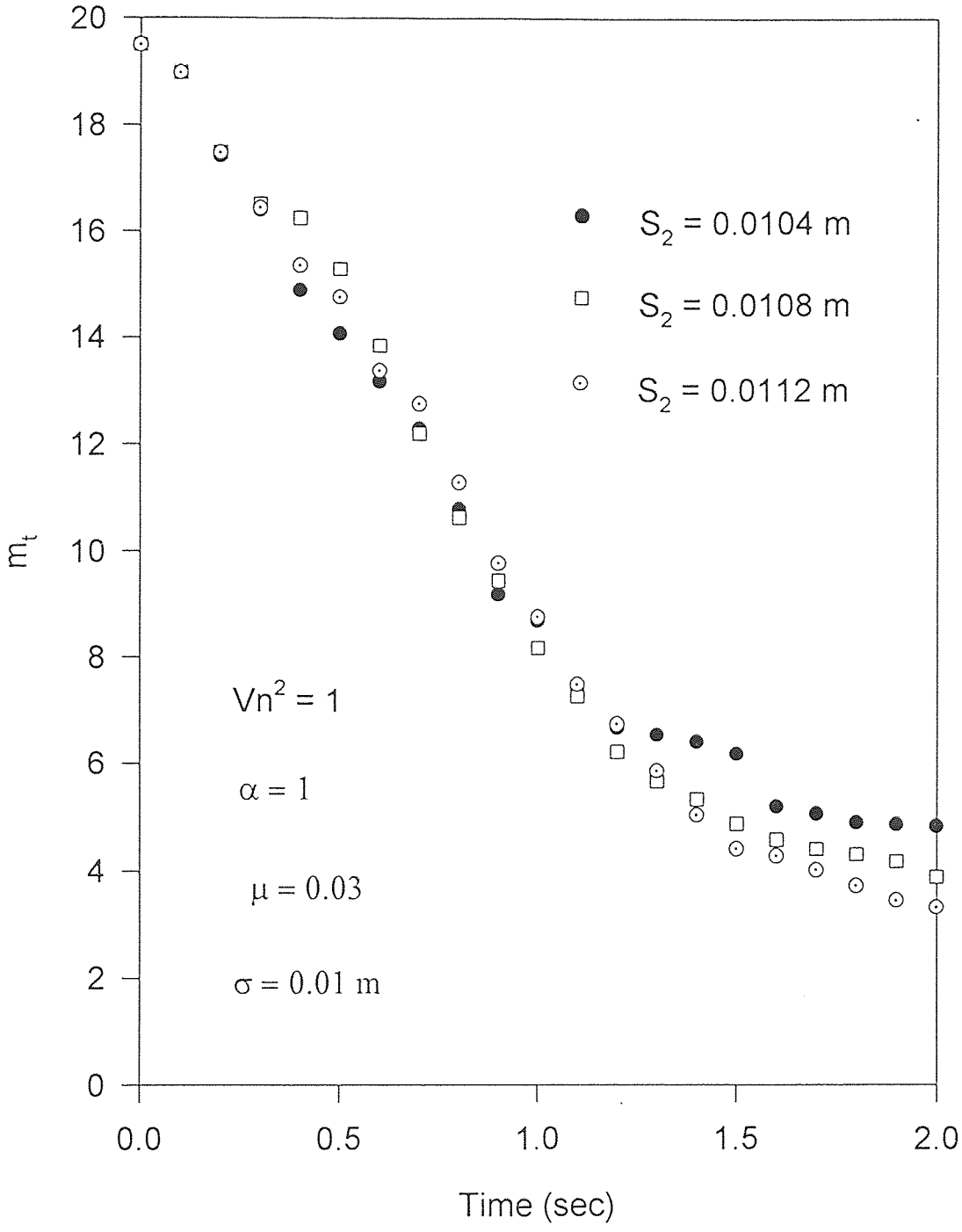

Figure A3.3(b) Mass hold-up evolution for different sieve apertures.
Vn^2=1, α=1, μ=0.03, σ=0.01 m

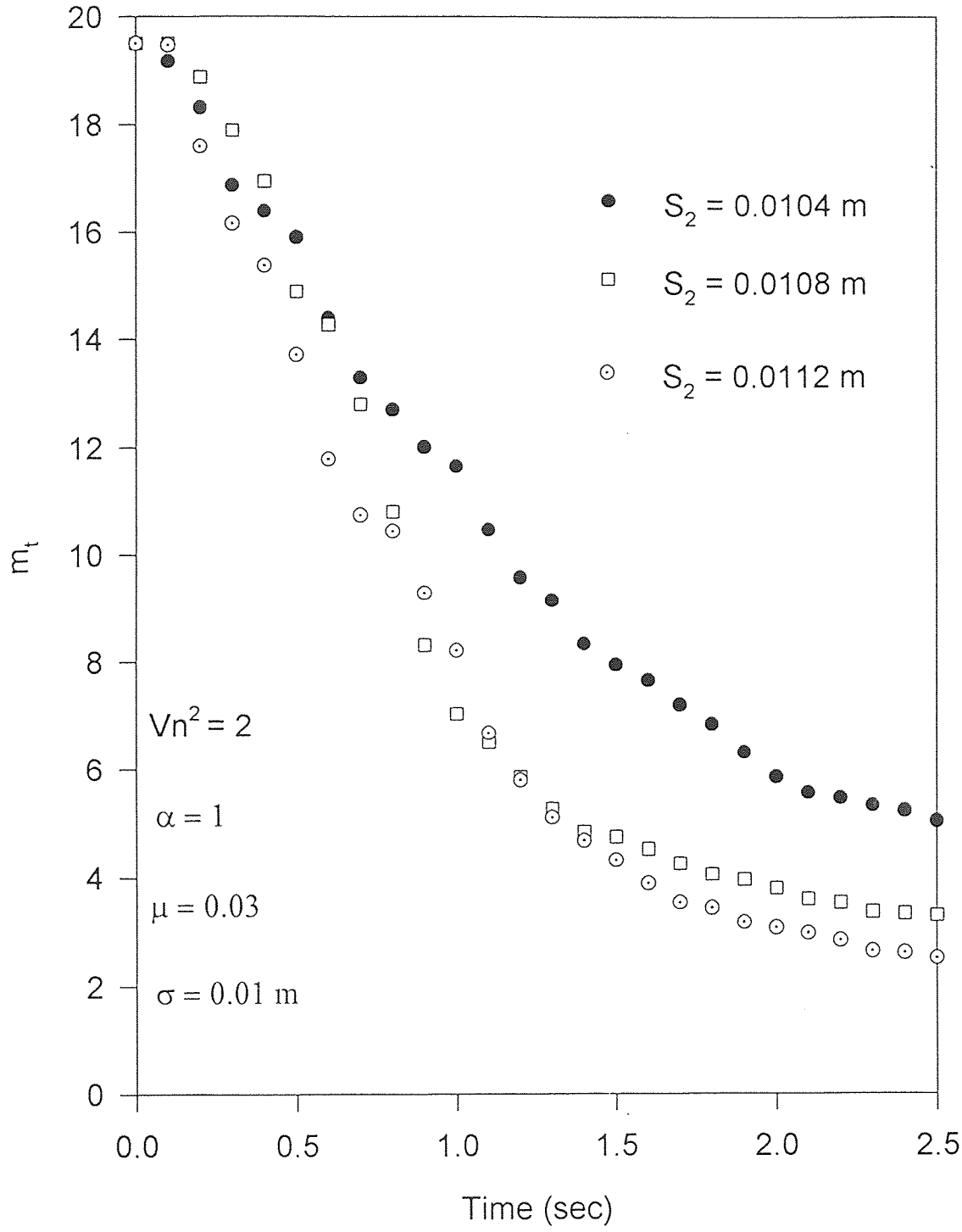

Figure A3.3(c) Mass hold-up evolution for different sieve apertures. Vn^2=2, α=1, μ=0.03, σ=0.01 m

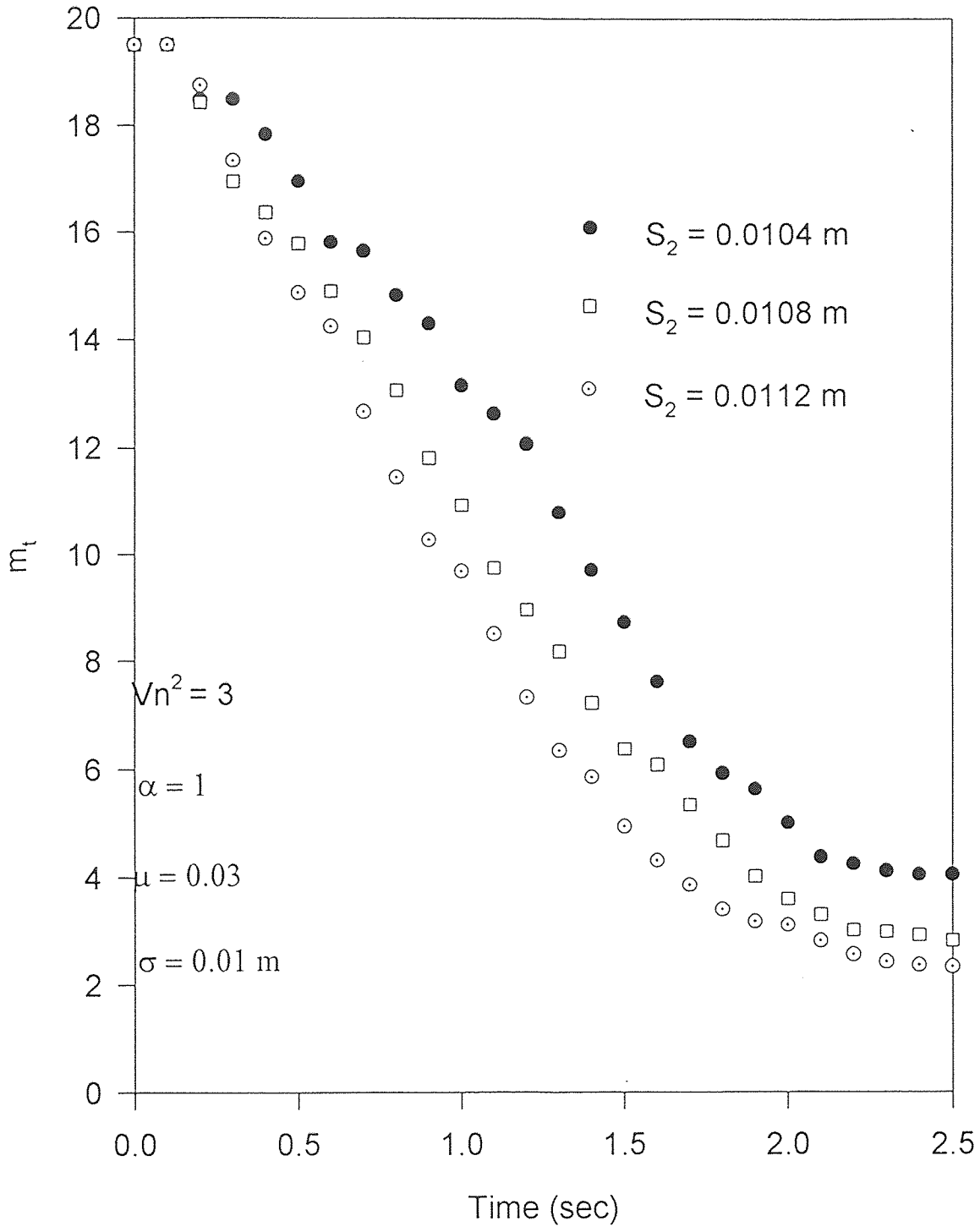

Figure A3.3(d) Mass hold-up evolution for different sieve apertures.

Vn^2=3, α=1, μ=0.03, σ=0.01m

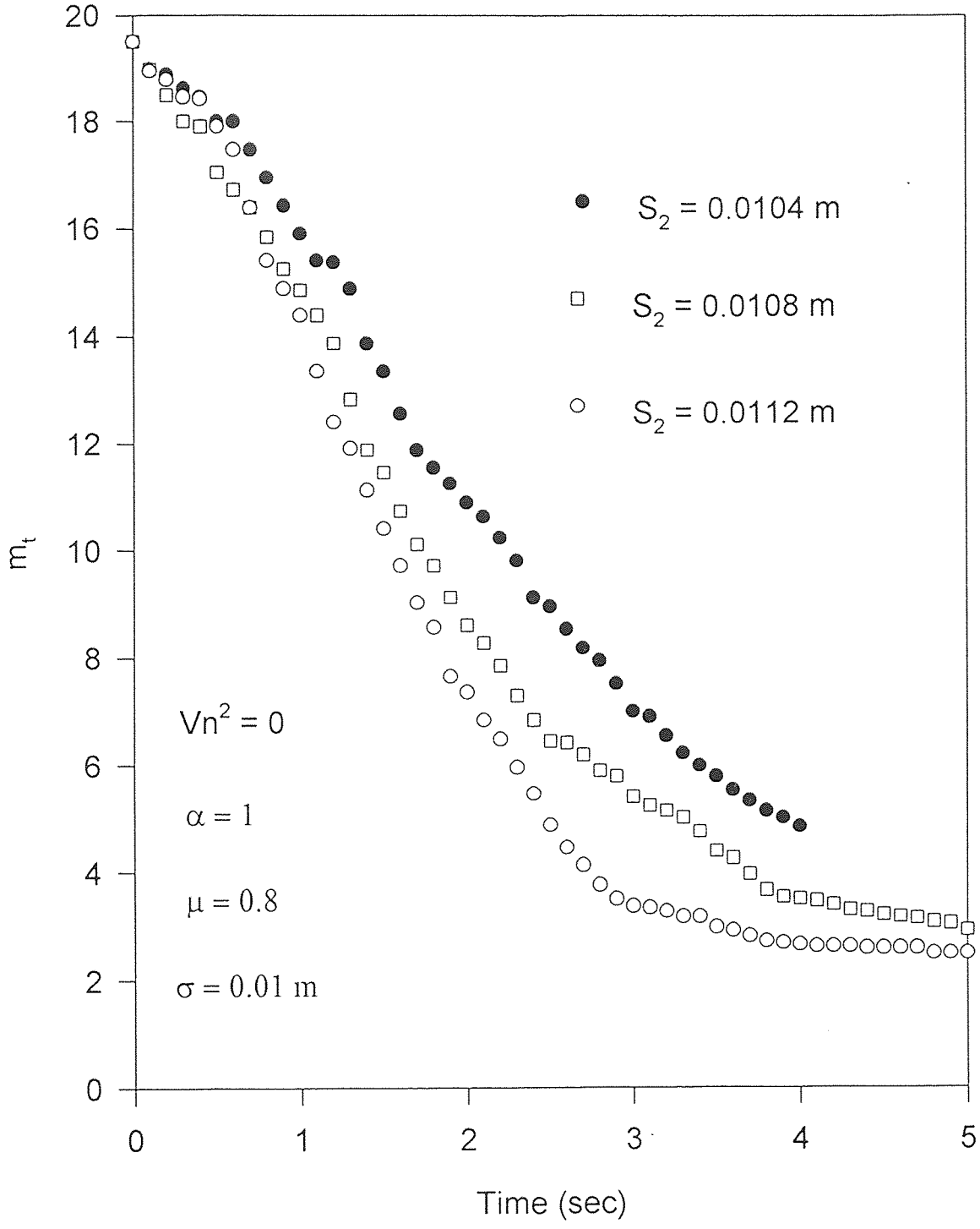

Figure A3.4(a) Mass hold-up evolution for different sieve apertures

Vn^2=0, α=1, μ=0.8, σ=0.01 m

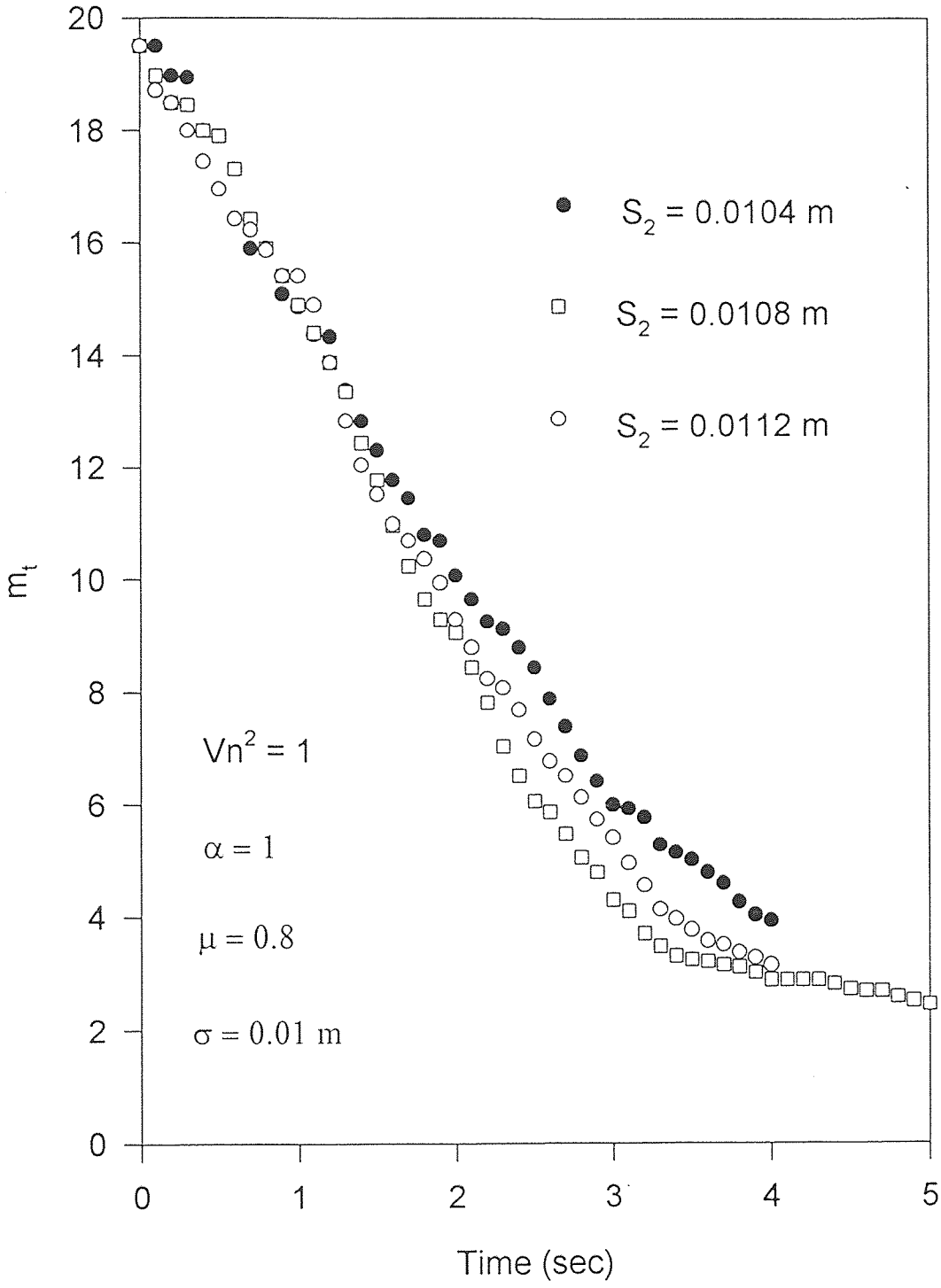

Figure A3.4(b) Mass hold-up evolution for different sieve apertures

Vn^2=1, α=1, μ=0.8, σ=0.01 m

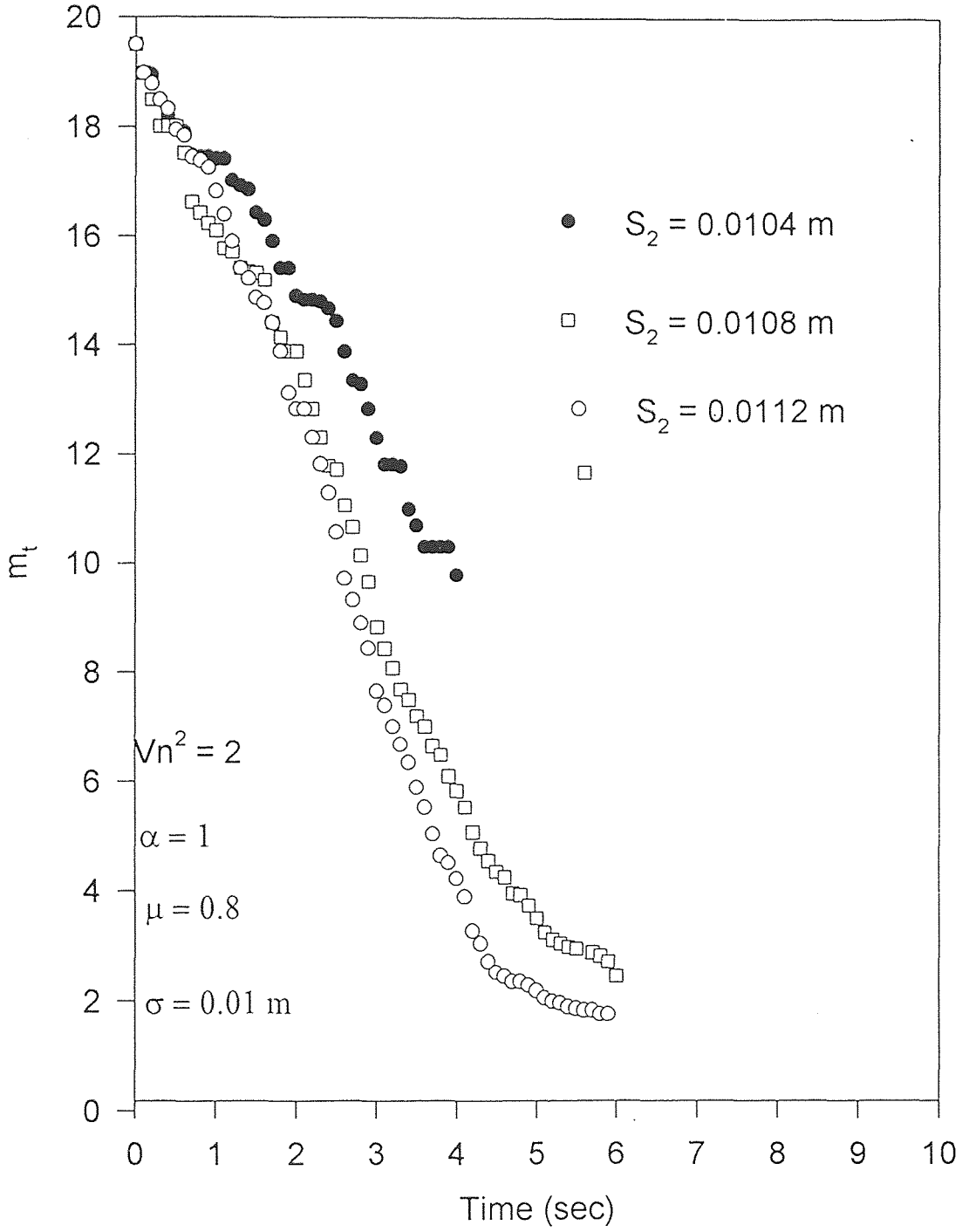

Figure A3.4(c) Mass hold-up evolution for different sieve apertures. Vn^2=2, α=1, μ=0.8, σ=0.01 m

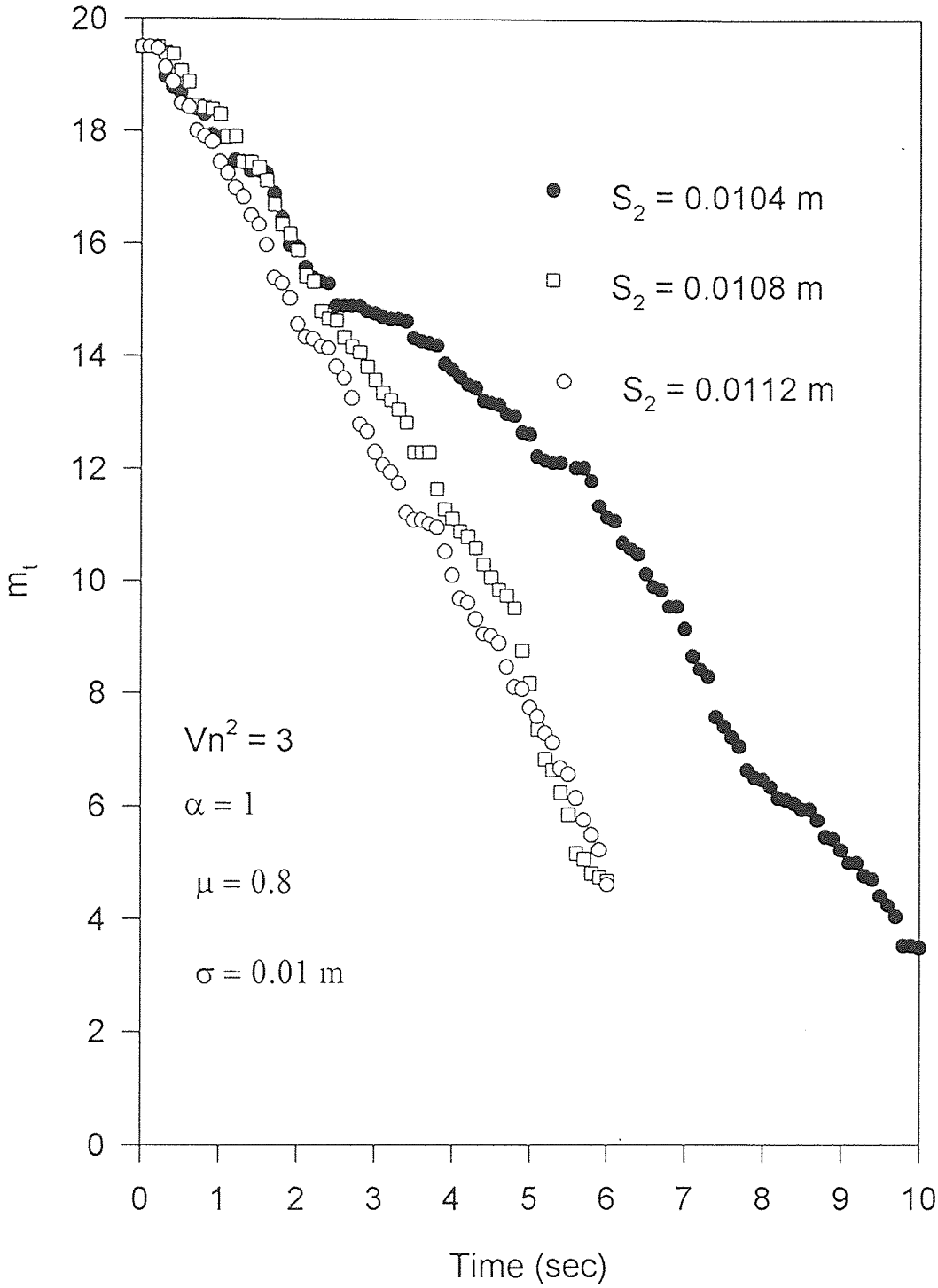

Figure A3.4(d) Mass hold-up evolution for diferent sieve apertures. Vn^2=3, α=1, μ=0.8, σ=0.01m

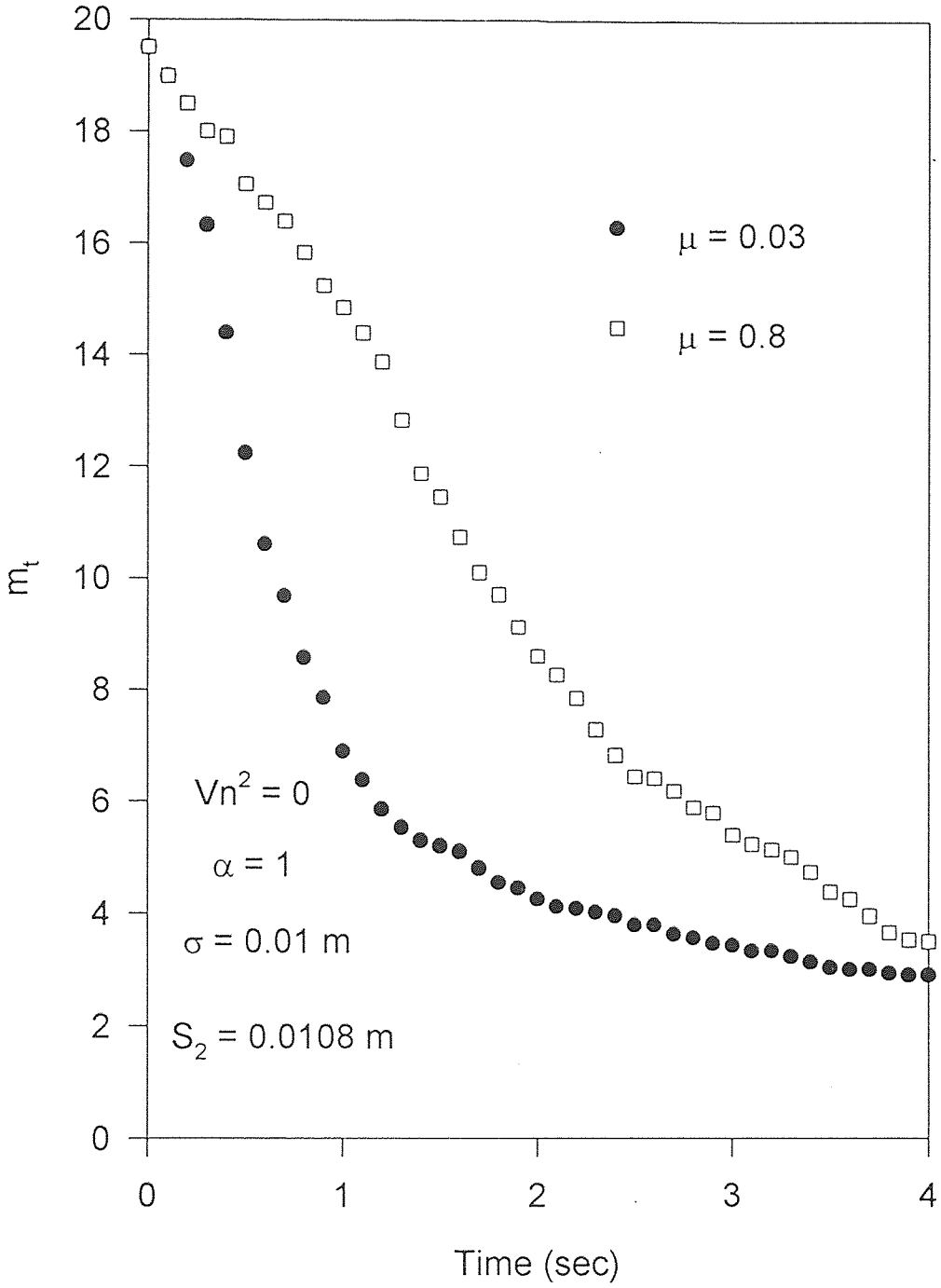

Figure A3.4(e) Mass hold-up evolutin for different friction coefficient $Vn^2 = 0$, $\alpha = 1$, $\sigma = 0.01$ m, $S_2 = 0.0108$m

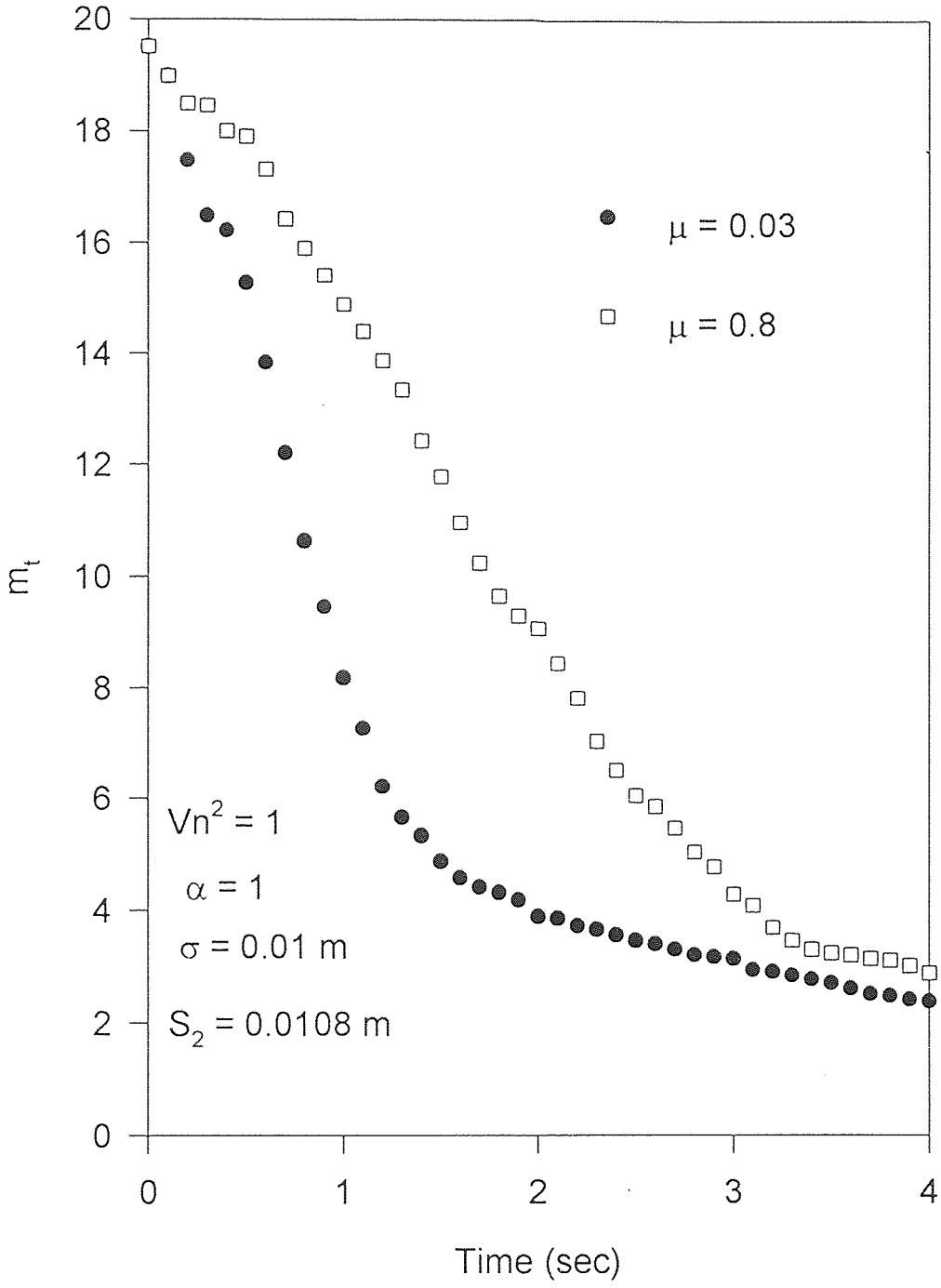

Figure A3.4(f) Mass hold-up evolutin for different friction coefficient $Vn^2 = 1$, $\alpha = 1$, $\sigma = 0.01$ m, $S_2 = 0.0108$m

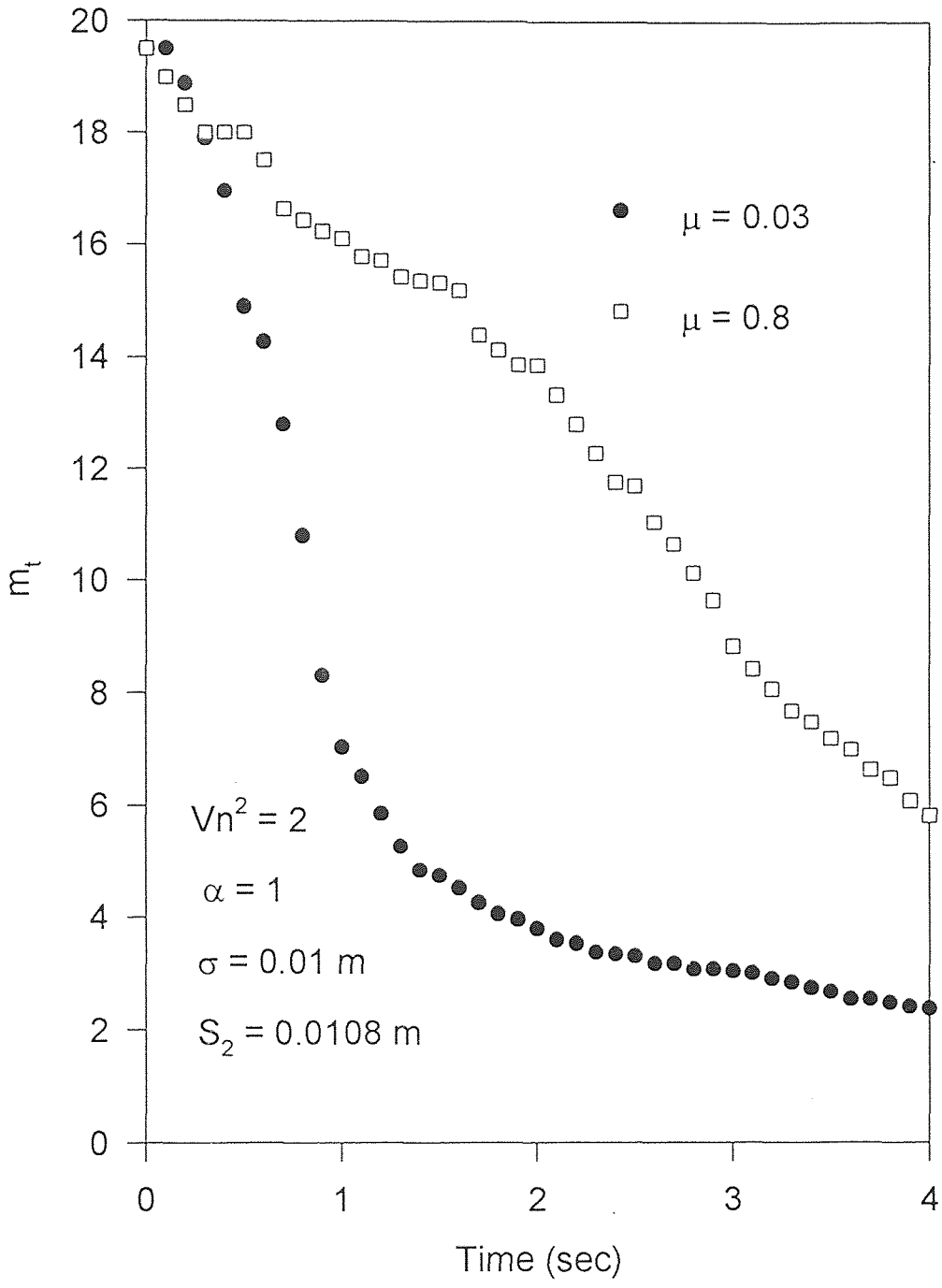

Figure A3.4(g) Mass hold-up evolutin for different friction coefficient $Vn^2 = 2$, $\alpha = 1$, $\sigma = 0.01$ m, $S_2 = 0.0108$m

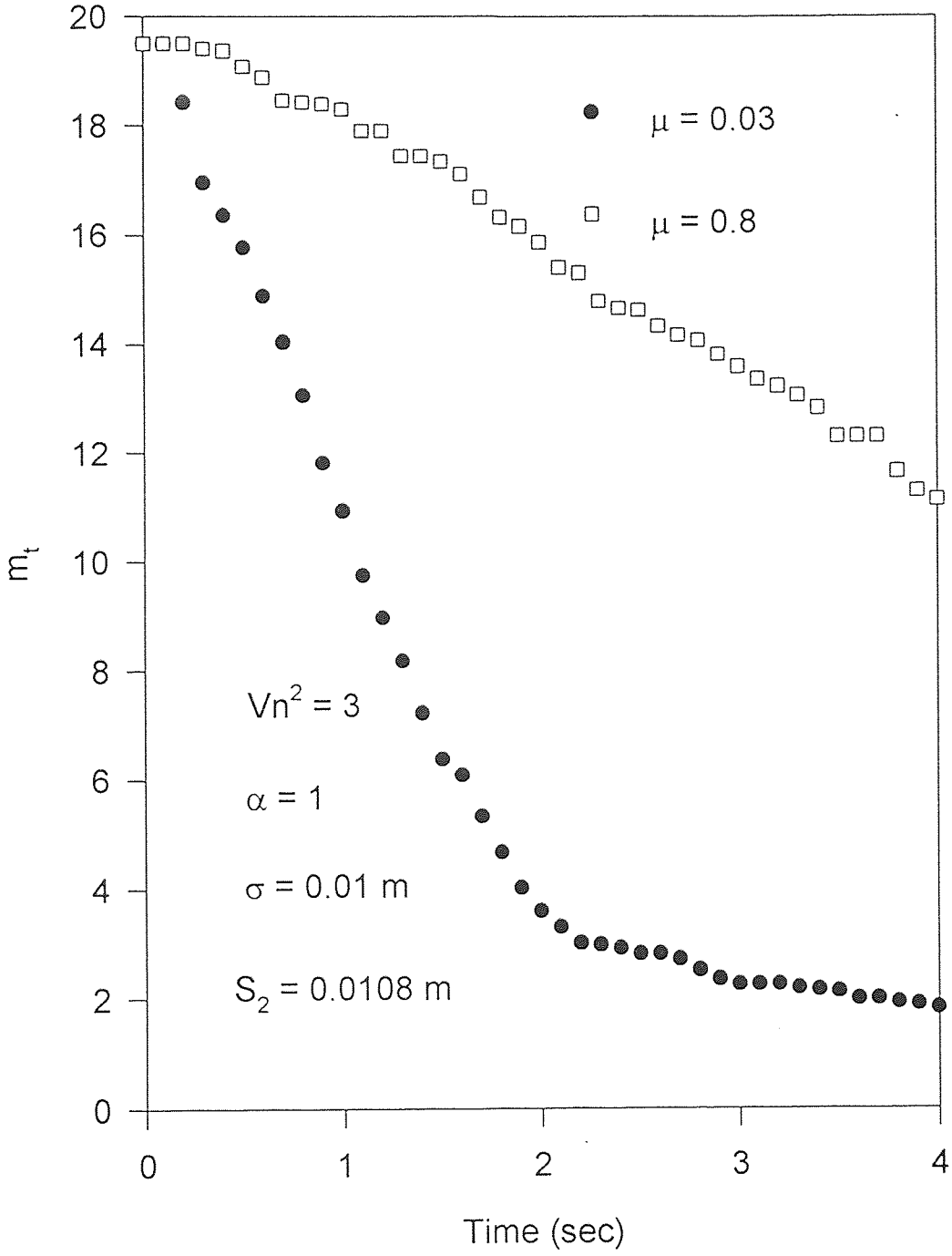

Figure A3.4(h) Mass hold-up evolutin for different friction coefficient

$Vn^2 = 3$, $\alpha = 1$, $\sigma = 0.01$ m, $S_2 = 0.0108$m

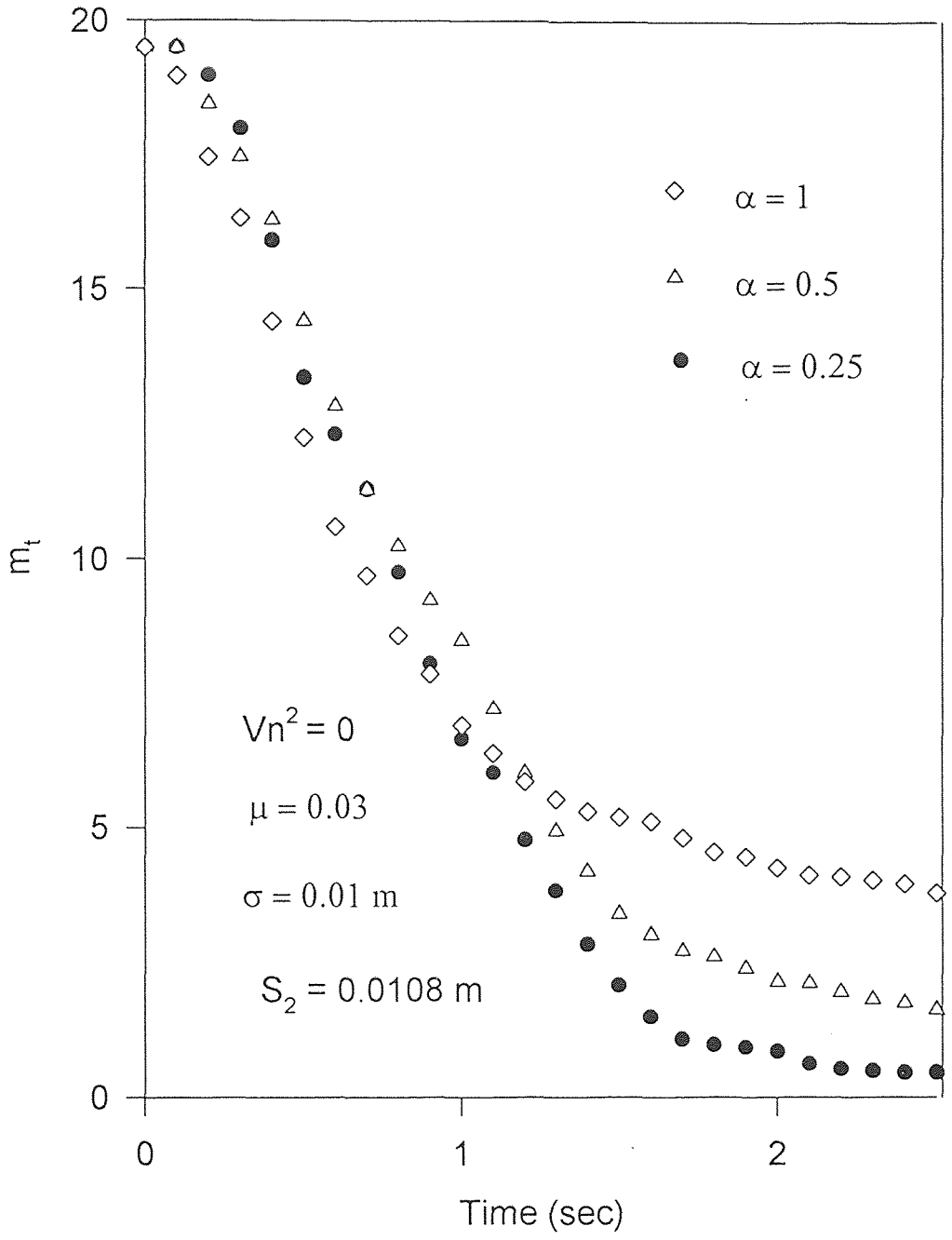

Figure A3.5(a) Mass hold-up evolution for different values of α.
$Vn^2 = 0$, $\mu = 0.03$, $\sigma = 0.01$ m, $S_2 = 0.0108$ m

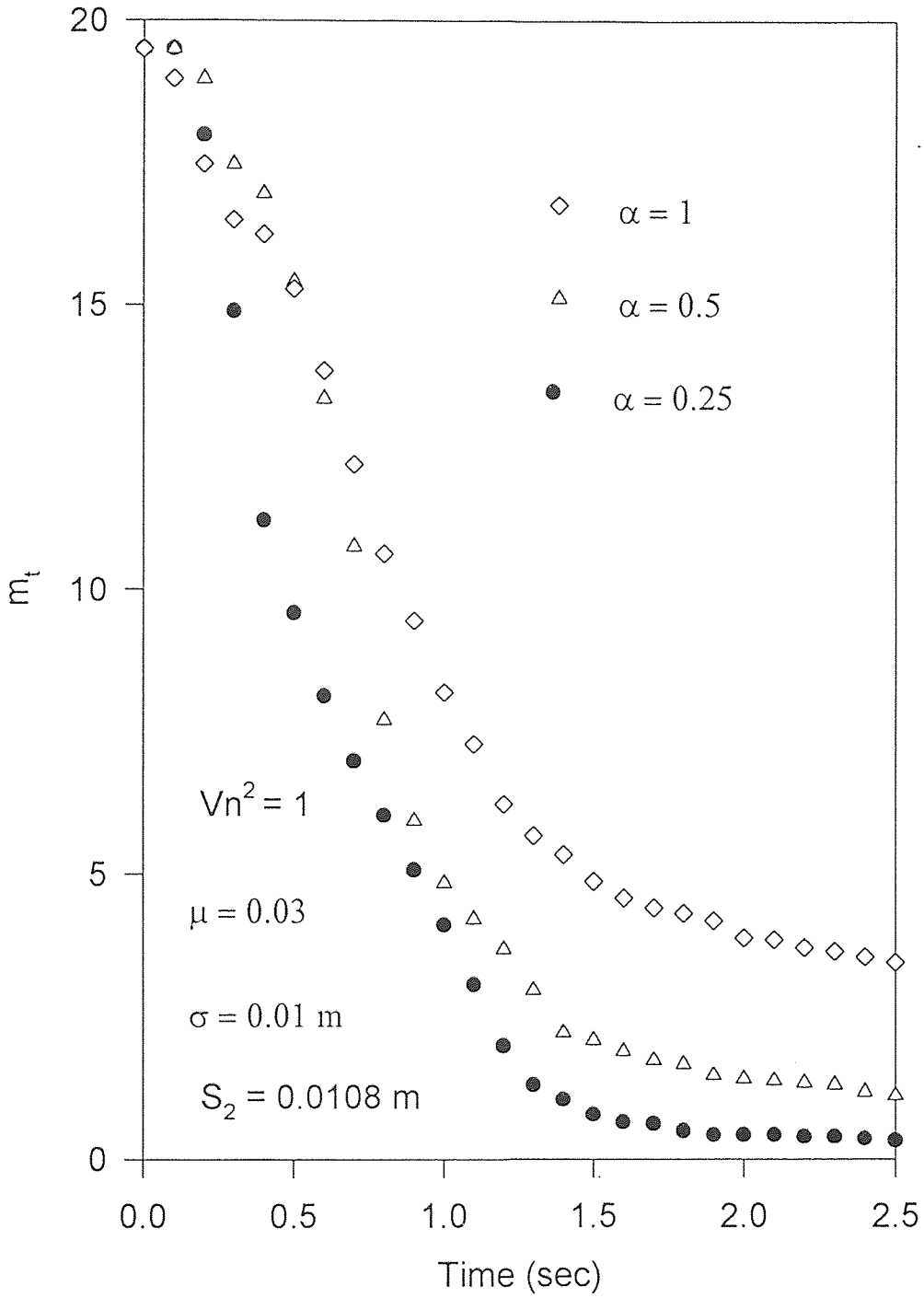

Figure A3.5(b) Mass hold-up evolution for differentvalues of α.
$Vn^2 = 1$, $\mu = 0.03$, $\sigma = 0.01$ m, $S_2 = 0.0108$ m

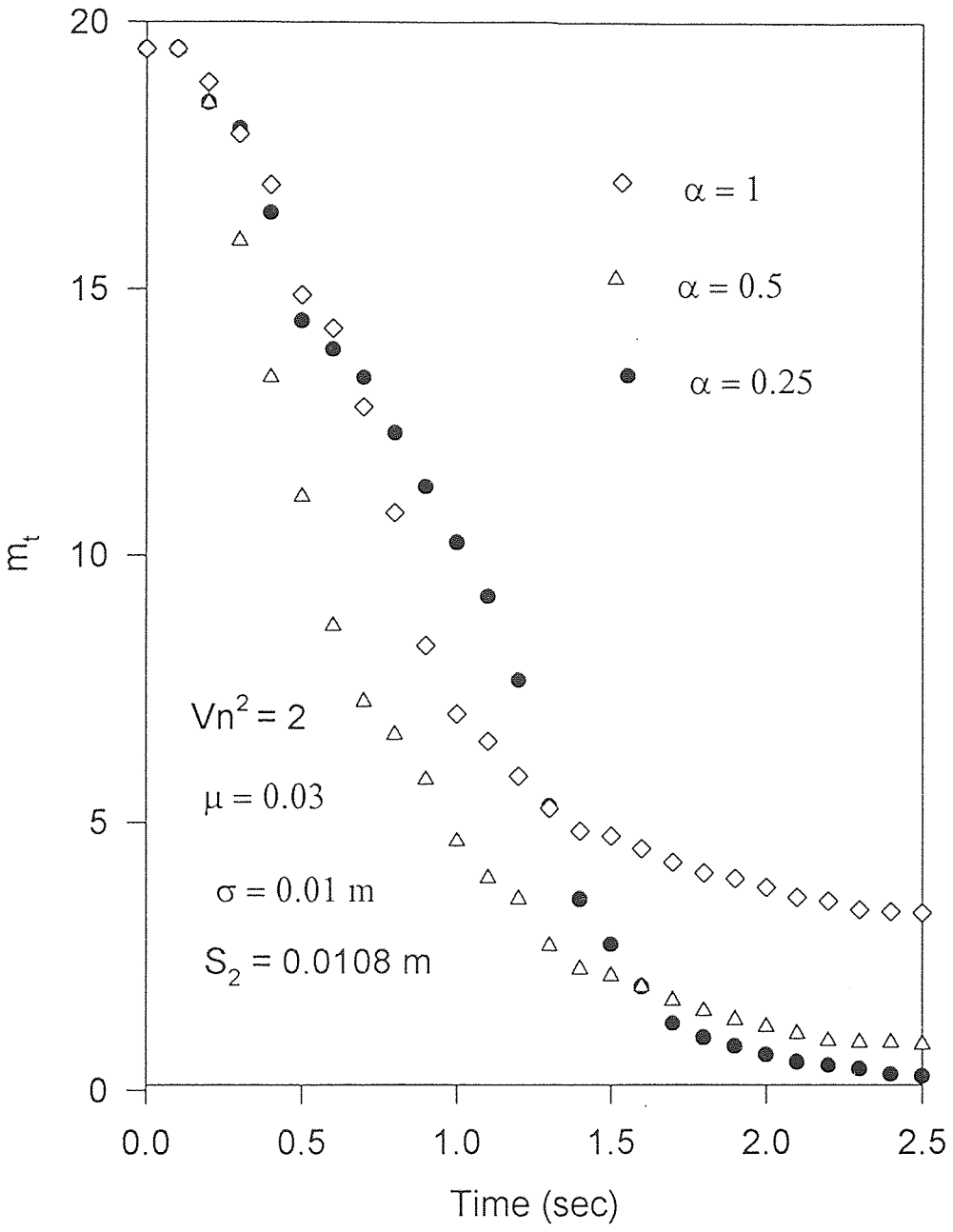

Figure A3.5(c) Mass hold-up evolution for different values of a. $Vn^2 = 2$, $\mu = 0.03$, $\sigma = 0.01$ m, $S_2 = 0.0108$ m

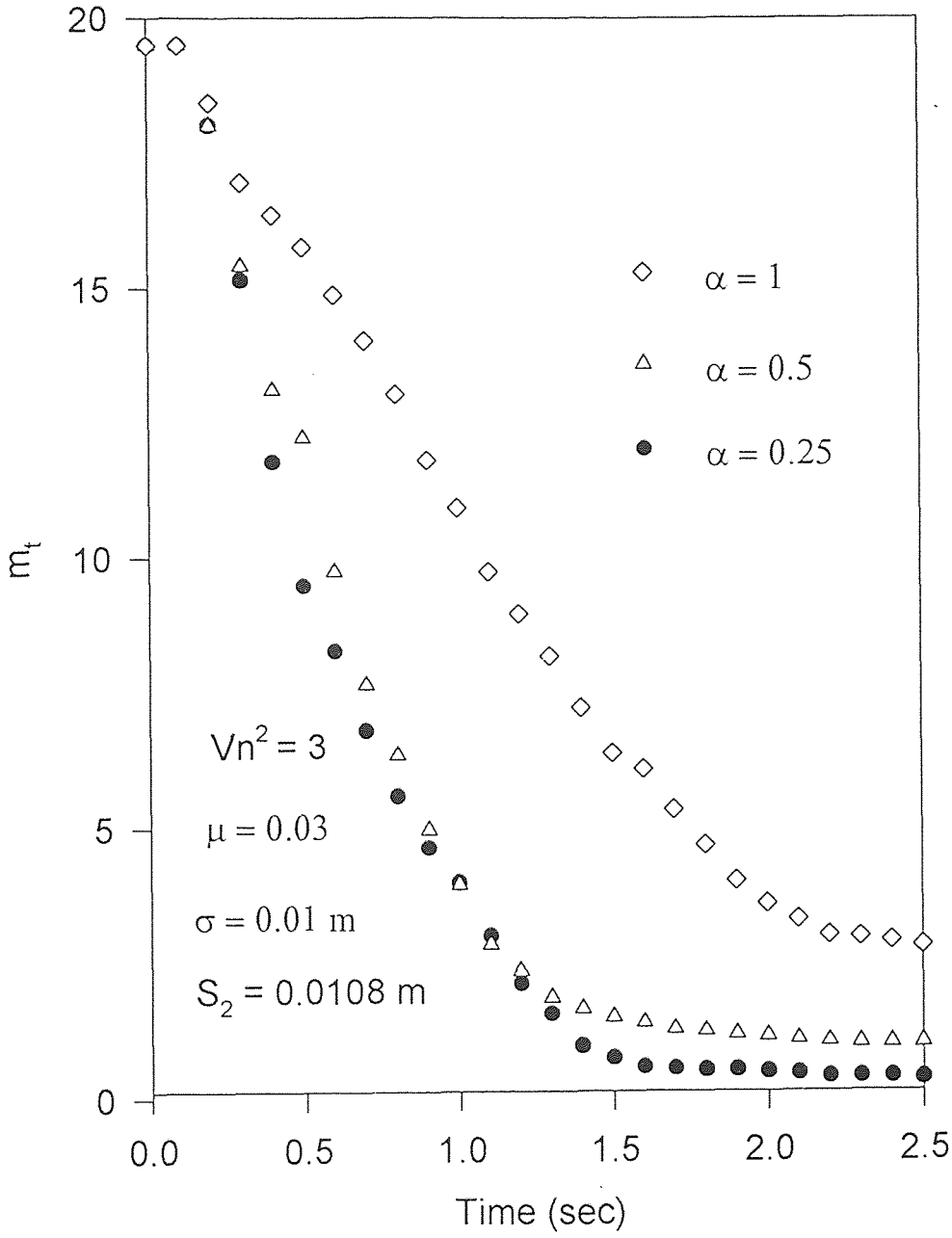

Figure 3.5(d) Mass hold-up evolution for different values of α.
$Vn^2 = 3$, $\mu = 0.03$, $\sigma = 0.01$ m, $S_2 = 0.0108$ m

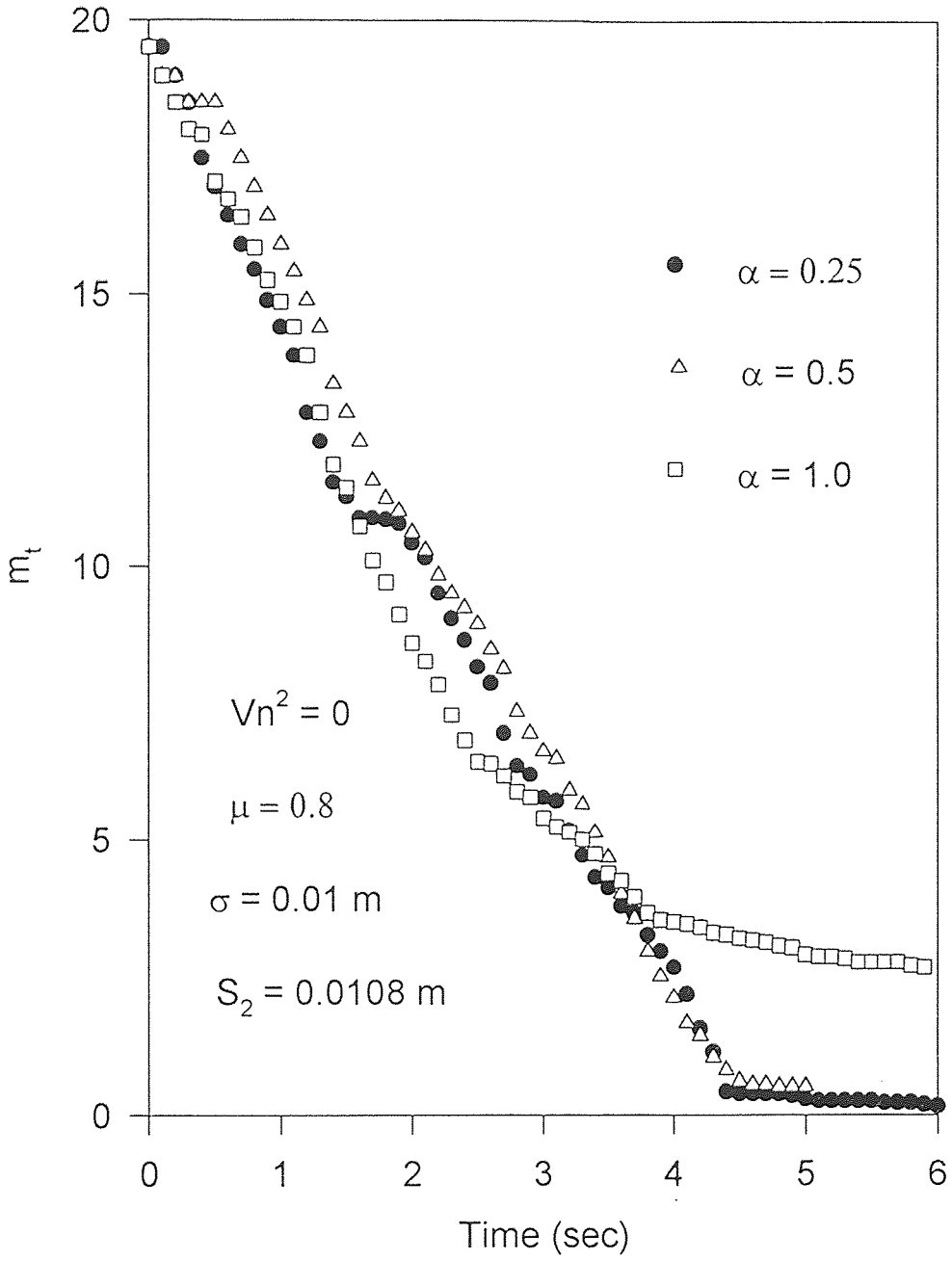

Figure A3.6(a) Mass hold-up evolution for different values of α.
$Vn^2 = 0$, μ = 0.8, σ = 0.01 m, S_2 = 0.0108 m

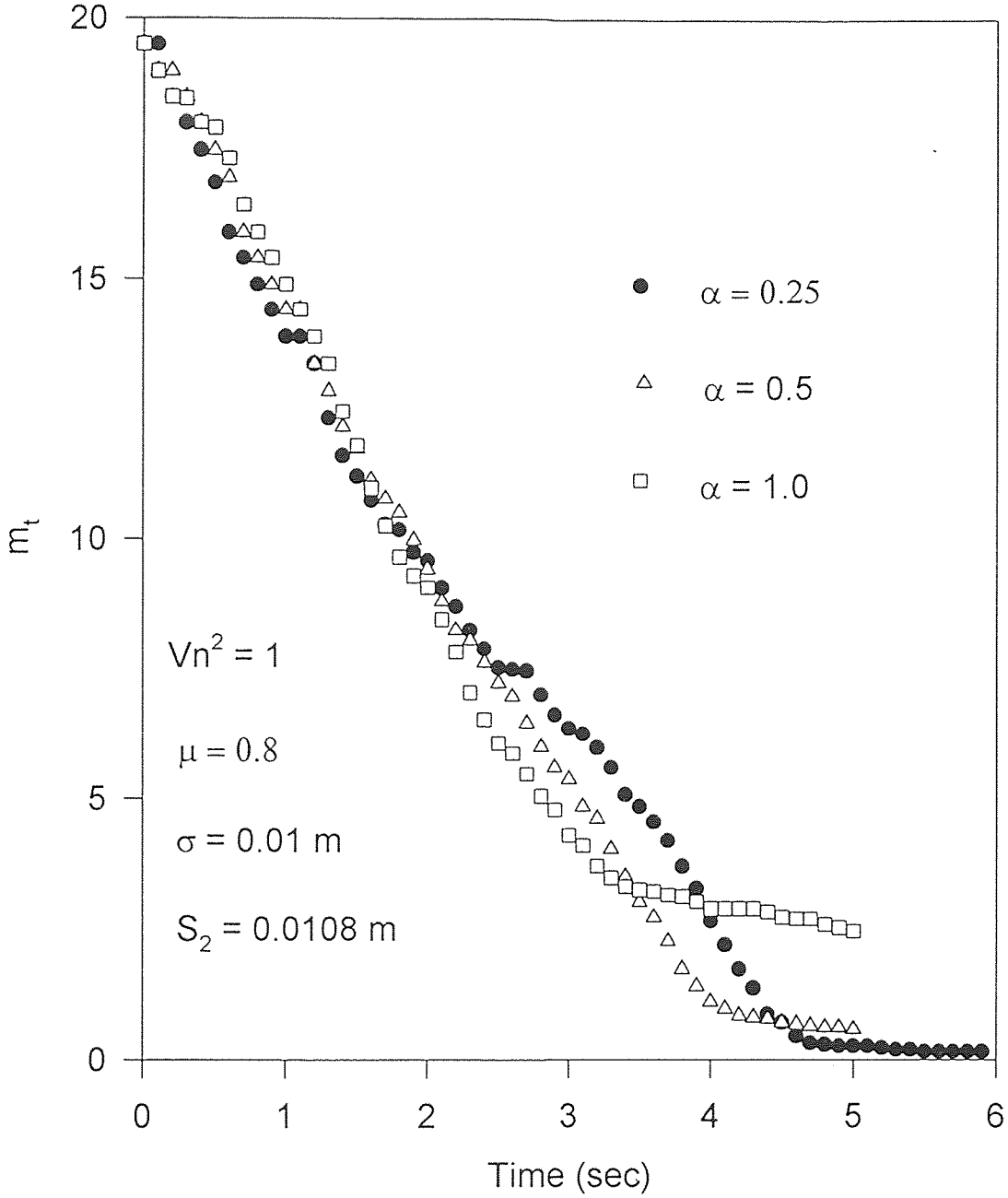

Figure A3.6(b) Mass hold-up evolution for different values of α.
$Vn^2 = 1$, μ = 0.8, σ = 0.01 m, S_2 = 0.0108 m

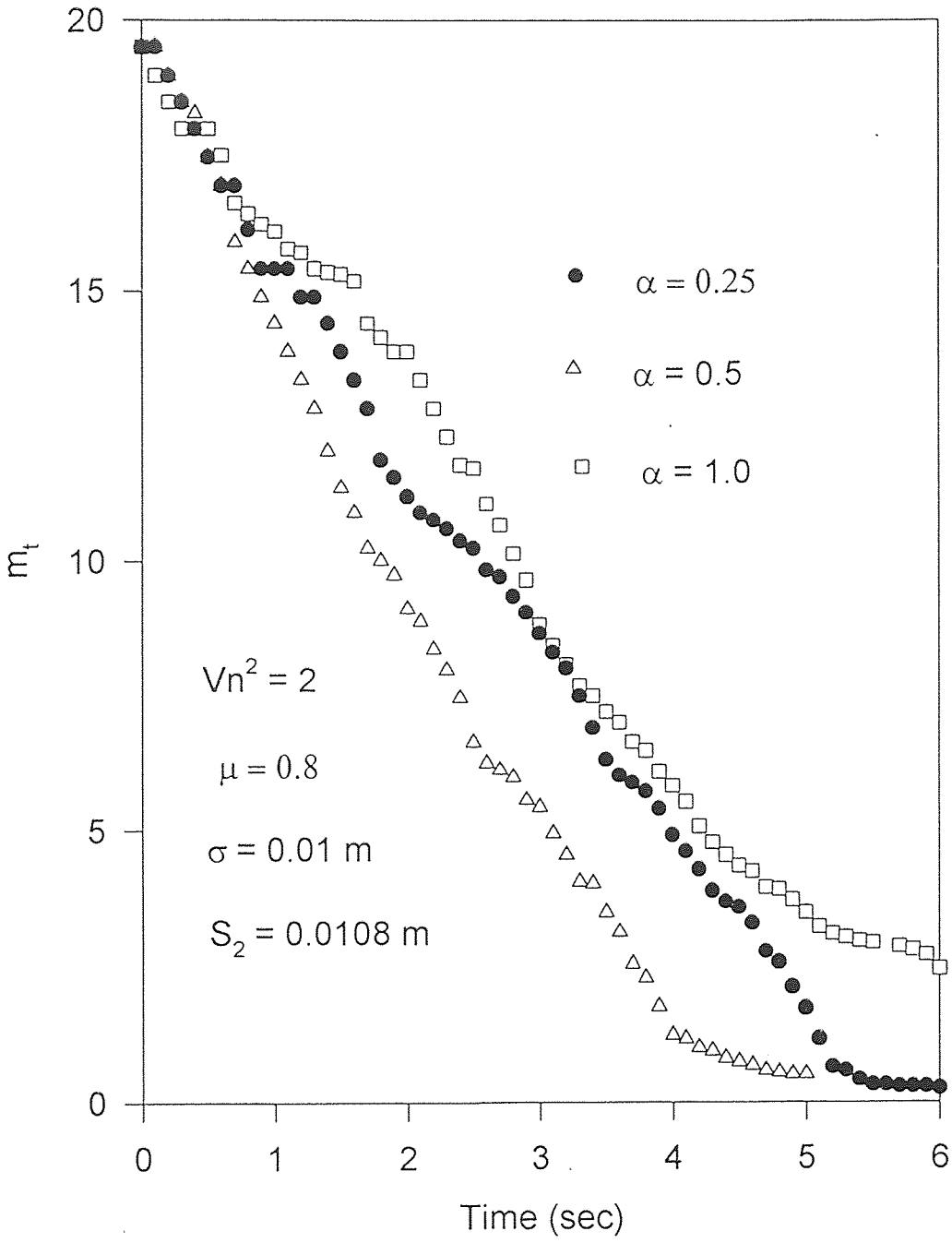

Figure A3.6(c) Mass hold-up evolution for different values of α.
$Vn^2 = 2$, μ = 0.8, σ = 0.01 m, S_2 = 0.0108 m

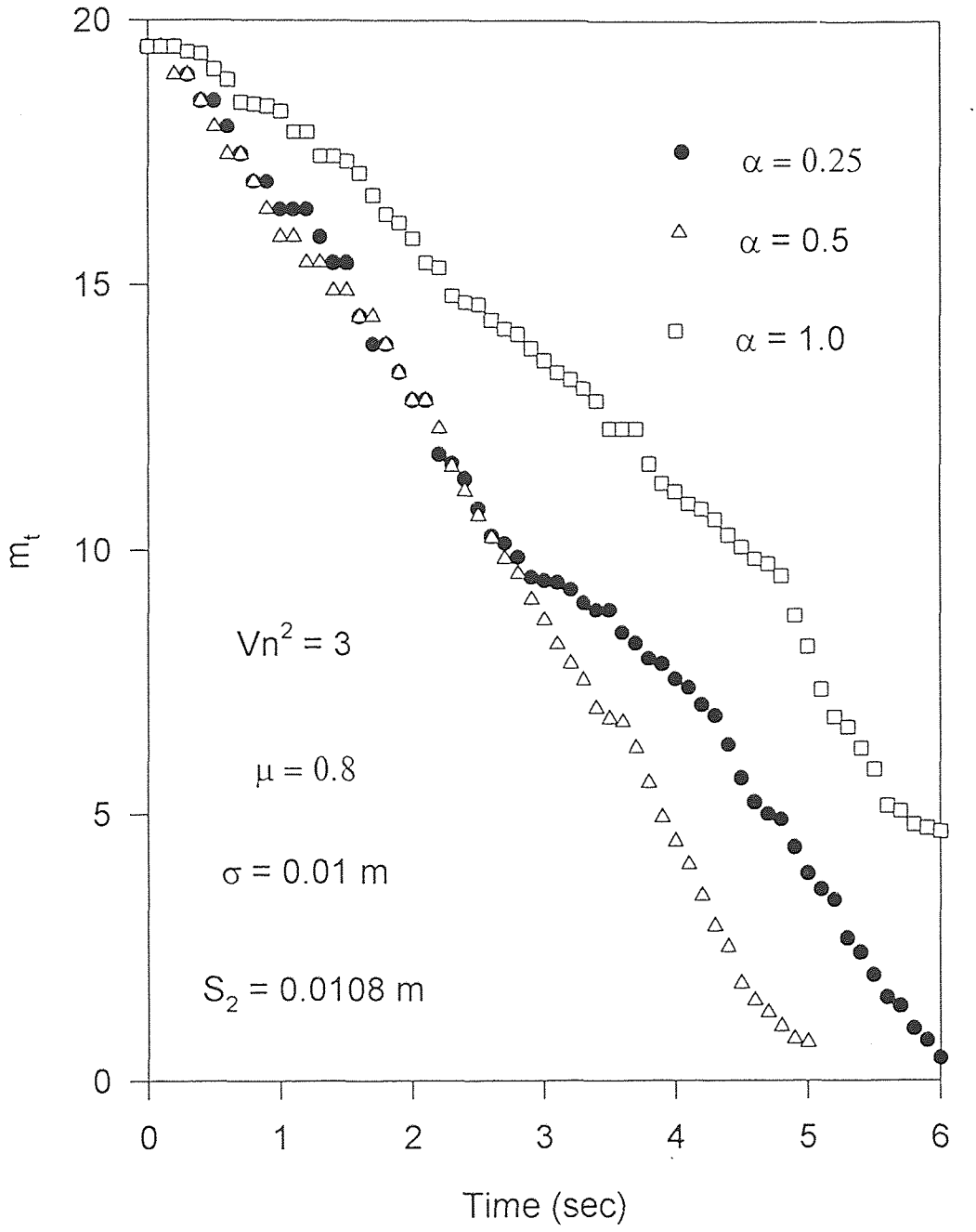

Figure A3.6(d) Mass hold-up evolution for different values of α.
$Vn^2 = 3$, μ = 0.8, σ = 0.01 m, S_2 = 0.0108 m

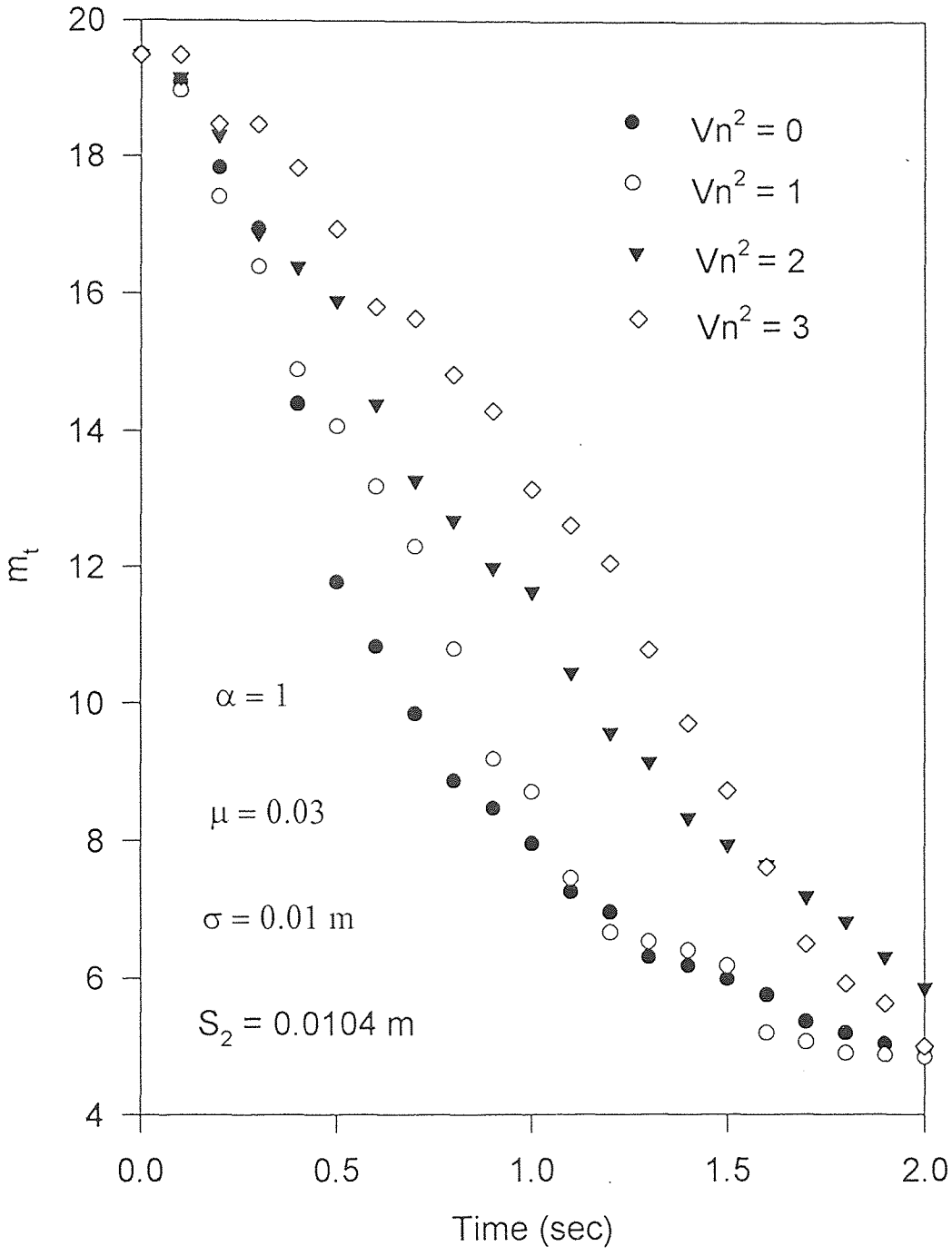

Figure A3.7(a) Mass hold-up evolution for different values of Vn^2. $\alpha = 1$, $\mu = 0.03$, $\sigma = 0.01$ m, $S_2 = 0{,}0104$ m

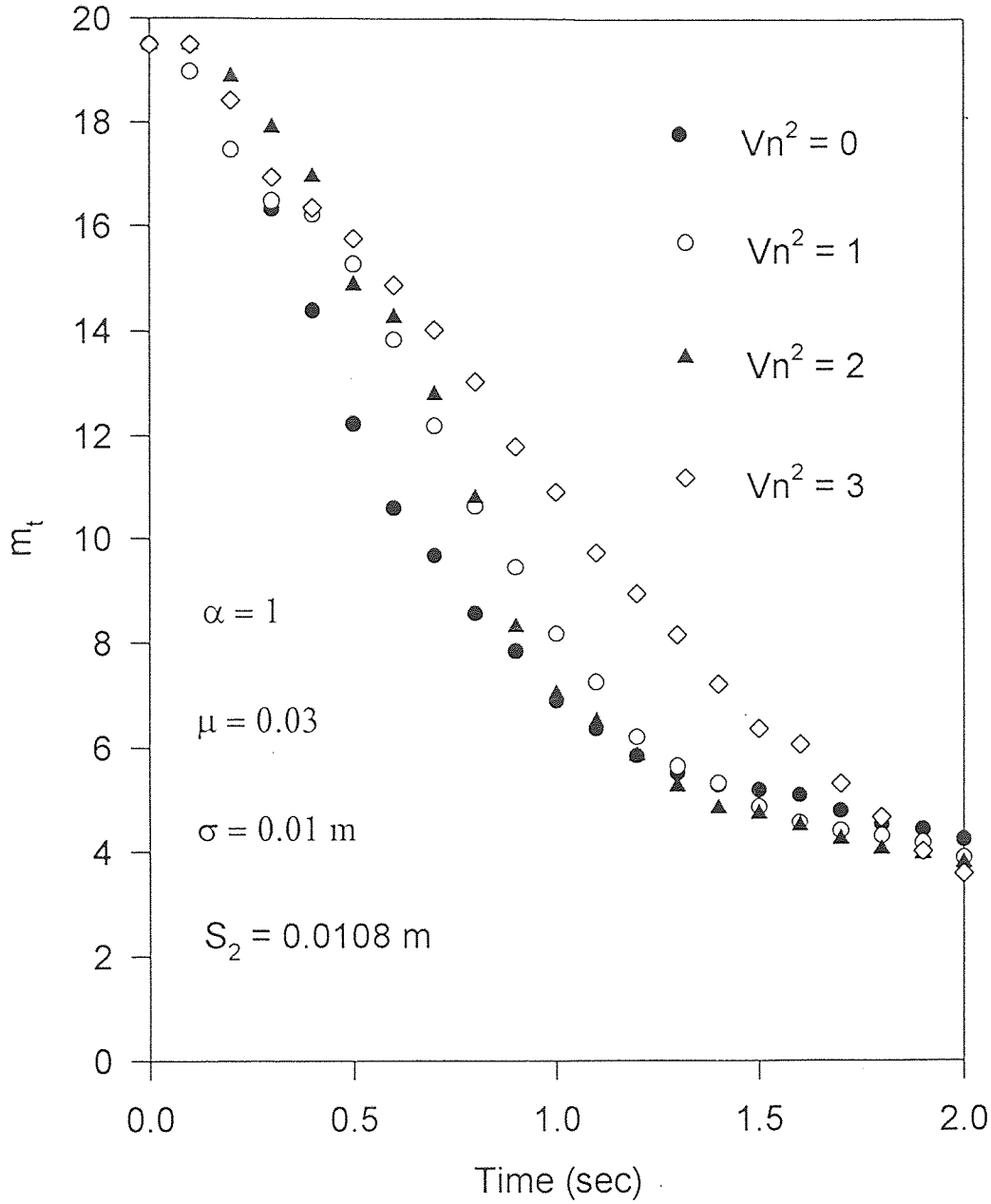

Figure A3.7(b) Mass hold-up evolution for different values of Vn^2.
a = 1, m = 0.03, s = 0.01 m, S_2 = 0.0108 m

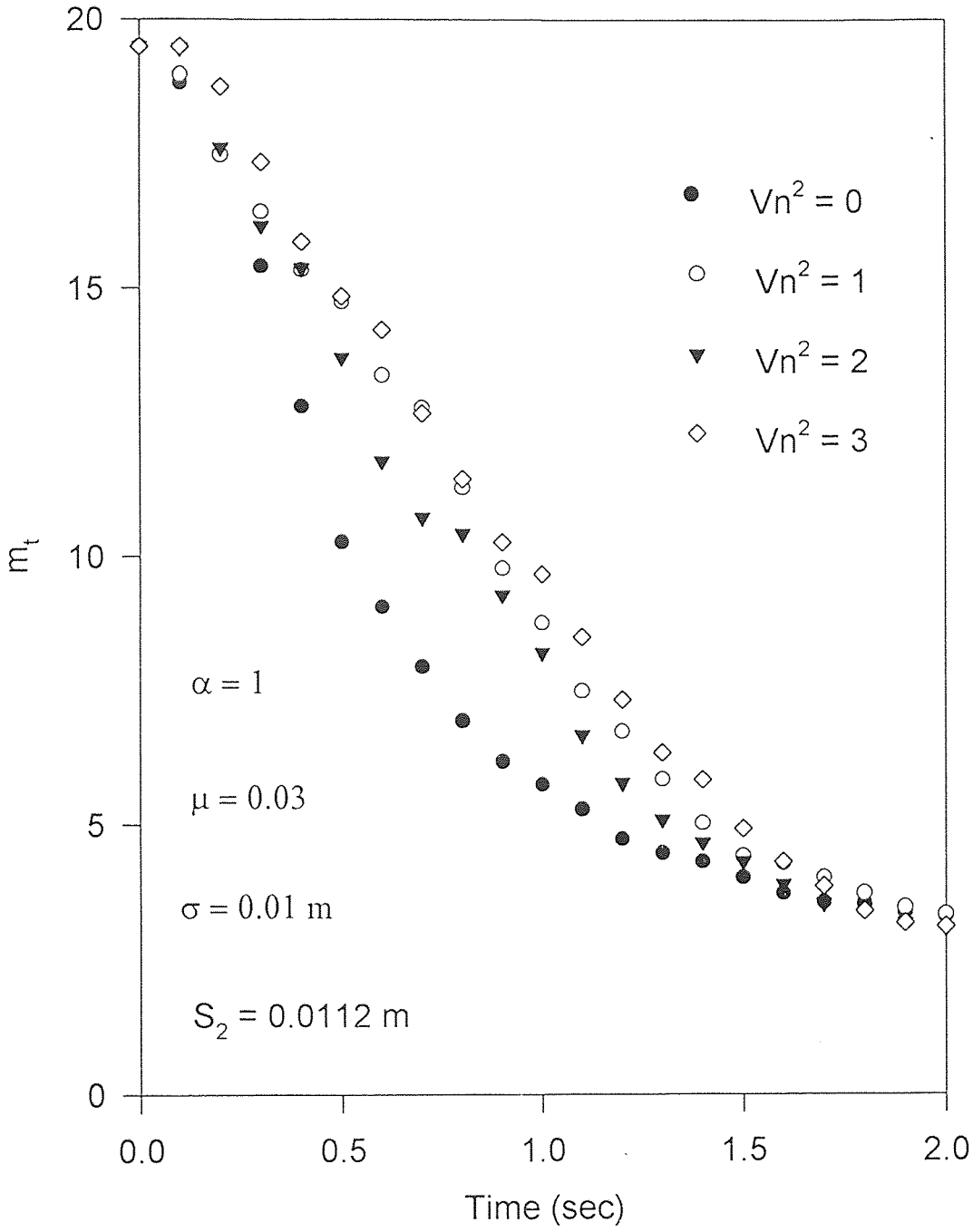

Figure A3.7(c) Mass hold-up evolution for different values of Vn^2.
$\alpha = 1$, $\mu = 0.03$, $\sigma = 0.01$ m, $S_2 = 0.0112$ m

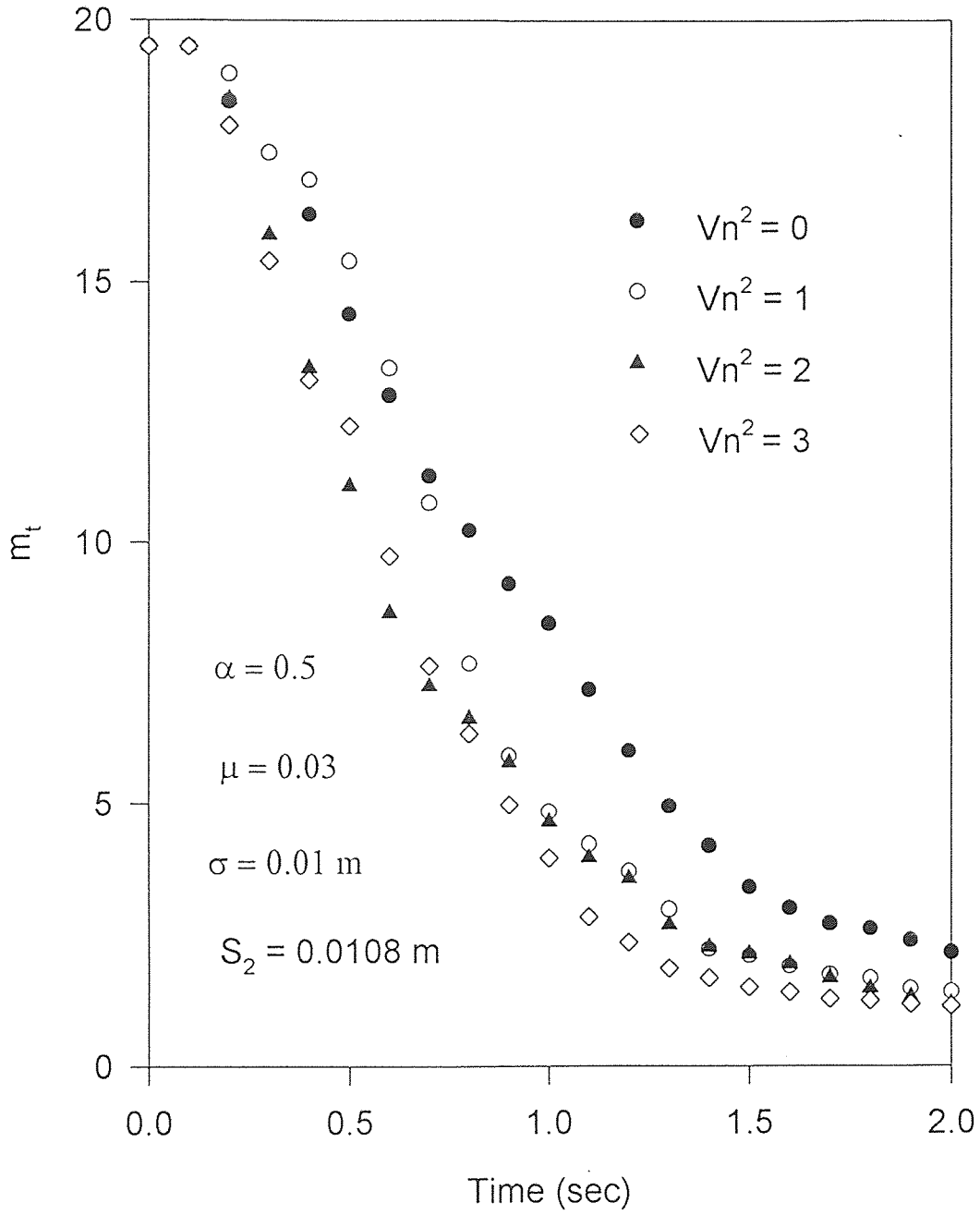

Figure A3.7(d) Mass hold-up evolution for different values of Vn^2
a = 0.5, μ = 0.03, σ = 0.01 m, S_2 = 0.0108 m

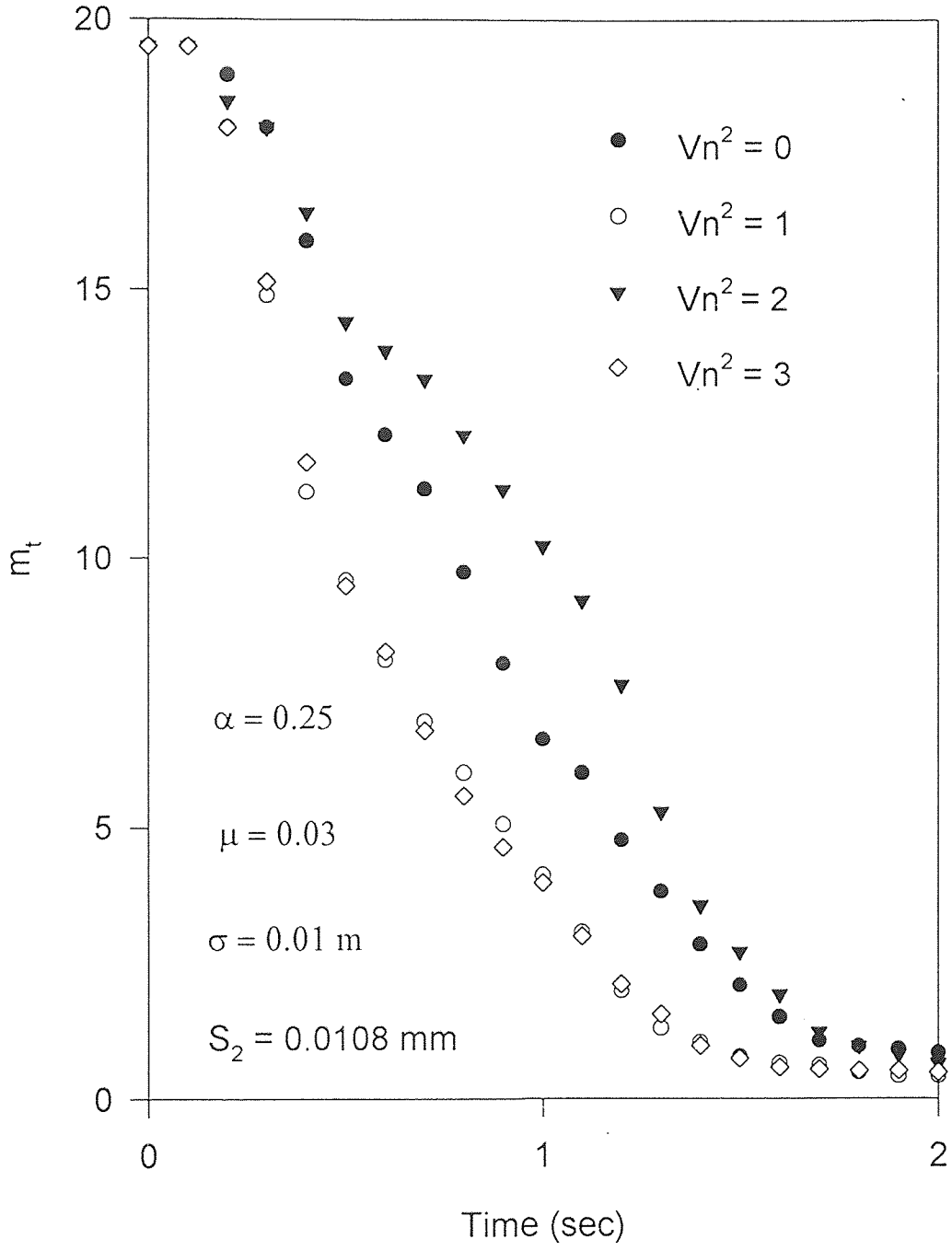

Figure A3.7(e) Mass hold-up evolution for different values of Vn^2
a = 0.25, μ = 0.03, σ = 0.01 m, S_2 = 0.0108 m

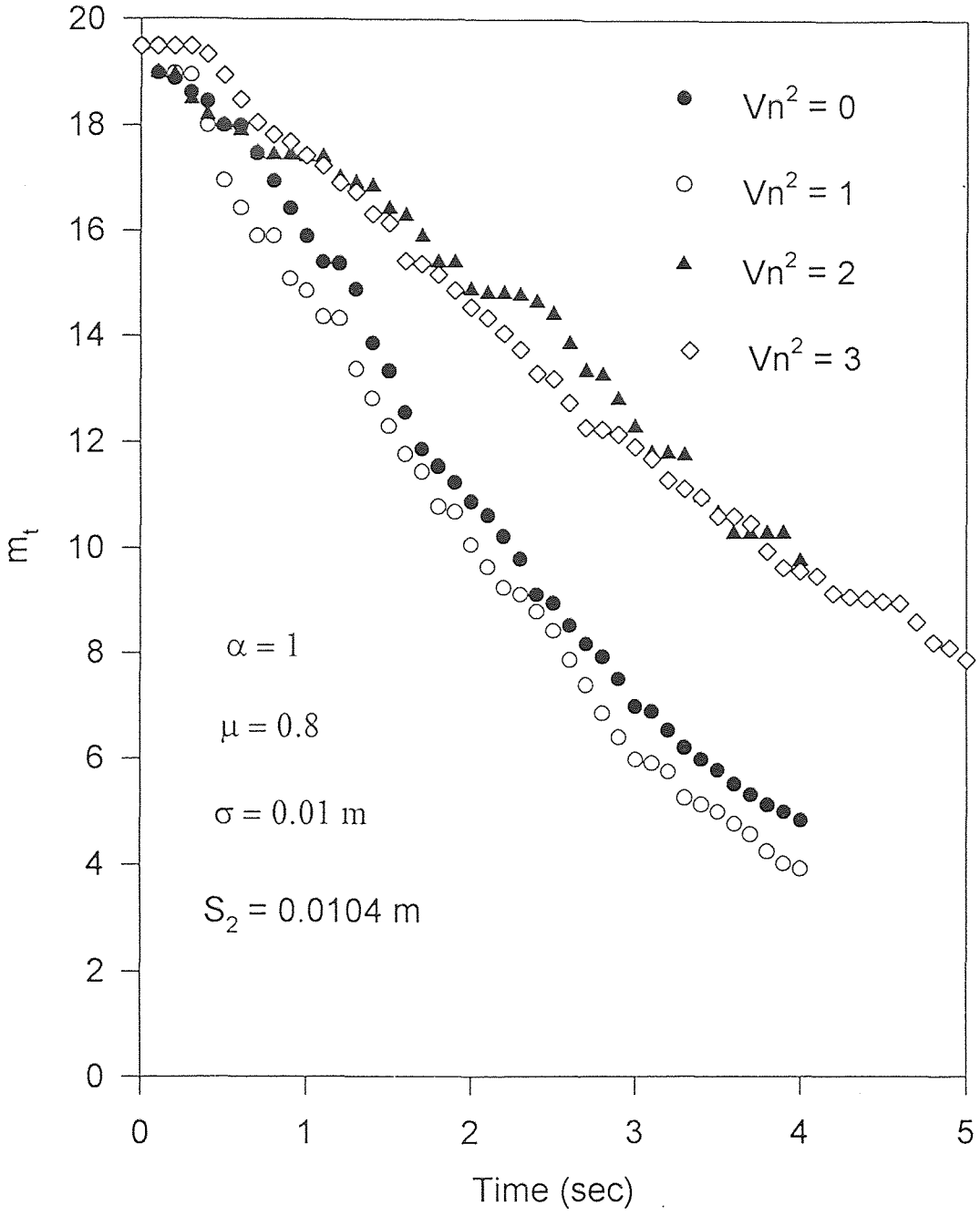

Figure A3.8(a) Mass hold-up evolution for different values of Vn^2.
$\alpha = 1$, $\mu = 0.8$, $\sigma = 0.01$ m, $S_2 = 0.0104$ m

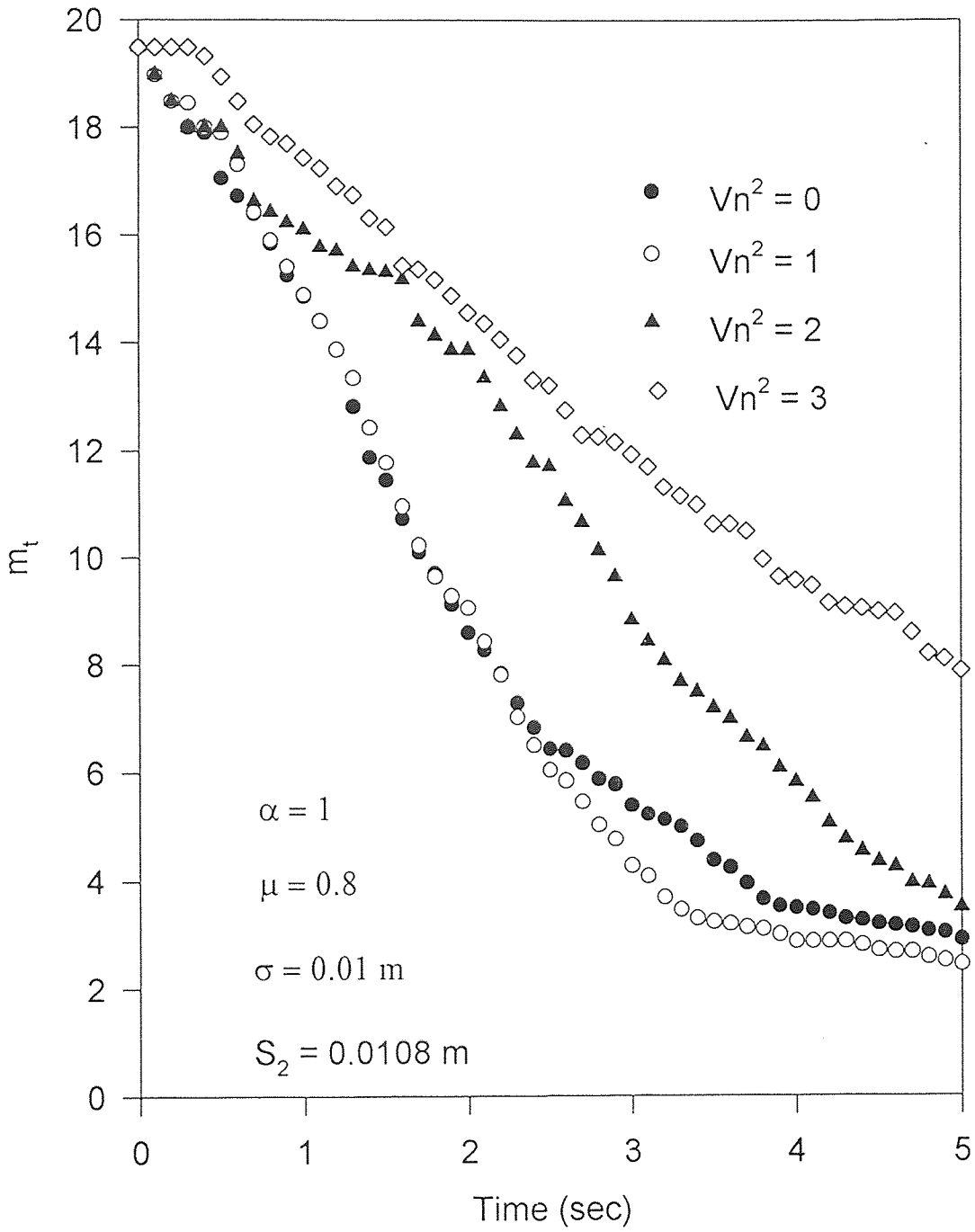

Figure A3.8(b) Mass hold-up evolution for different values of Vn^2.
$\alpha = 1$, $\mu = 0.8$, $\sigma = 0.01$ m, $S_2 = 0.0108$ m

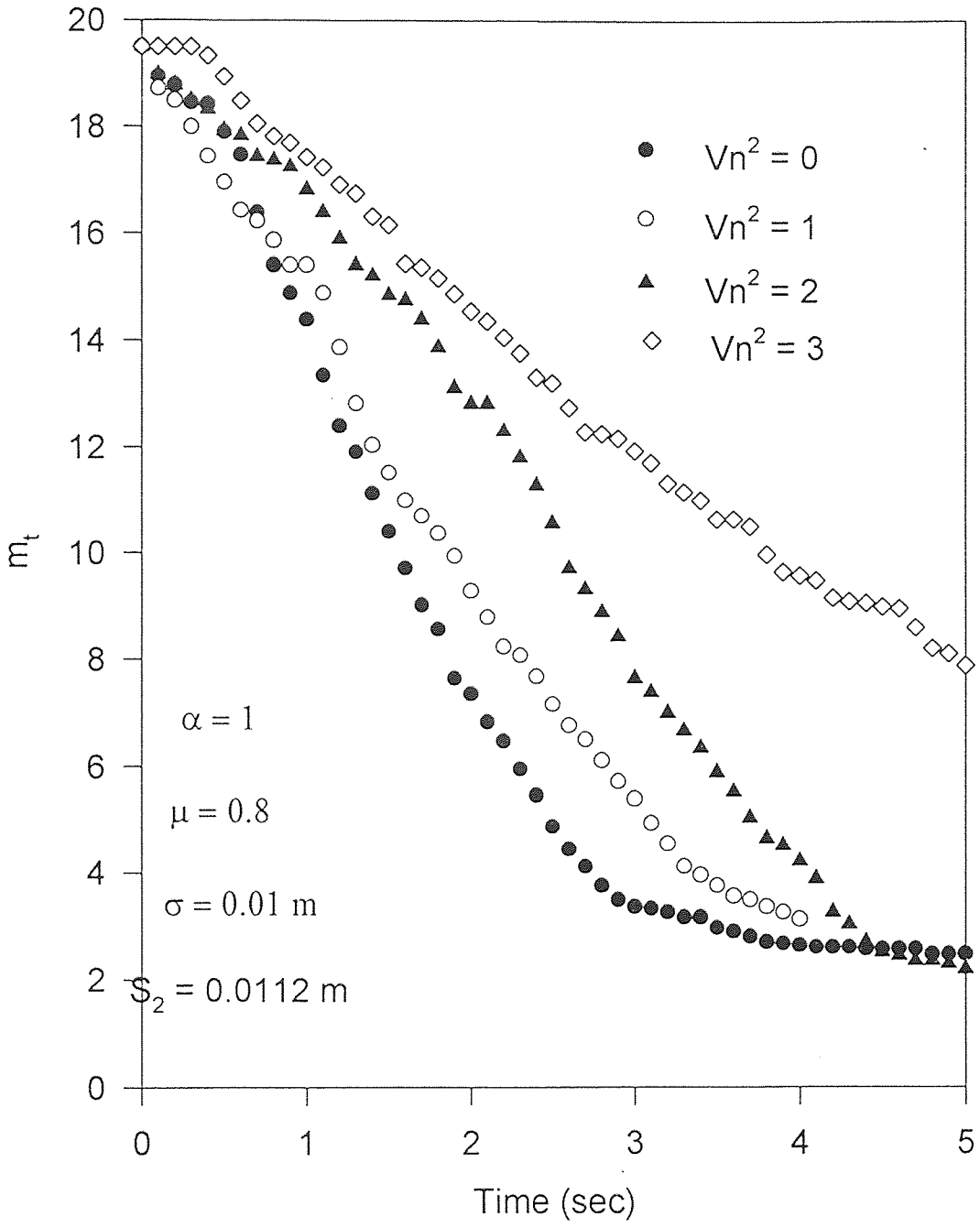

Figure A3.8(c) Mass hold-up evolution for different values of Vn^2.
$\alpha = 1$, $\mu = 0.8$, $\sigma = 0.01$ m, $S_2 = 0.0112$ m

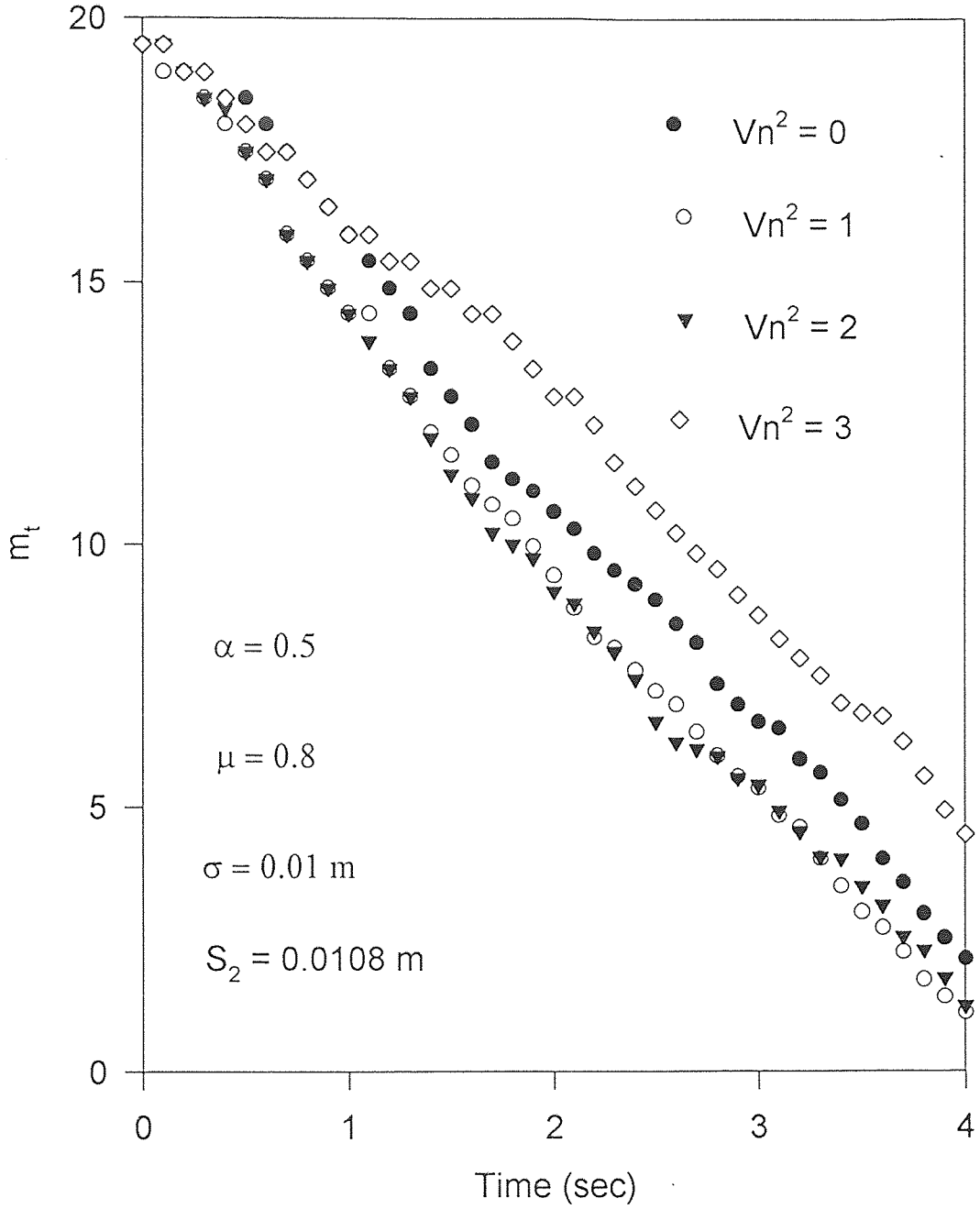

Figure A3.8(d) Mass hold-up evolution for different values of Vn^2.
$\alpha = 0.5$, $\mu = 0.8$, $\sigma = 0.01$ m, $S_2 = 0.0108$ m

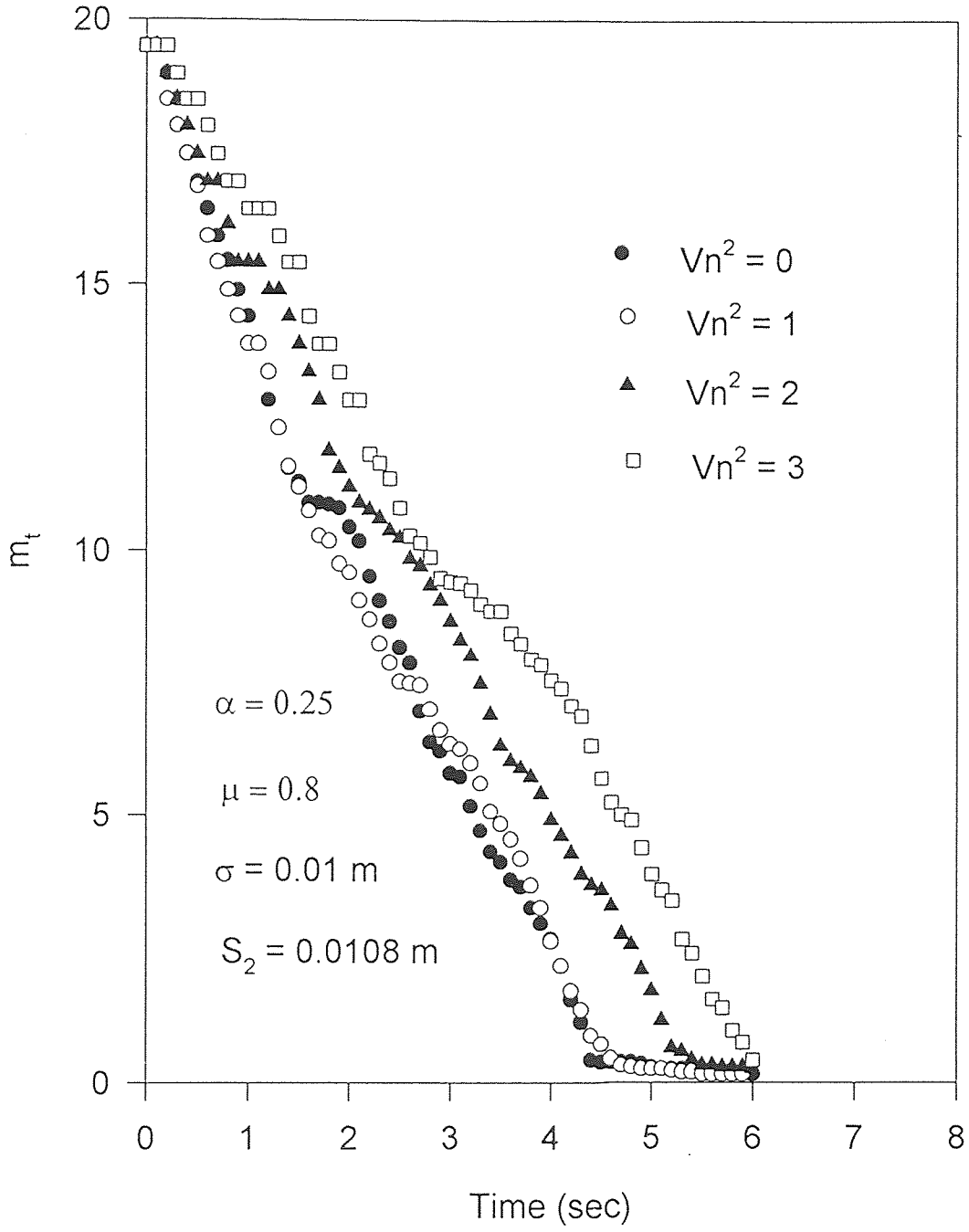

Figure A3.8(e) Mass hold-up evolution for different values of Vn^2.
$\alpha = 0.25$, $\mu = 0.8$, $\sigma = 0.01$ m, $S_2 = 0.0108$ m

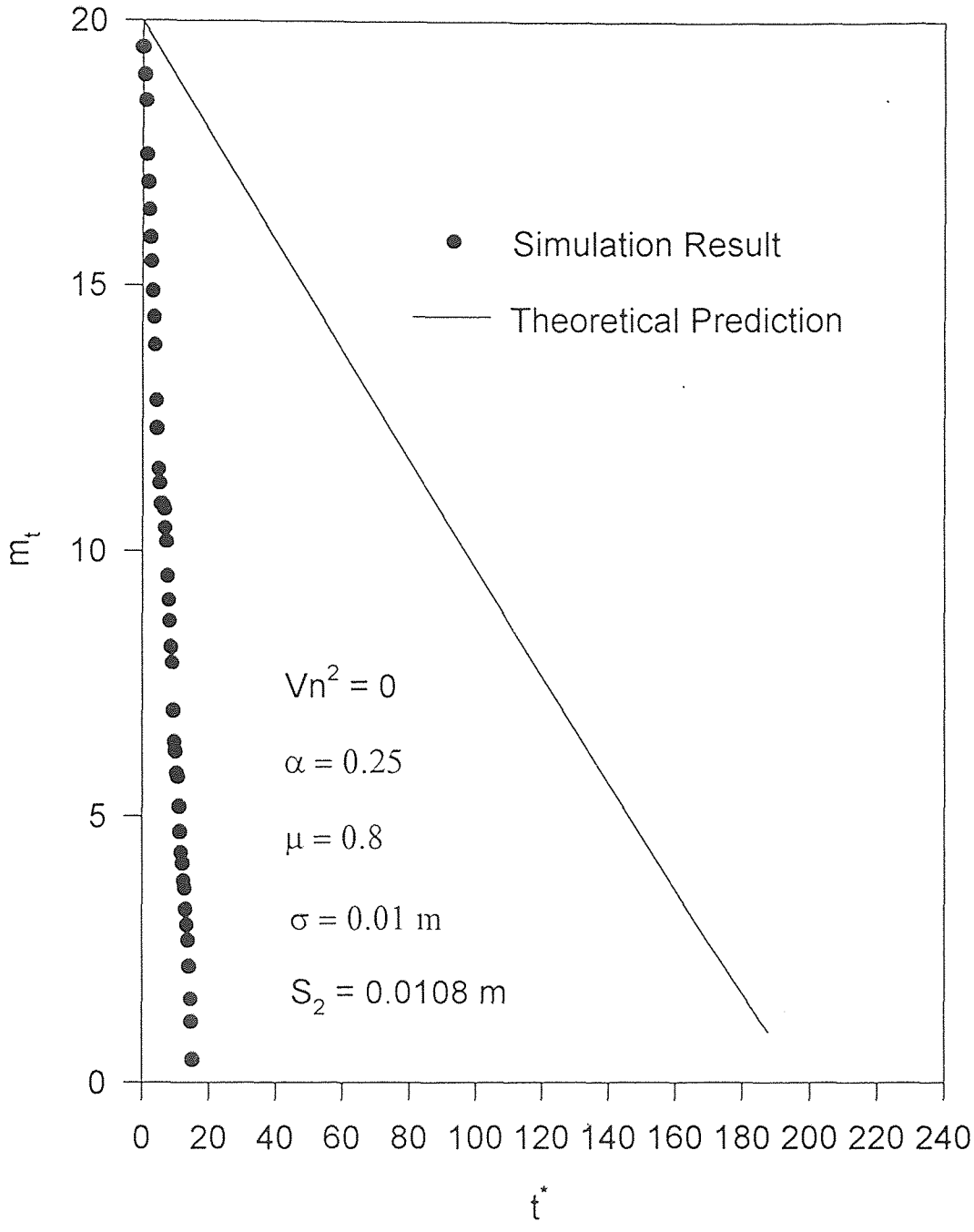

Figure A3.9(a) Mass hold-up profile compared with the theoretical prediction for $Vn^2 = 0$, $\alpha = 0.25$, $\mu = 0.8$, $\sigma = 0.01$ m, $S_2 = 0.0108$ m

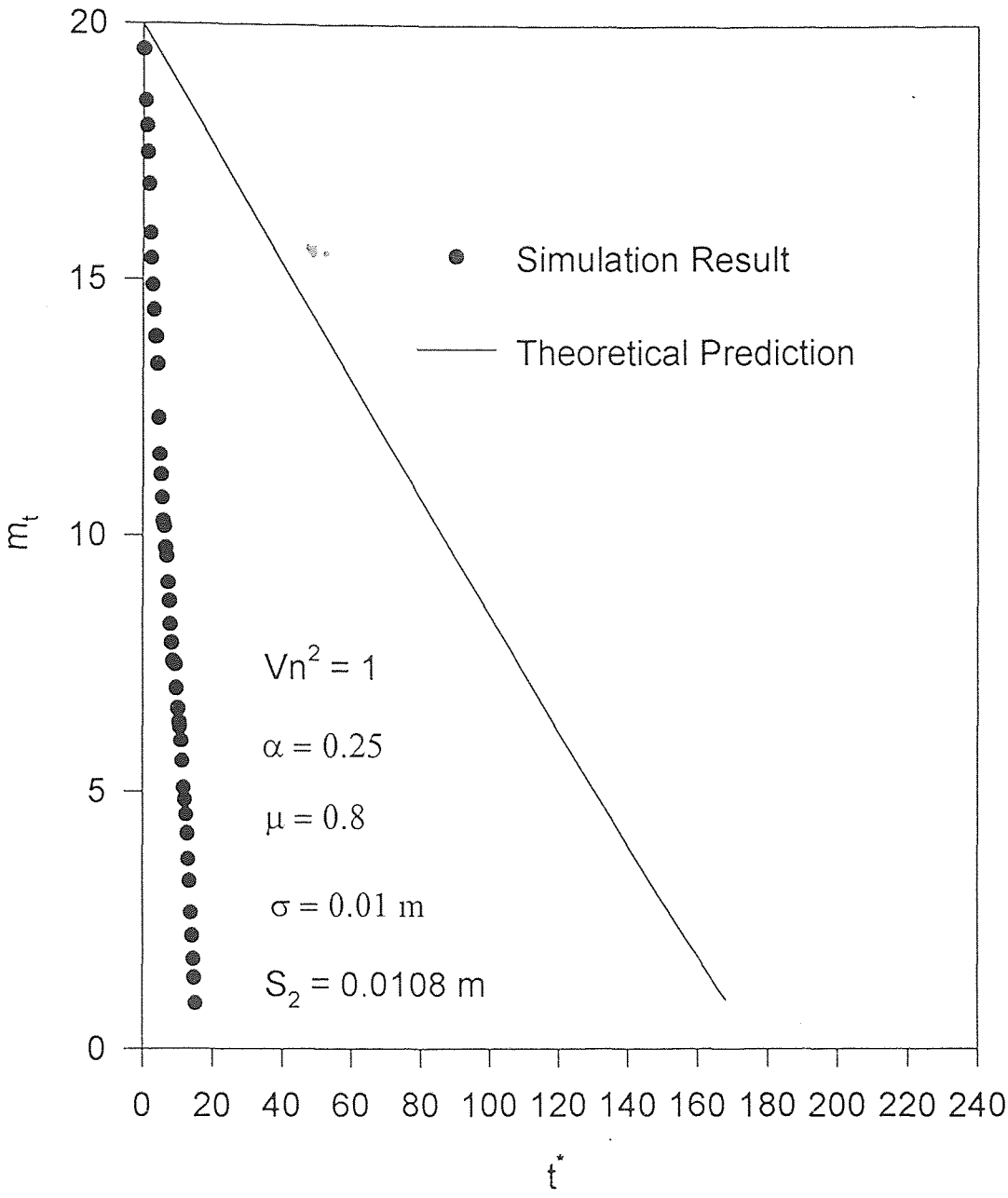

Figure A3.9(b) Mass hold-up profile compared with theoretical prediction for $Vn^2 = 1$, $\alpha = 0.25$, $\mu = 0.8$, $\sigma = 0.01$ m, $S_2 = 0.0108$ m

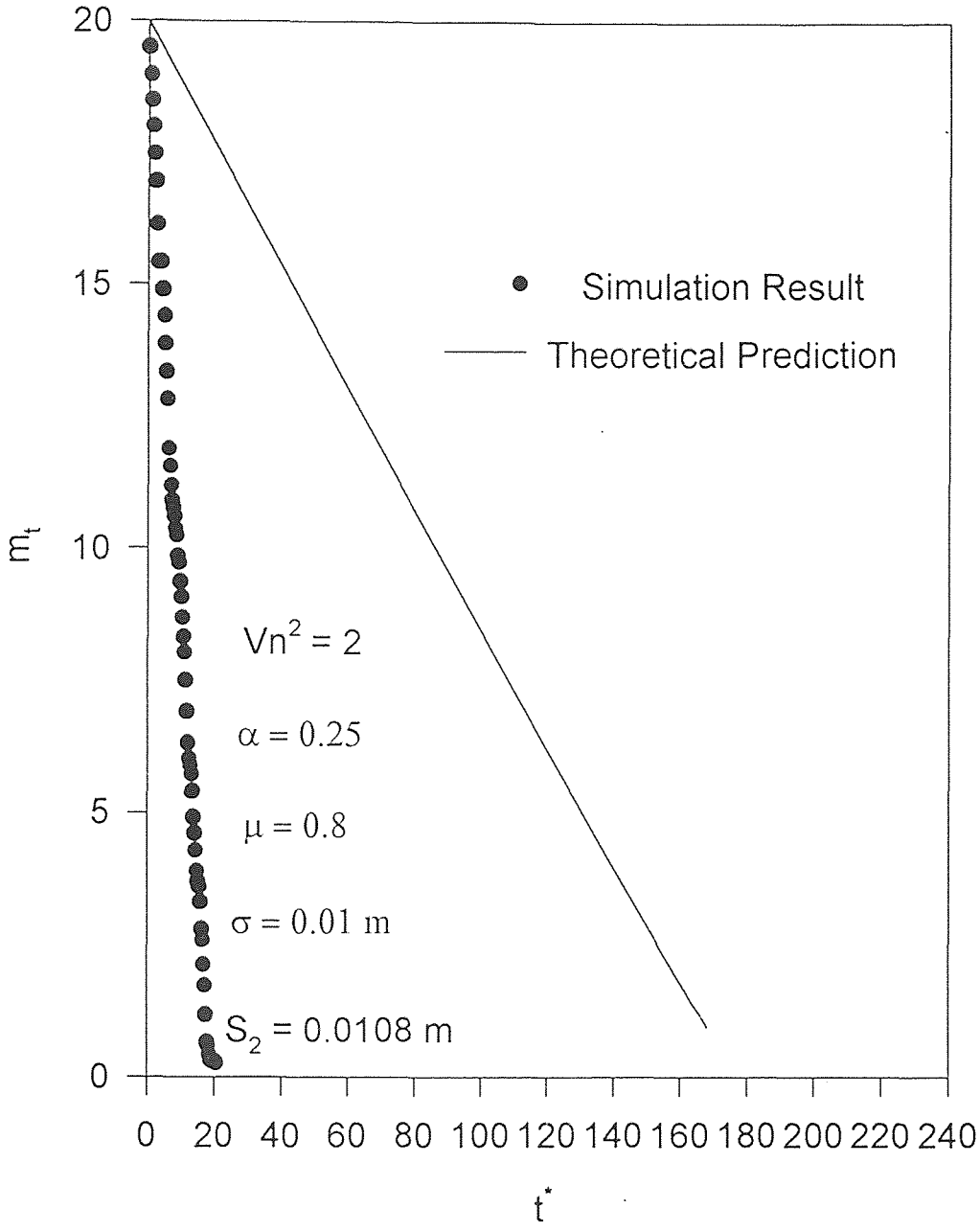

Figure A3.9(c) Mass hold-up profile compared with the theoretical prediction for $Vn^2 = 2$, $\alpha = 0.25$, $\mu = 0.8$, $\sigma = 0.01$ m, $S_2 = 0.0108$ m

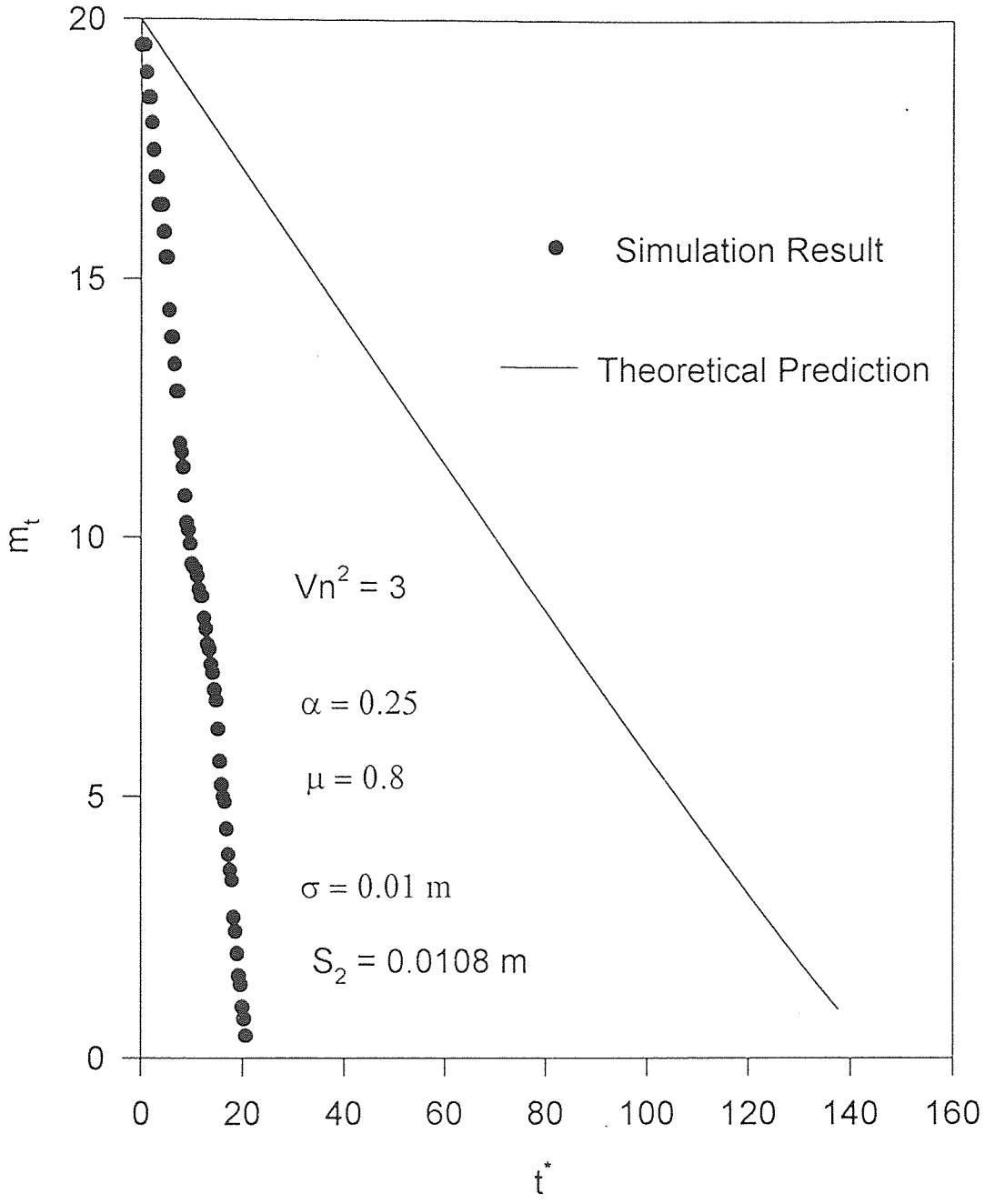

Figure A3.9(d) Mass hold-up profiles compared with the theoretical prediction for $Vn^2 = 3$, $\alpha = 0.25$, $\mu = 0.8$, $\sigma = 0.01$ m, $S_2 = 0.0108$ m

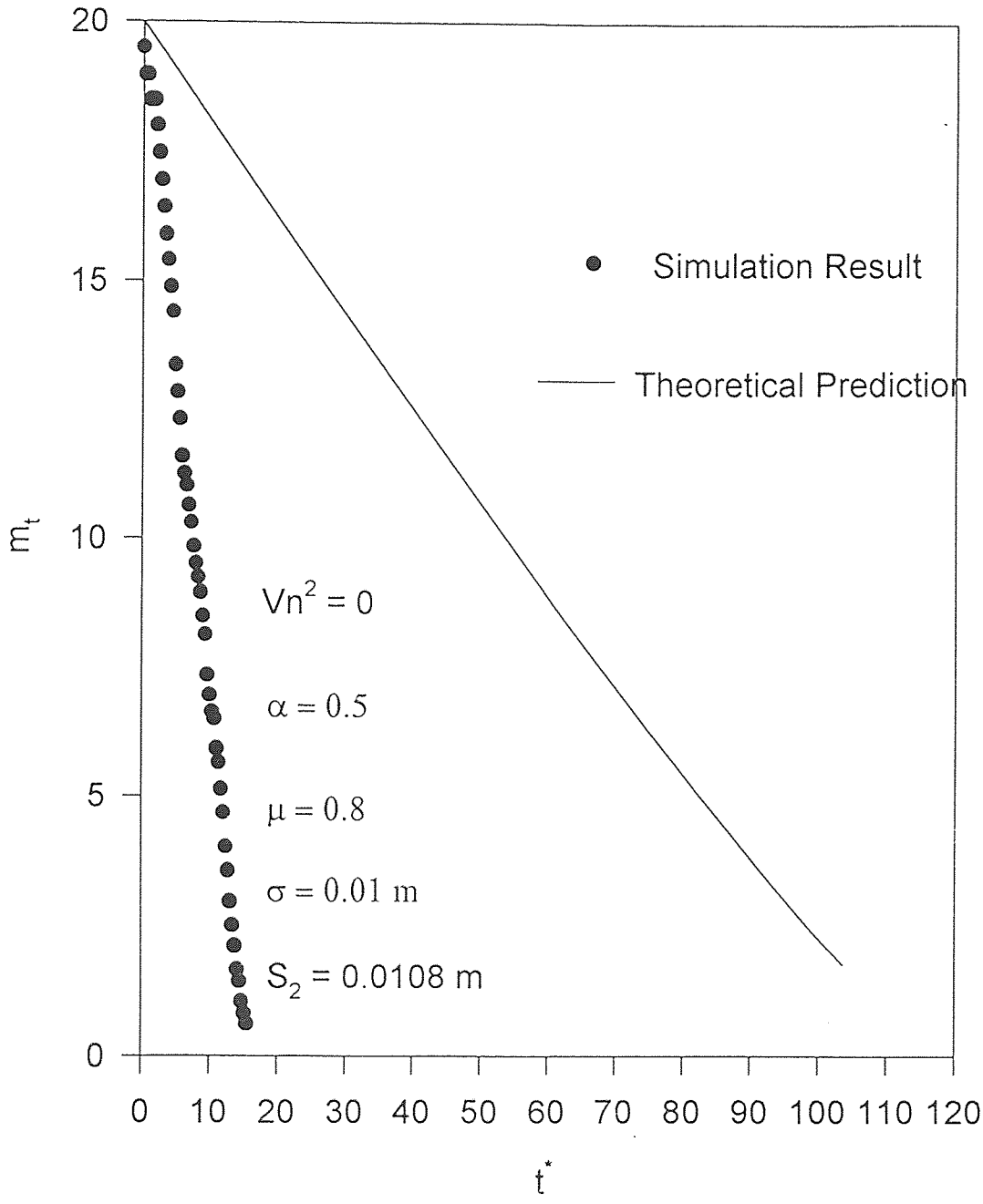

Figure A3.10(a) Mass hold-up profile compared with the theoretical prediction for $Vn^2 = 0$, $\alpha = 0.5$, $\mu = 0.8$, $\sigma = 0.01$ m, $S_2 = 0.0108$ m

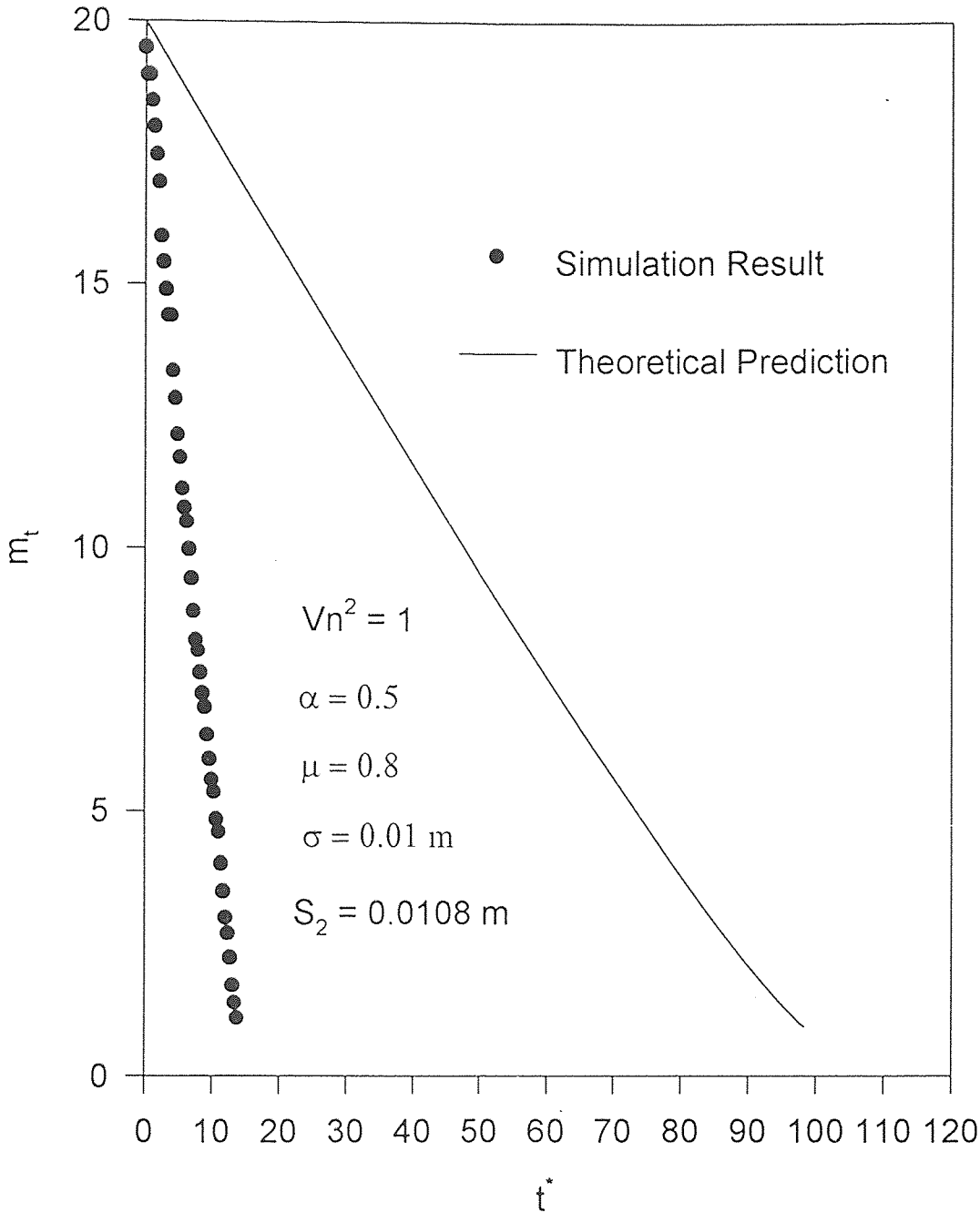

Figure A3.10(b) Mass hold-up profile compared with the theoretical prediction for $Vn^2 = 1$, $\alpha = 0.5$, $\mu = 0.8$, $\sigma = 0.01$ m, $S_2 = 0.0108$ m

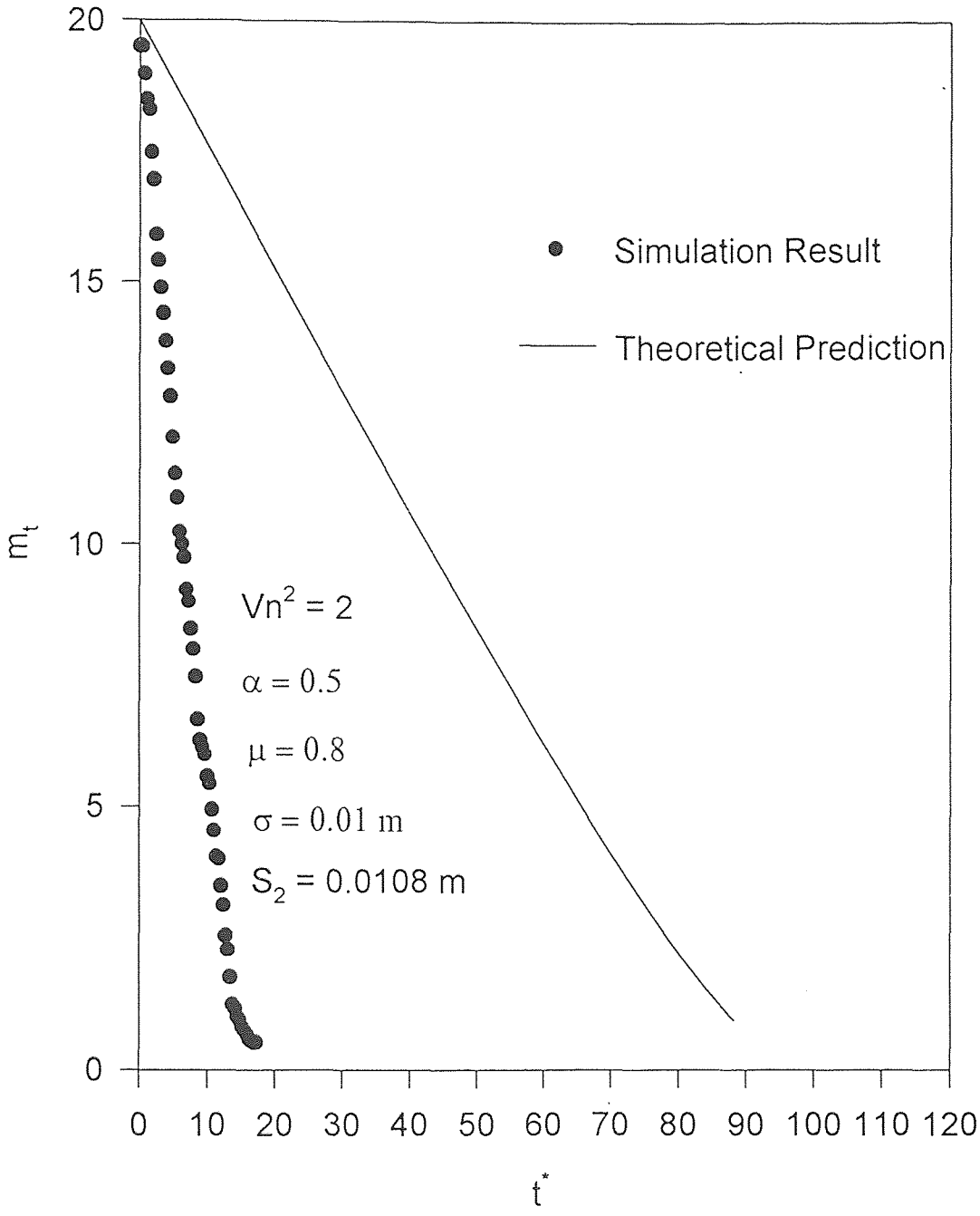

Figure A3.10(c) Mass hold-up profile compared with the theoretical prediction for $Vn^2 = 2$, $\alpha = 0.5$, $\mu = 0.8$, $\sigma = 0.01$ m, $S_2 = 0.0108$ m

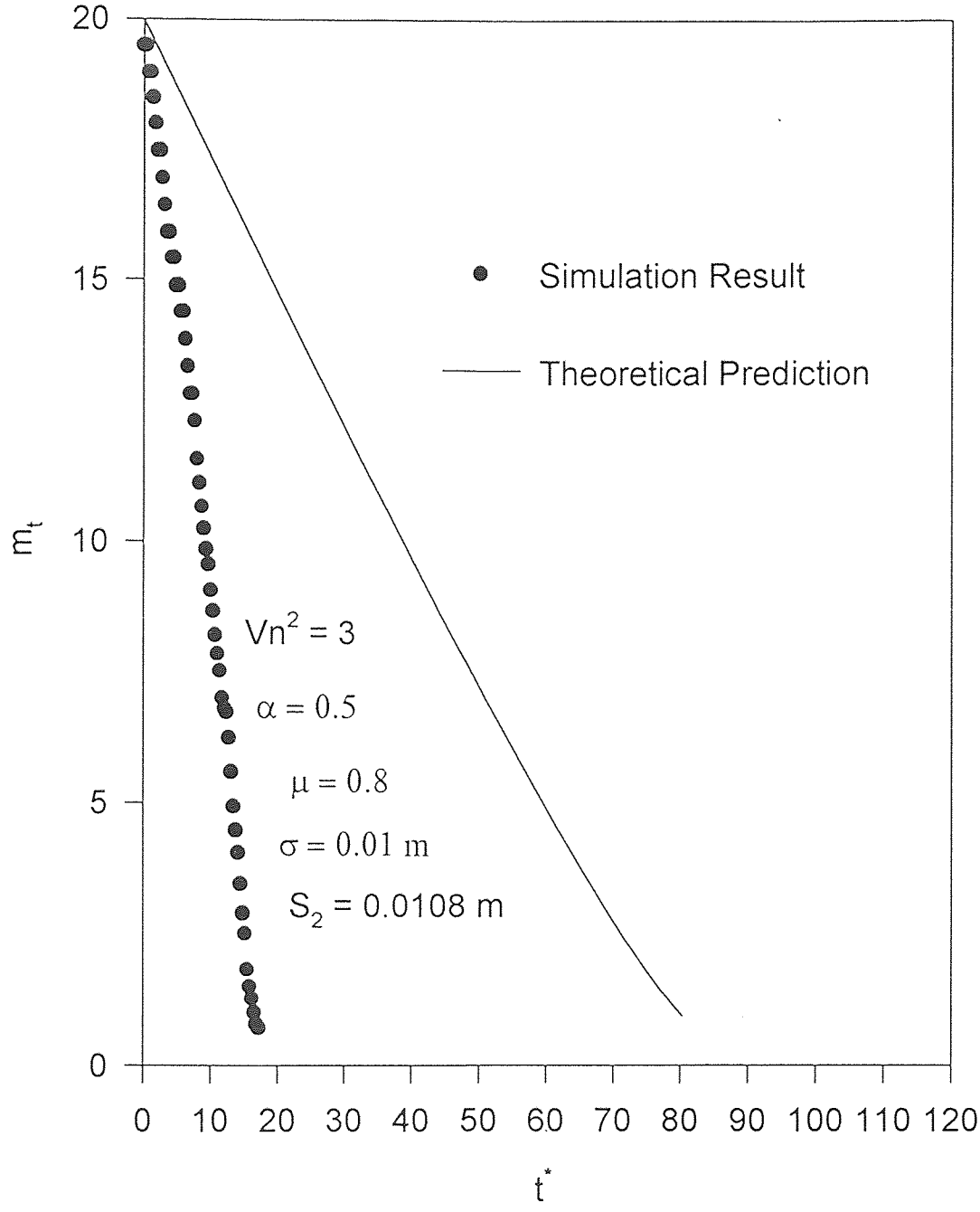

Figure A3.10(d) Mass hold-up profile compared with the theoretical prediction for $Vn^2 = 3$, $\alpha = 0.5$, $\mu = 0.8$, $\sigma = 0.01$ m, $S_2 = 0.0108$ m

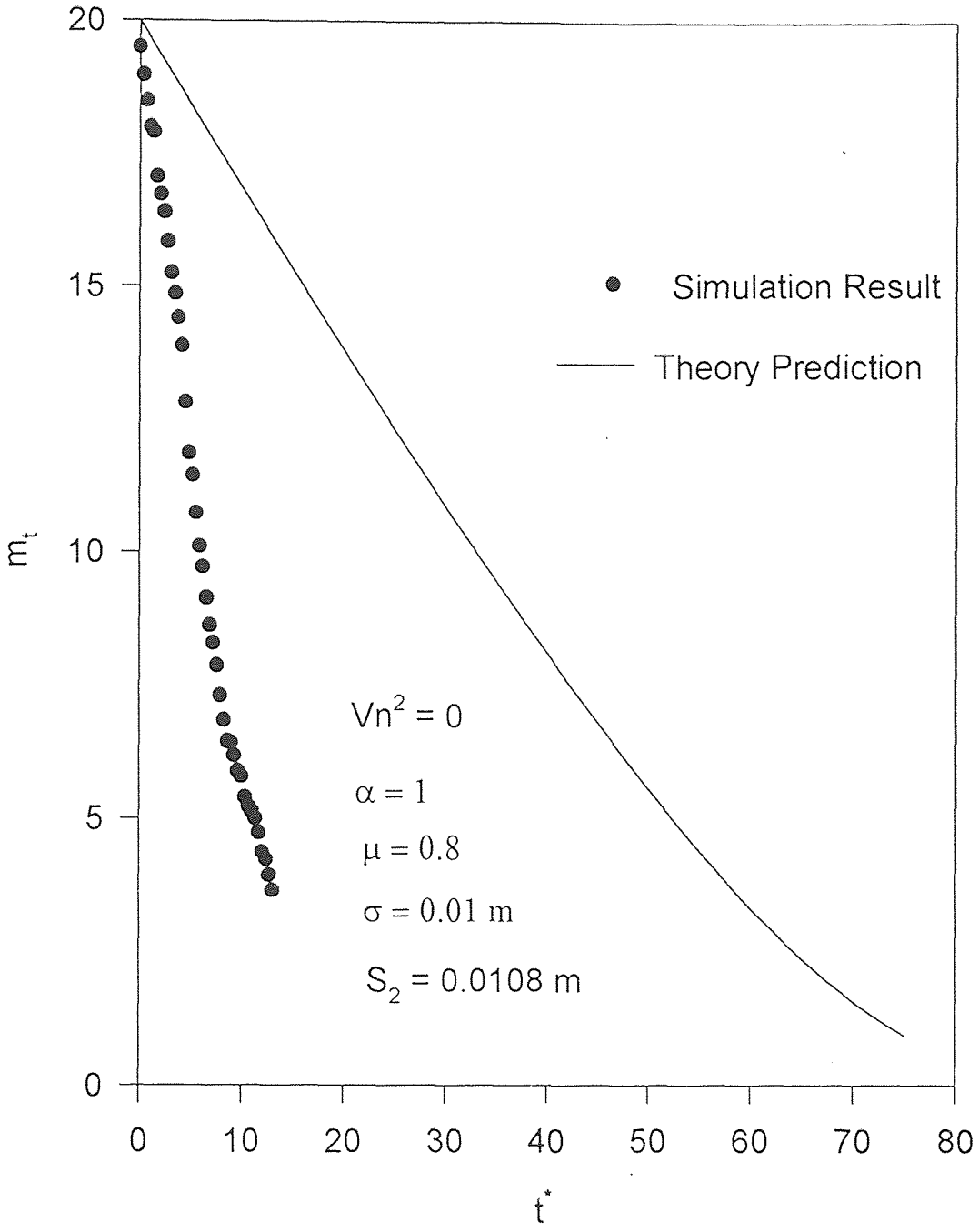

Figure A3.11(a) Mass hold-up profiles compared with the theoretical prediction for $Vn^2 = 0$, $\alpha = 1$, m = 0.8, $\sigma = 0.01$ m, $S_2 = 0.0108$ m

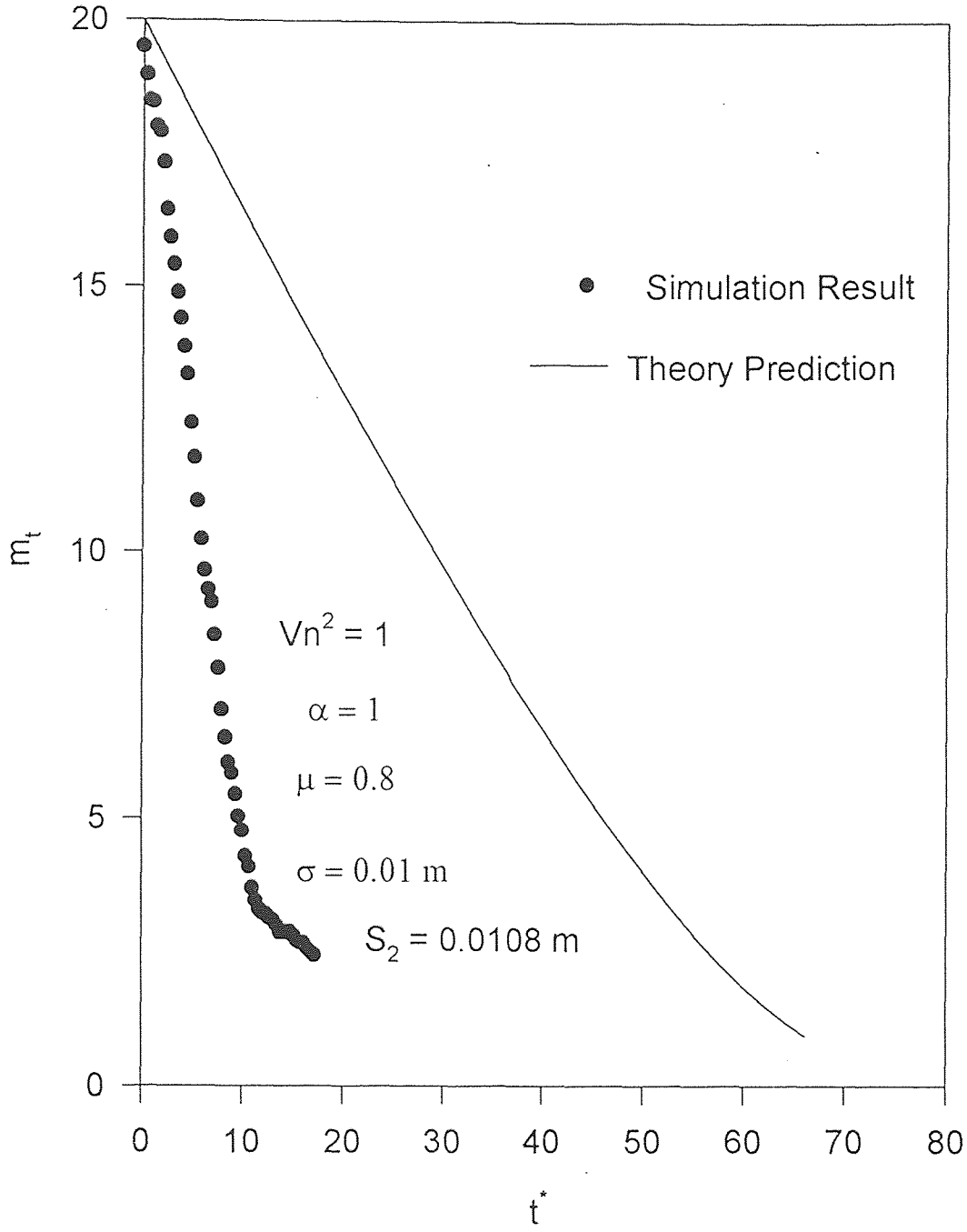

Figure A3.11(b) Mass hold-up profiles compared with the theoretical prediction for $Vn^2 = 1$, $\alpha = 1$, $m = 0.8$, $\sigma = 0.01$ m, $S_2 = 0.0108$ m

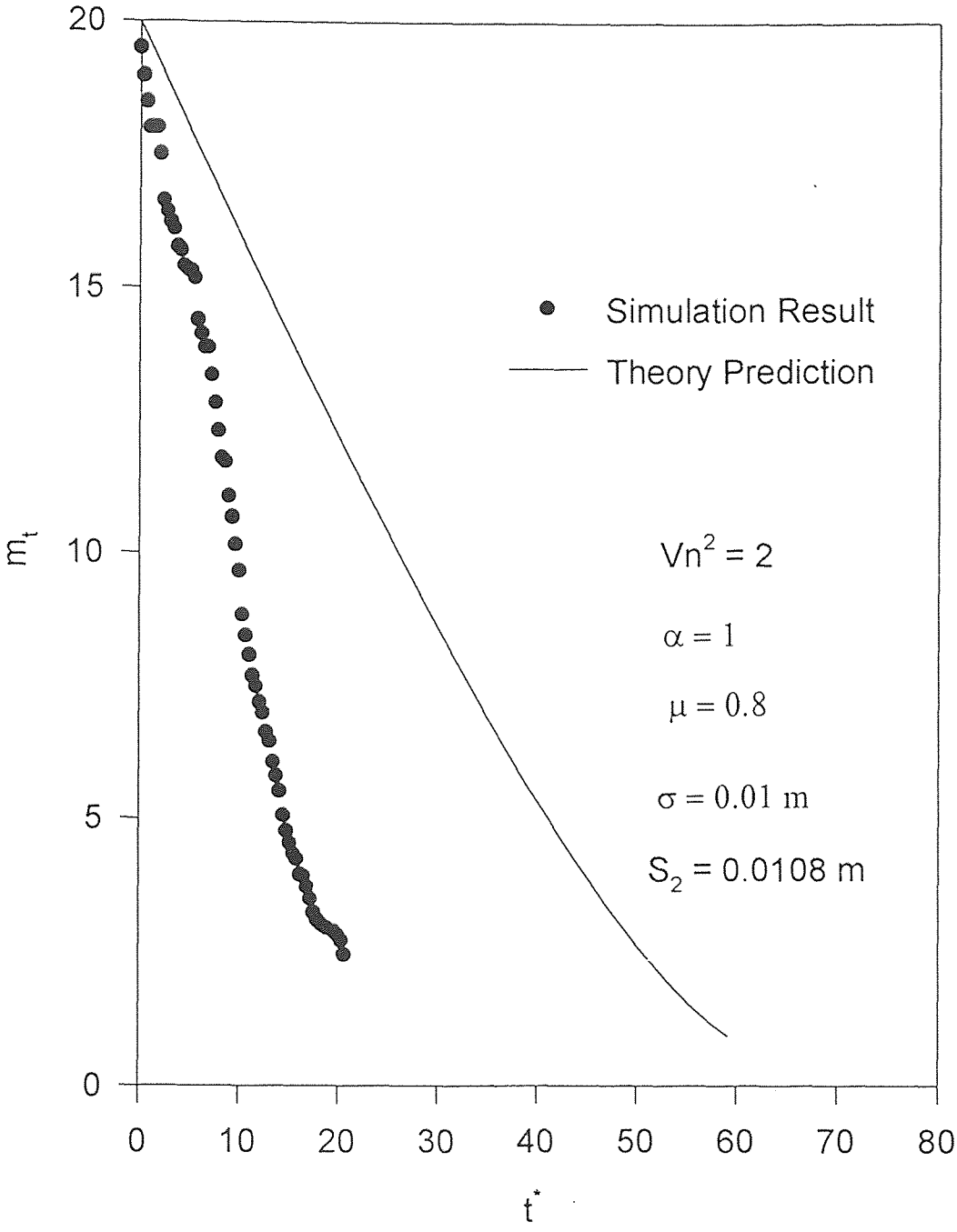

Figure A3.11(c) Mass hold-up profiles compared with the theoretical prediction for $Vn^2 = 2$, $\alpha = 1$, m = 0.8, $\sigma = 0.01$ m, $S_2 = 0.0108$ m

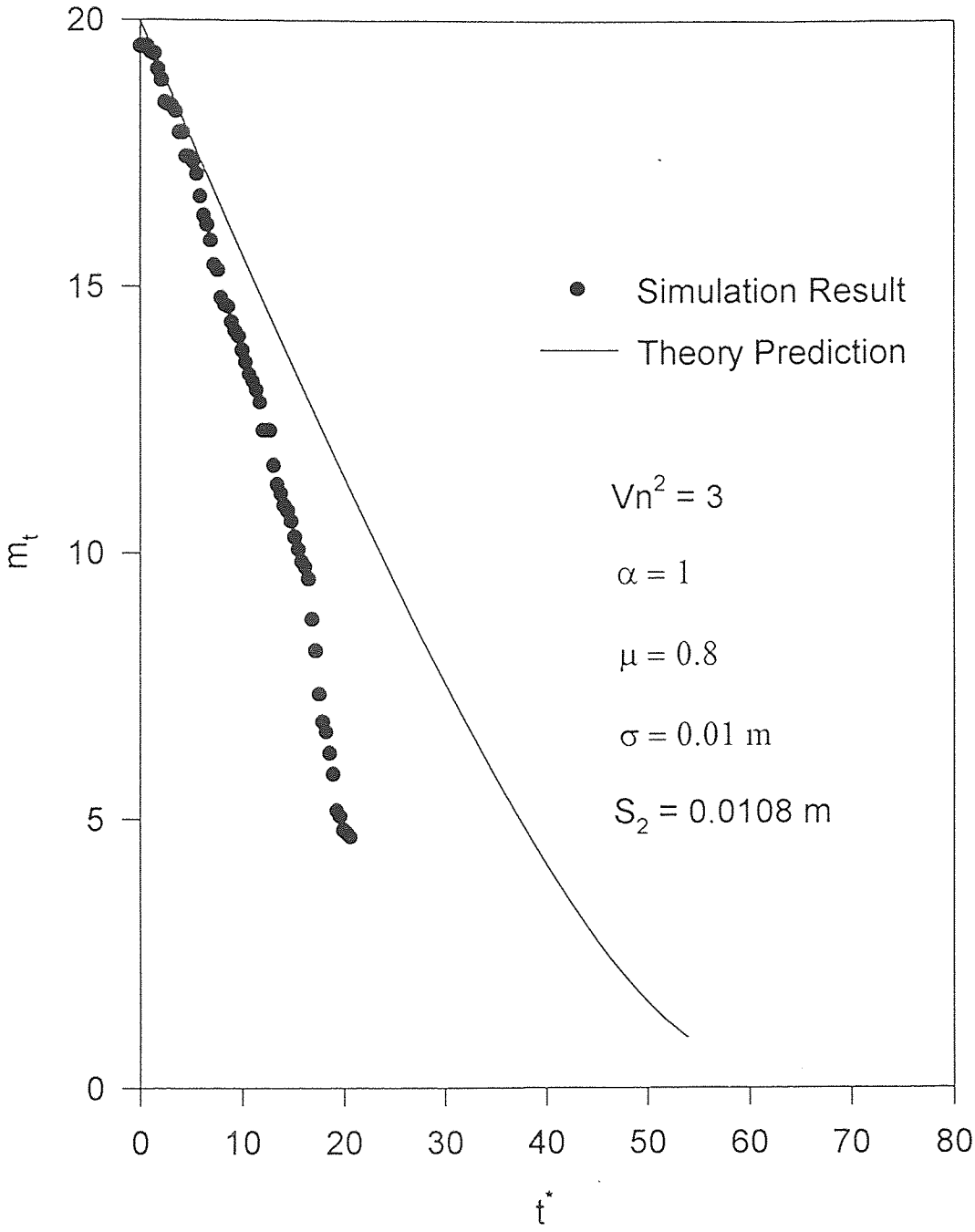

Figure A3.11(d) Mass hold-up profile compared with the theoretical prediction for $Vn^2 = 3$, $\alpha = 1$, m = 0.8, $\sigma = 0.01$ m, $S_2 = 0.0108$ m

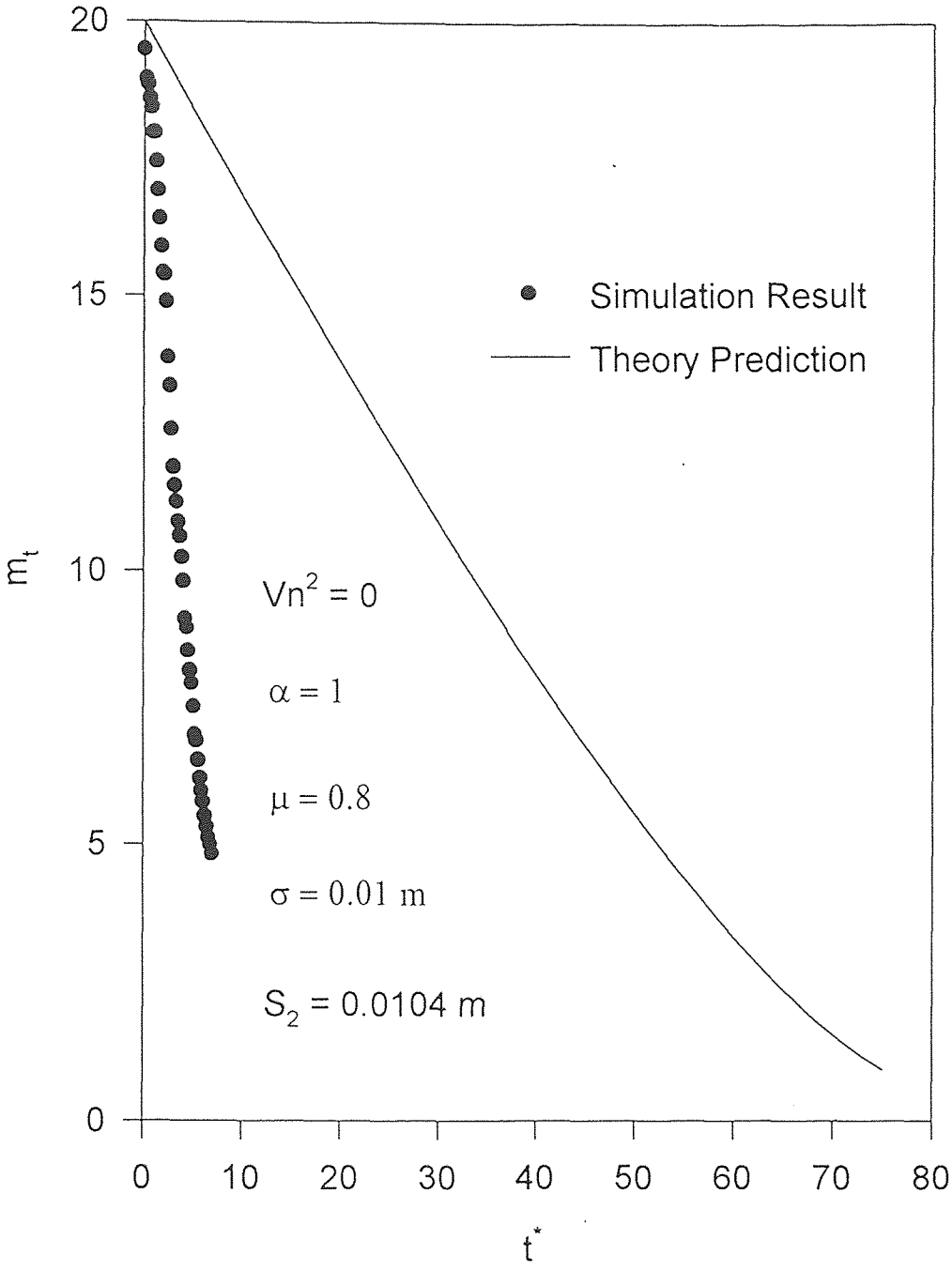

Figure A3.12(a) Mass hold-up profile compared with the theoretical prediction for $Vn^2 = 0$, $\alpha = 1$, m = 0.8, $\sigma = 0.01$ m, $S_2 = 0.0104$ m

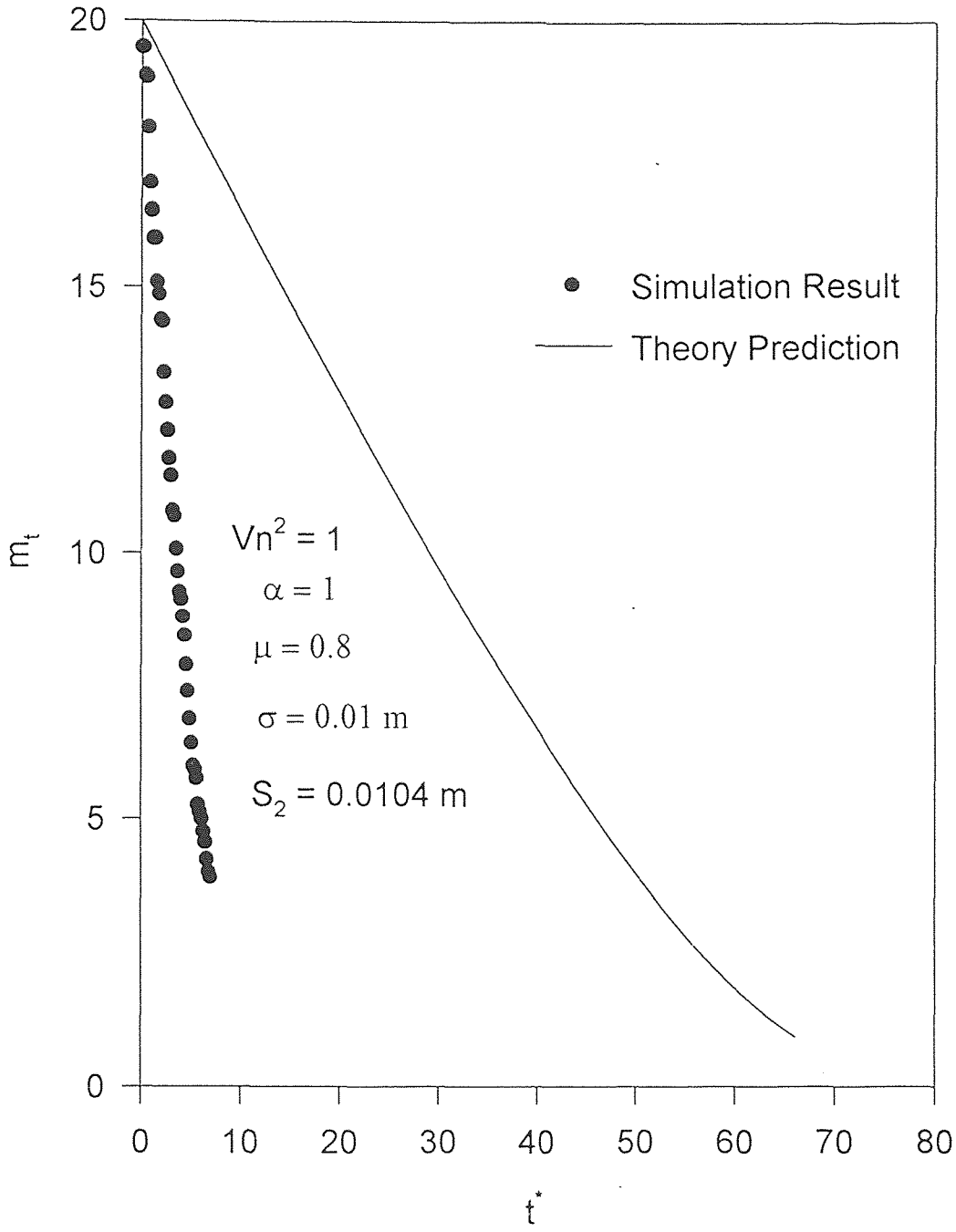

Figure A3.12(b) Mass hold-up profile compared with the theoretical prediction for $Vn^2 = 1$, $\alpha = 1$, m = 0.8, $\sigma = 0.01$ m, $S_2 = 0.0104$ m

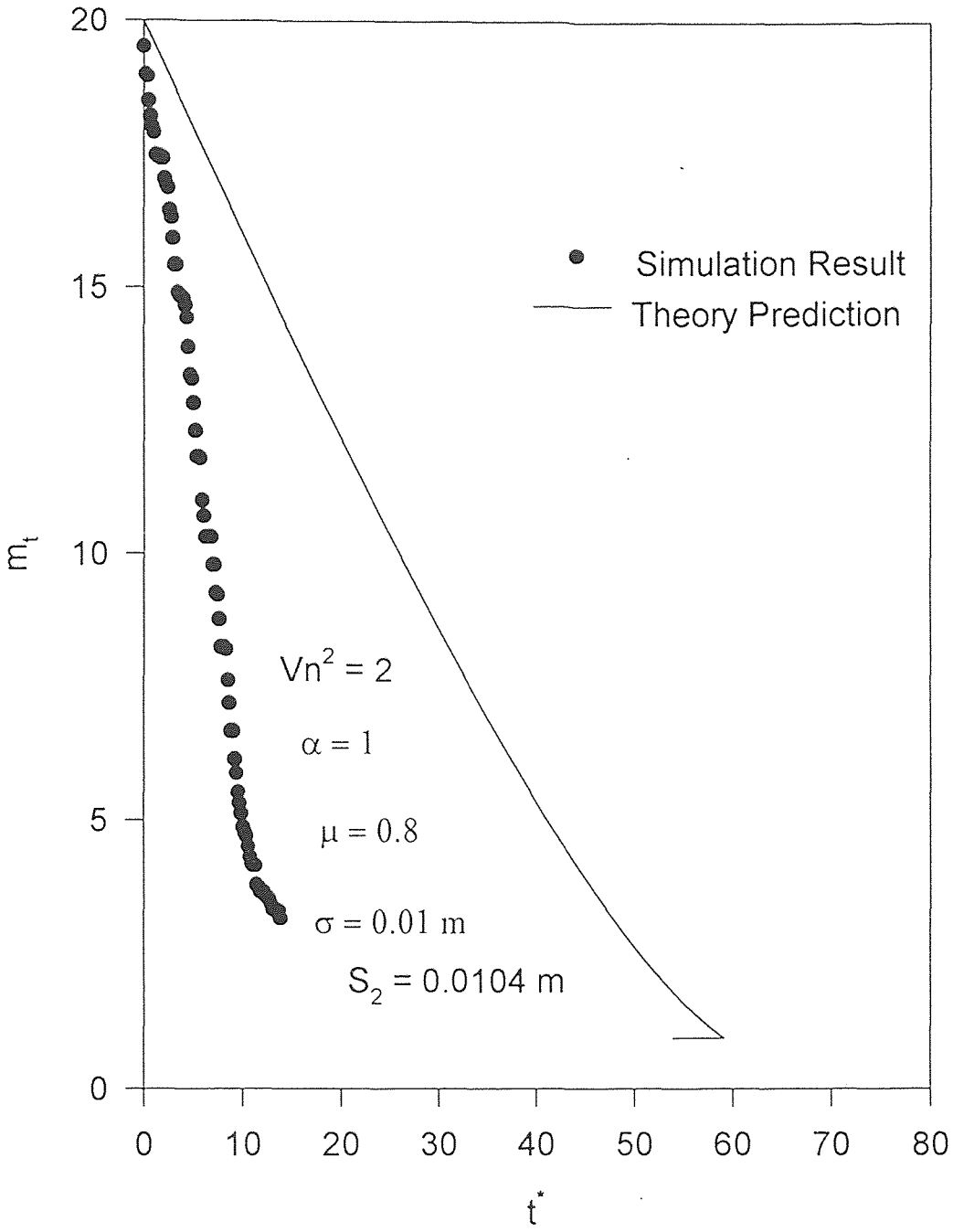

Figure A3.12(c) Mass hold-up profile compared with the theoretical prediction for $Vn^2 = 2$, $\alpha = 1$, $m = 0.8$, $\sigma = 0.01$ m, $S_2 = 0.0104$ m

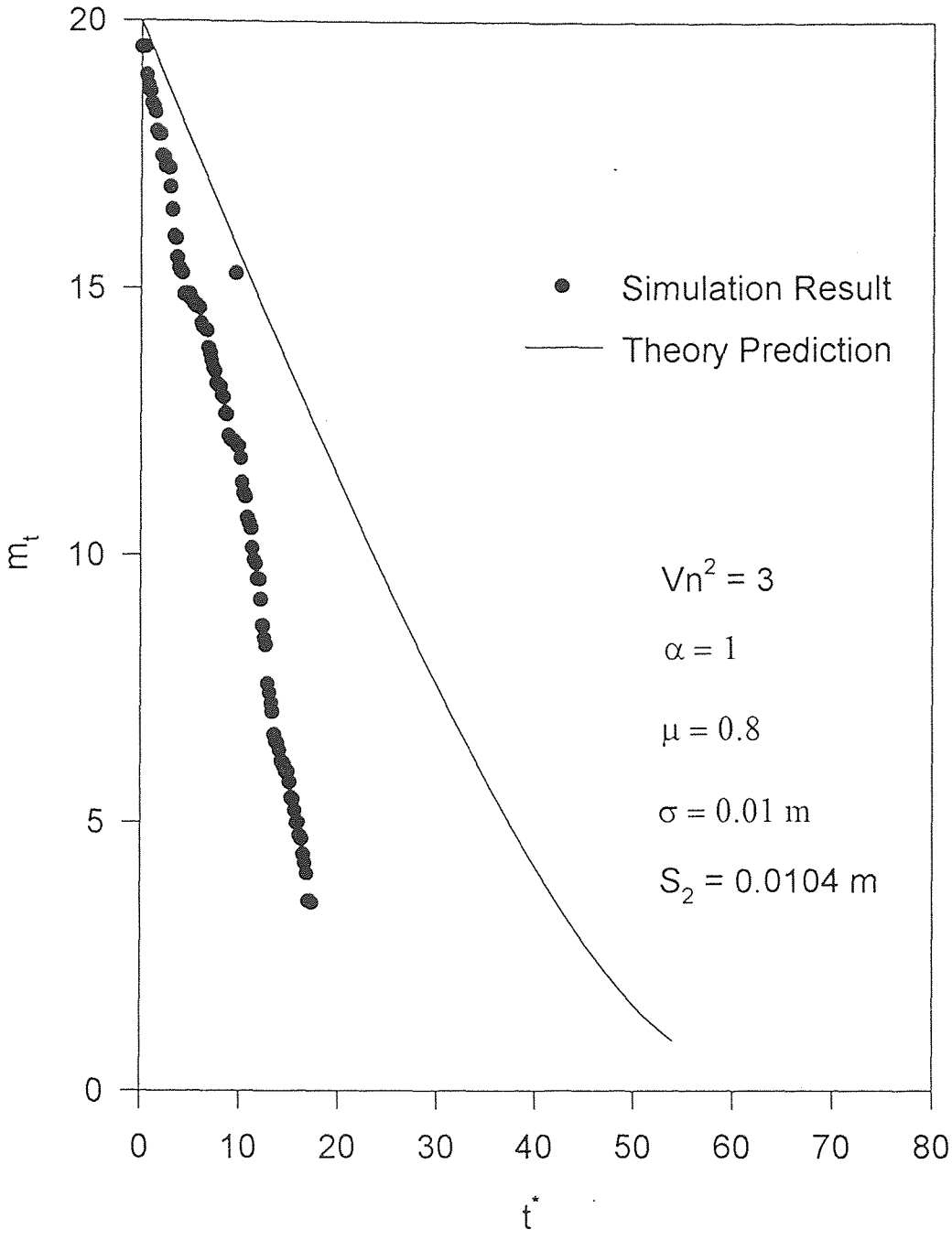

Figure A3.12(d) Mass hold-up profile compared with the theoretical prediction for $Vn^2 = 3$, $\alpha = 1$, m = 0.8, $\sigma = 0.01$ m, $S_2 = 0.0104$ m

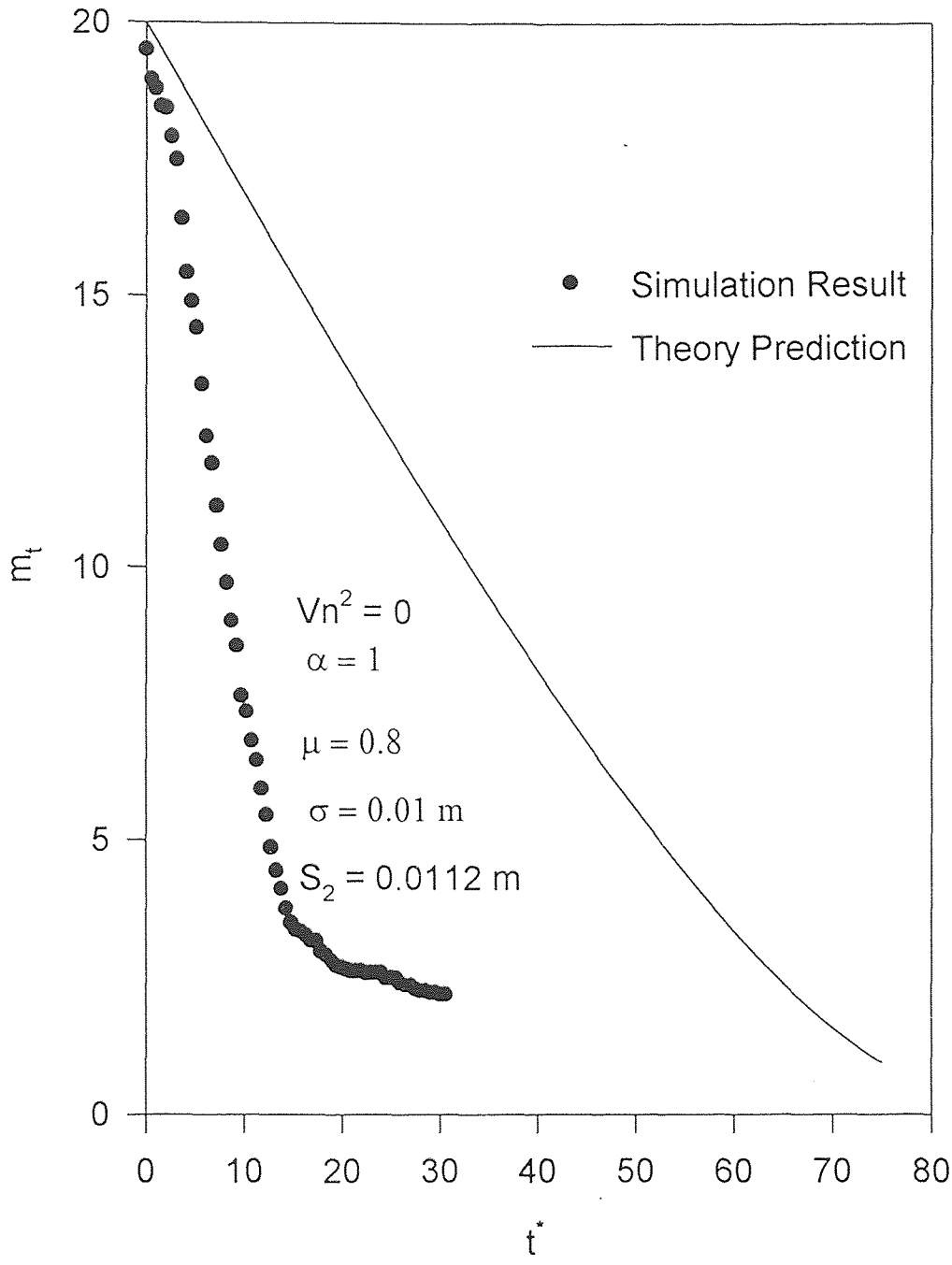

Figure A3.13(a) Mass hold-up profile compared with the theoretical prediction for $Vn^2 = 0$, $\alpha = 1$, m = 0.8, $\sigma = 0.01$ m, $S_2 = 0.0112$ m

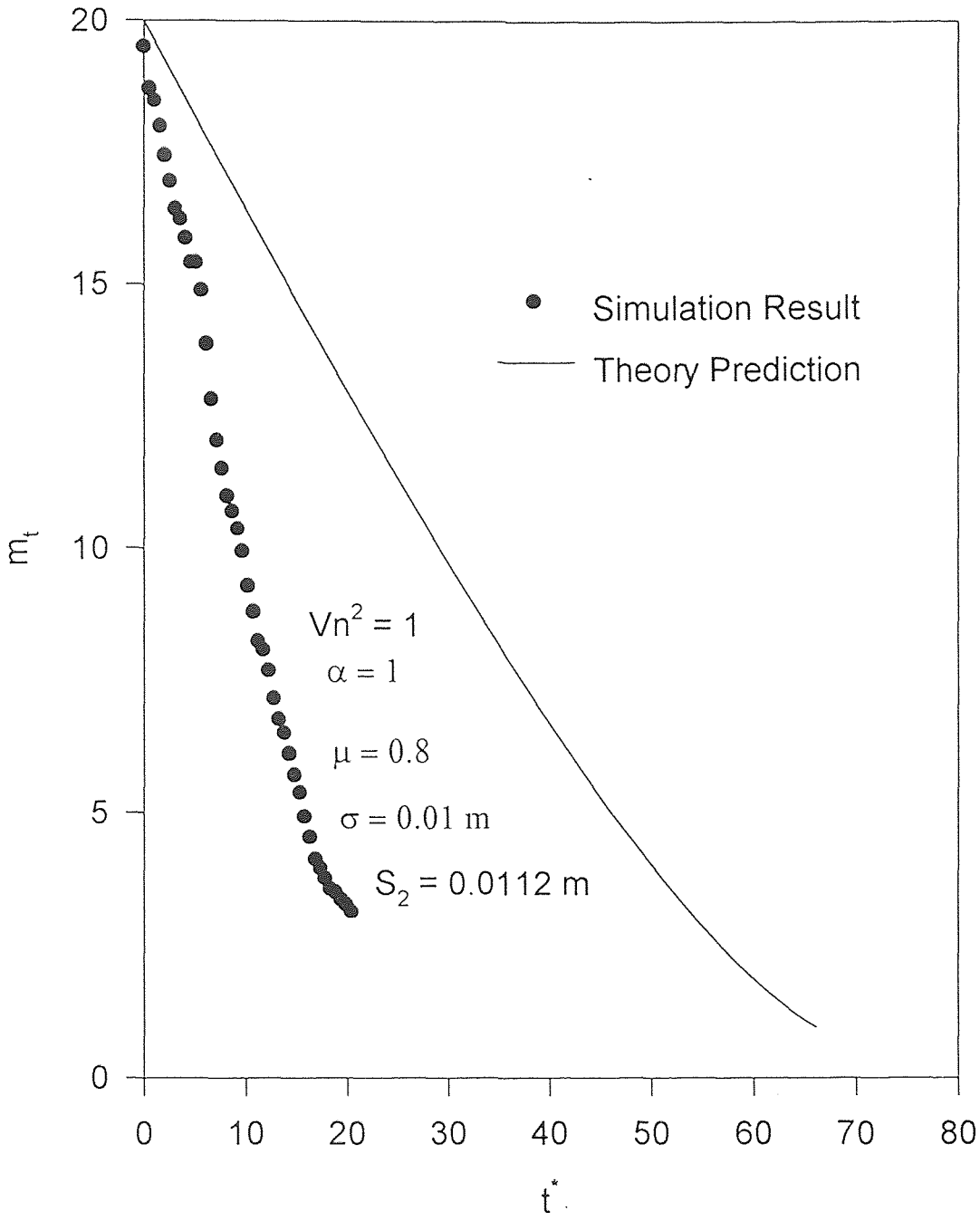

Figure A3.13(b) Mass hold-up profile compared with the theoretical prediction for $Vn^2 = 1$, $\alpha = 1$, $\mu = 0.8$, $\sigma = 0.01$ m, $S_2 = 0.0112$ m

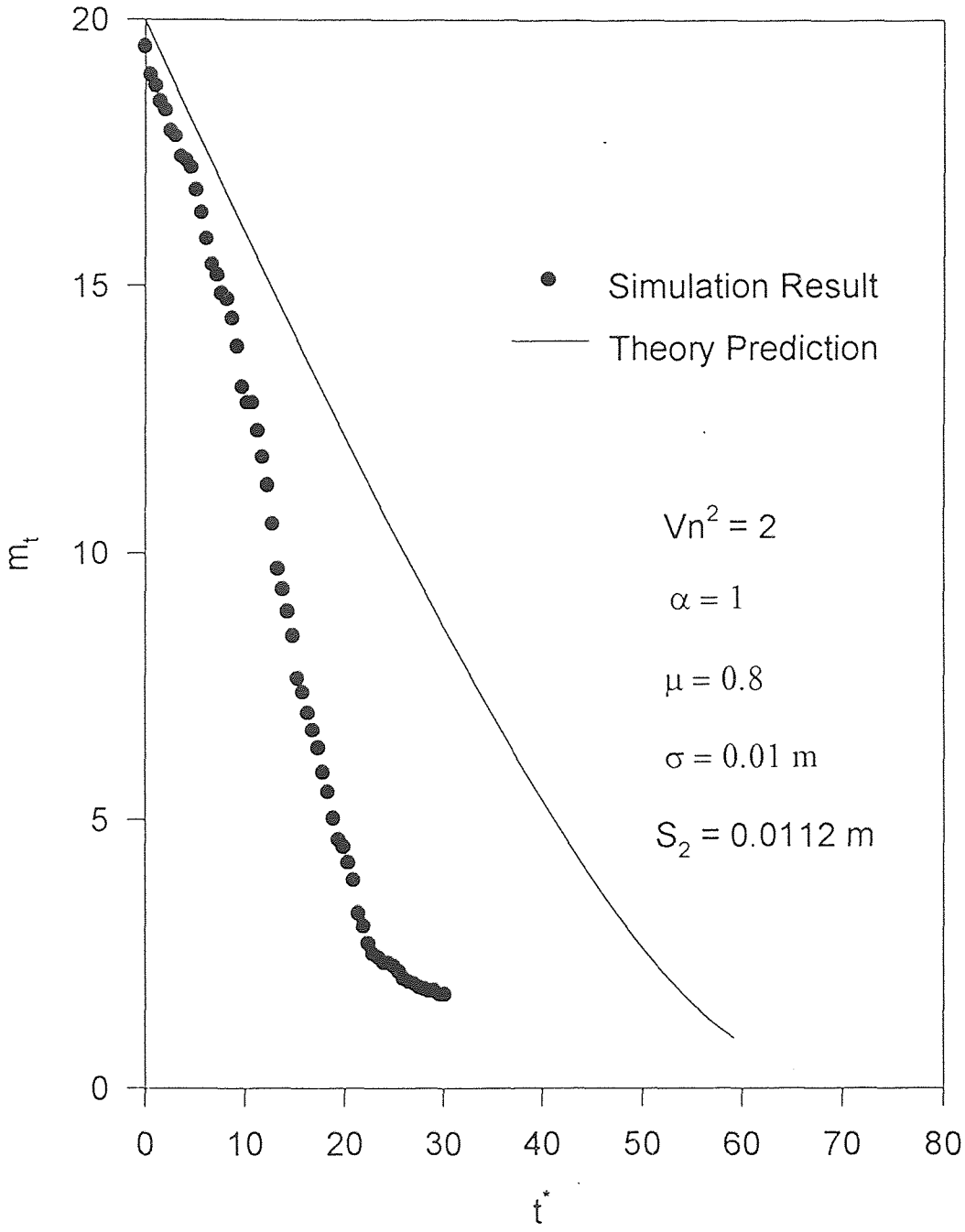

Figure A3.13(c) Mass hold-up profile compared with the theoretical prediction for $Vn^2 = 2$, $\alpha = 1$, $\mu = 0.8$, $\sigma = 0.01$ m, $S_2 = 0.0112$ m

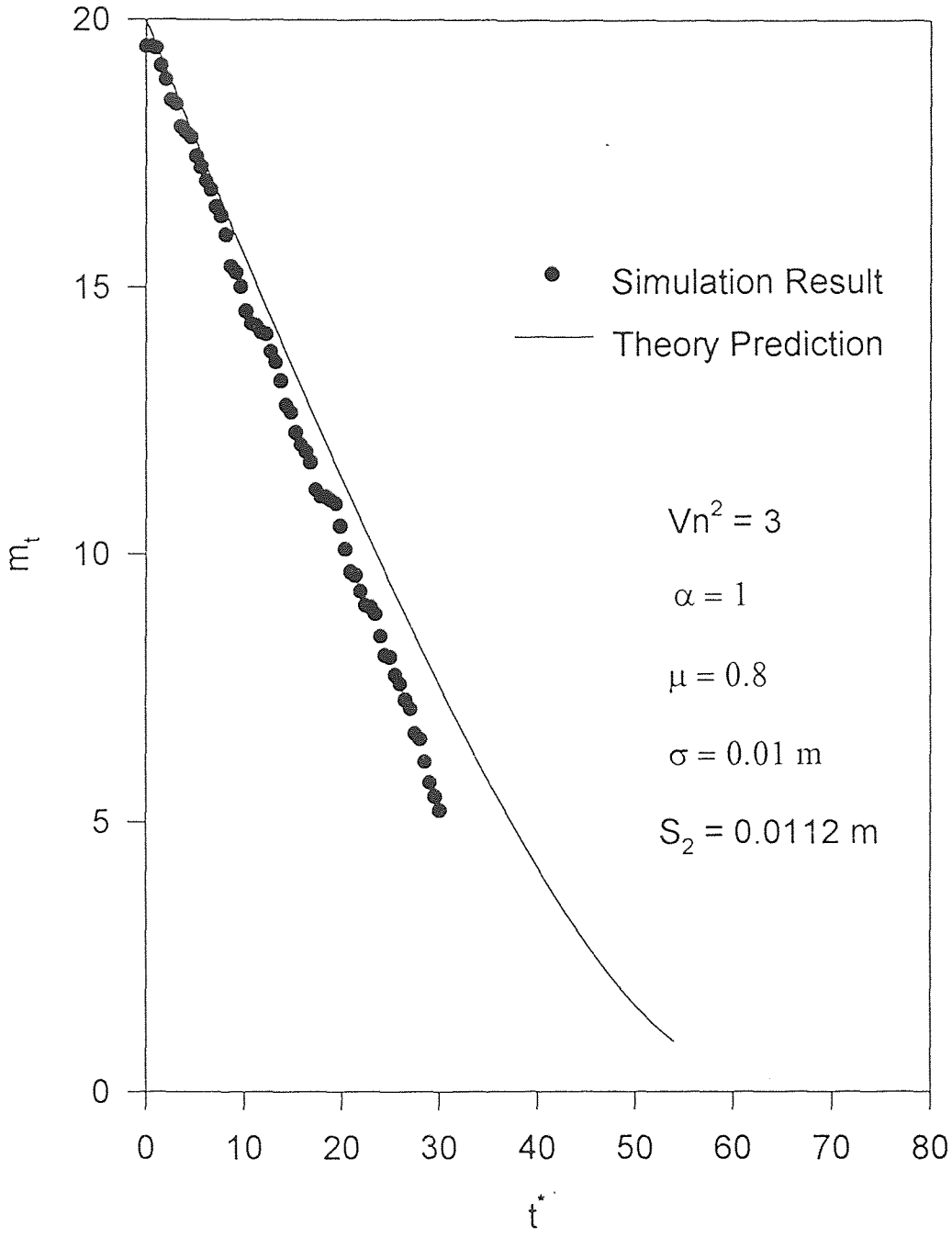

Figure A3.13(d) Mass hold-up profile compared with the theoretical prediction for $Vn^2 = 3$, $\alpha = 1$, $\mu = 0.8$, $\sigma = 0.01$ m, $S_2 = 0.0112$ m

REFERENCES

[1] Allen Ternence *Particle Size Measurement* Lecture in Powder Technology, Universty of Bradford (1968).

[2] Cadle, R. *Particle Size Determination* Stanford, Research Institute, Stanford, California (1955).

[3] Fagerholt,G. "Particle Size Distributionof Products Ground in Tube Mill" G.E.C. Gads Forlag, Copenhagen (1945).

[4] Frank G. Carpenter and Victor R. Deitz "Method of Sieve Analysis With Particular Reference to Bone Char," *Journal of Research of The National Bureau of Standards*, Vol.**45**, No.4, Oct. (1950), Research Paper 2143.

[5] Frank G. Carpenter and Victor R. Deitz "Glass Spheres for the Measurement of the Effective Opening of Testing Sieves" *Journal of Research of The National Bureau of Standards*, Vol.**47**, No.3, Sep. (1951), Research Paper 2238.

[6] Kaye B. "Investigation Into the Possibilities of Developing a Rate Method of Sieve Analysis" *Powder Metallurgy*, (1962), No.10:199-217.

[7] Kaye, B.and Robb, N. "An Algorithm for Deducing an Effective Sieve Residue from the Rate of Powder Passage through a Sieve" *Powder Technology*, **24**(1979):125-128

[8] Kenneth T. Whitby " The Mechanics of Fine Sieving" *ASTM spec. Tech. Publ.* No. **234**, 1959, P. 3.

[9] Kurt Leschonski "Sieve Analyses, the Cinderella of Particle Size Analysis Metjod" *Powder Tech.*, **24** (1979):115-124.

[10] Lan Y.D. "Particle Dynamics Modeling of Vibrating Granular Beds" Ph.D. Thesis, Mechanical Engineering Department, New Jersey Institute of Technology, Newark, New Jersey (1994).

[11] Manual of Test Sieving Methods" *A.S.T.M. Special Technical Publication* 447.

[12] Markwick, *Journal of the Society of Chemical Industry*, Vol.**59** (1940):88-92.

[13] Mindlin, R. D., and H. Deresiewicz, "Elastic Spheres in Contacts Under Varying Oblique Forces," *J. Appl. Mech(Trans. ASME)*, **20**(1953):327

[14] Richman, M. W. and R.E. Martine. "Unconfined Granular Materials Thermalized by Fluctuating Horizontal Surface." Proc. 9th conf. Engr. Mech. (ed. L.D., Lute, J. N., Niezwecki), *ASCE*, NY (1992):900-903.

[15] Richman, M. W. and L. Wang "Granular Flows Through Vibrating Surfaces With Holes" Mechanical Engineering Department, Worcester Polytechnic Institute, Worcester, MA 01609, U.S.A.

[16] Shergold F. "The Effect od Sieve Loading on the Results of Sieve Analysis of Nature Sands" *Journal of the Soc. of Chemical Industry*" Vol.65, Sep. (1946).

[17] Standish N. "The Kinetic of Batch Sieving" *Powder Technology*, 41(1985):57-67.

[18] Walton, O. R., "Numerical Simulation of Inelastic, Frictional Particle-Particle. Interactions." *Particulate Two-Phase Flow*, (ed. M. C. Roco), Butterworth-Heinemann, Boston (1992).